NANO · MICRO small
www.small-journal.com

3D Printing-Enabled Design and Manufacturing Strategies for Batteries: A Review

*Nathan Fonseca, Sri Vaishnavi Thummalapalli, Sayli Jambhulkar, Dharneedar Ravichandran, Yuxiang Zhu, Dhanush Patil, Varunkumar Thippanna, Arunachalam Ramanathan, Weiheng Xu, Shenghan Guo, Hyunwoong Ko, Mofe Fagade, Arunchala M. Kannan, Qiong Nian, Amir Asadi, Guillaume Miquelard-Garnier, Anna Dmochowska, Mohammad K. Hassan, Maryam Al-Ejji, Hassan M. El-Dessouky, Felicia Stan, and Kenan Song**

Lithium-ion batteries (LIBs) have significantly impacted the daily lives, finding broad applications in various industries such as consumer electronics, electric vehicles, medical devices, aerospace, and power tools. However, they still face issues (i.e., safety due to dendrite propagation, manufacturing cost, random porosities, and basic & planar geometries) that hinder their widespread applications as the demand for LIBs rapidly increases in all sectors due to their high energy and power density values compared to other batteries. Additive manufacturing (AM) is a promising technique for creating precise and programmable structures in energy storage devices. This review first summarizes light, filament, powder, and jetting-based 3D printing methods with the status on current trends and limitations for each AM technology. The paper also delves into 3D printing-enabled electrodes (both anodes and cathodes) and solid-state electrolytes for LIBs, emphasizing the current state-of-the-art materials, manufacturing methods, and properties/performance. Additionally, the current challenges in the AM for electrochemical energy storage (EES) applications, including limited materials, low processing precision, codesign/comanufacturing concepts for complete battery printing, machine learning (ML)/artificial intelligence (AI) for processing optimization and data analysis, environmental risks, and the potential of 4D printing in advanced battery applications, are also presented.

1. Introduction

Electrochemical energy storage (EES) refers to the procedure and method of converting chemical energy into electric energy via an electrochemical oxidation-reduction reverse reaction. The EES devices have been widely used in portable electronics and electric vehicles (EVs) as renewable energy due to their enormous potential to reduce carbon footprint and mitigate energy challenges with fossil fuel depletion while promoting an eco-friendly environment. These EES systems include batteries, fuel cells, and supercapacitors. Batteries are the most popular among these devices due to their fast-charging rates, long cyclability/lifetime, mechanical durability, higher energy efficiency than fuel cells, and better specific energy than supercapacitors. With the advances in materials and manufacturing, newer battery applications have emerged, such as wearable electronics, micro/smart sensors, medical devices, the Internet of Things (IoT), and electric transportation.[1,2] However, the

N. Fonseca, S. V. Thummalapalli, D. Ravichandran, Y. Zhu, D. Patil, V. Thippanna, A. Ramanathan, S. Guo, H. Ko, K. Song
Manufacturing Engineering
School of Manufacturing Systems and Networks (MSN)
Ira A. Fulton Schools of Engineering
Arizona State University (ASU)
Mesa, AZ 85212, USA
E-mail: kenan.song@asu.edu

The ORCID identification number(s) for the author(s) of this article can be found under https://doi.org/10.1002/smll.202302718

DOI: 10.1002/smll.202302718

S. Jambhulkar, W. Xu, S. Guo, H. Ko, K. Song
Systems Engineering
School of Manufacturing Systems and Networks (MSN)
Ira A. Fulton Schools of Engineering, Arizona State University (ASU),
Mesa, AZ 85212, USA

M. Fagade
Mechanical Engineering
School of Engineering for Matter
Transport and Energy (SEMTE)
Ira A. Fulton Schools of Engineering
Arizona State University
Tempe, AZ 85281, USA

demand for batteries in various applications is challenging to meet since they require a prolonged lifetime, survivability in harsh environments, size reduction, packing compatibility, biodegradability, and higher energy and power densities.

Conventional manufacturing methods for energy materials and rigid packaging or assembly requirements have significantly limited current battery dimensions (e.g., cylindrical, prismatic, pouch, and coin cells) and functionalities. As a new manufacturing technique, additive manufacturing (AM), or 3D printing, is a series of processes making 3D objects layer-by-layer based on light-monomer, heat-filament, laser-powder, or mechanical shear-ink interactions via digital modeling software. Compared to traditional subtractive manufacturing, AM has shown extensive versatility with better design freedom, and design versatility along with more efficient design/deposition systems. AM is becoming increasingly popular due to its rapid prototyping capabilities, cost- and time-efficiency, and a broad range of raw feedstocks. Among many different utilizations, the AM used for EES has facilitated new materials to be synthesized/fabricated, creative structures to be designed, and new applications to be targeted.[3,4] In addition, the AM for battery processing and packaging has benefits to i) flexibly include different material types (e.g., polymers, ceramics, metals, or their composites), ii) quickly tune microstructures or even nanoscale features (e.g., porosity, tortuosity, volume-to-surface ratio), iii) promptly design complex architectures or hierarchies (e.g., surface patterning or layers in packaging), iv) potentially maximize energy efficiency (e.g., mass loading of active materials), and (v) rapidly finish the life cycle assessment (e.g., on fly manufacturing, in-situ monitoring, data analytics for quality control).[4–7]

In modern energy-focused technologies, the AM field has pushed for higher energy density, strict safety characteristics, better interface with human beings, and enhanced sustainability in energy storage devices to meet design, manufacturing, cost, and environmental demands.[8,9] Most review papers in the 3D printing fields for energy storage devices (**Table 1**) fall into the following categories.

- Various 3D printing-compatible materials for electrochemical energy applications[6,10–12]
- 3D printing-enabled microstructures for energy applications[5,13–15]
- Main-stream 3D printing methods to compare different electrochemical performances[16–19]
- Different 3D printing-enabled solid-state energy storage devices focusing on supercapacitors and battery components[7,11,20]
- 3D printing-facilitated design and prototyping trends to process or manufacture electrodes and electrolytes[2,8,9,21–23]
- Methods in modeling, simulation, and data analytics regarding their role in 3D printing and the general manufacturing of energy devices[24–26]

However, a comprehensive summary of different 3D printing mechanisms for designing and manufacturing of energy storage applications based on each battery component (i.e., anode, cathode, and electrolyte) has been rarely reported. Therefore, unlike other literature papers in Table 1, we have focused on different 3D printing techniques for electrochemical energy applications, including the electrodes and solid-state electrolytes (SSEs), featuring the role of 3D printing in energy storage device development and their applications. Specifically, this review will first summarize currently available 3D printing methodologies such as light-based printing (i.e., stereolithography (SLA), digital light processing (DLP), continuous liquid interface production (CLIP), computed axial lithography (CAL), and two-/multi-photo polymerization (TPP/MPP)) as shown in **Figure 1**a_1, filament-based (i.e., fused deposition modeling (FDM), and direct ink writing (DIW)) in Figure 1a_2, powder-based (i.e., powder bed fusion (PBF)-based printing of selective laser sintering (SLS), and selective laser melting (SLM)) in Figure 1a_3, and jetting-based printing (i.e., PolyJet, MultiJet, and Binder jetting) displayed in Figure 1a_4 with their state-of-the-art trends, current challenges, and future mitigations. Section two will briefly summarize 3D printing platforms and their processing principles. Section three will cover the electrodes (i.e., cathode and anode), emphasizing the materials, manufacturing, and properties/performance. Similarly, section four covers the materials and 3D printing pathways for different

A. M. Kannan
Fuel Cell Laboratory
The Polytechnic School (TPS)
Ira A. Fulton Schools of Engineering
Arizona State University
Mesa, AZ 85212, USA
Q. Nian
School of Engineering for Matter
Transport and Energy (SEMTE)
Arizona State University
Tempe, AZ 85287, USA
A. Asadi
Department of Engineering Technology and Industrial Distribution (ETID)
Texas A&M University
College Station, TX 77843, USA
G. Miquelard-Garnier, A. Dmochowska
Laboratoire PIMM
Arts et Métiers Institute of Technology
CNRS, Cnam
HESAM Universite
151 Boulevard de l'Hopital, Paris 75013, France
M. K. Hassan, M. Al-Ejji
Center for Advanced Materials
Qatar University
P.O. BOX 2713, Doha Qatar
H. M. El-Dessouky
Physics Department
Faculty of Science
Galala University
Galala City 43511, Egypt
H. M. El-Dessouky
Physics Department
Faculty of Science
Mansoura University
Mansoura 35516, Egypt
F. Stan
Center of Excellence Polymer Processing & Faculty of Engineering
Dunarea de Jos University of Galati
47 Domneasca Street, Galati 800008, Romania
K. Song
Mechanical Engineering
University of Georgia
302 E. Campus Rd, Athens, Georgia 30602, United States

Table 1. Recent literature review papers in the field of advanced manufacturing of batteries (2015 onwards).

Year	Title	Focus	Refs.
2023	Application of 2D MXene in Organic Electrode Materials for Rechargeable Batteries: Recent Progress and Perspectives	Application of MXene in organic electrode materials for rechargeable batteries. Looking into organic polymers and the advantages of organic electrode materials. In addition to future perspectives focused on boosting stability of MXene, increasing the varieties and new fabrication strategies of MXene while developing surface chemistry in the battery application	[27]
2023	Material–structure–property integrated additive manufacturing of batteries	Package-level and material-structure-property applications with an emphasis on additive manufacturing of batteries. Material processing and integrated manufacturing approaches enable improvements in rechargeable batteries. Conversely, the difficulties and drawbacks of battery materials while also providing suggestions for improvements	[5]
2023	A non-academic perspective on the future of lithium-based batteries	Key metrics and challenges in addition to performance aspects when developing new technologies in the battery industry. Hence, an analysis of the supply chain, sustainability of materials, and system-level cost for the battery industry in addition to the latest developments with perspectives on the challenges and prospects of various technologies in the battery industry	[28]
2022	A focus review on 3D printing of wearable energy storage devices	Fundamentals of 3D printing inks used in wearable electrochemical systems such as batteries and supercapacitors with an emphasis on optimizing strategies in improving the mechanical and electrochemical properties	[4]
2022	Emerging application of 3D-printing techniques in lithium batteries: From liquid to solid	The working principles, advantages, and limitations for solid-state batteries via 3D printing methods with a focus on the modifications to raise the electrochemical performance of the electrodes and electrolytes	[17]
2022	Dry electrode technology, the rising star in solid-state battery industrialization	Review of the dry battery electrode techniques with an analysis of the superiorities, protocols, scientific principles, and potential attempts to improve the performance and production efficiency for industrialization	[18]
2021	Design Strategies of 3D Carbon-Based Electrodes for Charge/Ion Transport in Lithium-ion Battery and Sodium Ion Battery	The operating mechanism of charge/ion transport in 3D carbon-based electrodes with a focus on architectural analogies, such as porosity and tortuosity for higher capacity and fast transport	[21]
2021	3D Printing for Solid-State Energy Storage	Recent advances in 3D-printed solid-state energy storage devices, including solid-state batteries and solid-state supercapacitors	[20]
2021	3D printing for rechargeable lithium metal batteries	Recent advances in 3D printing rechargeable lithium metal batteries with fundamental principles, printing techniques, applications, design rationales, and practical challenges	[29]
2021	3D printing of advanced lithium batteries: a designing strategy of electrode/electrolyte architectures	Development trends of electrodes and electrolyte designs via 3D printing technologies, as well as prospects and challenges of 3D-printed lithium batteries	[9]
2021	3D printing-enabled advanced electrode architecture design	Recent studies on 3D-printed electrodes with advanced interdigitated structures, through-thickness aligned structures, hierarchical porous structures, and fiber and fabric structures of electrodes. Hence, novel advancements in electrode architecture are generated and optimized by computational simulation and machine learning	[8]
2021	Design and Manufacturing of 3D-Printed Batteries	Introduction to unique features of 3D printing techniques for battery modules and general approach to making them printable. Examining prominent roles of printing design in the module architectures battery configuration and effective solutions. Hence, a guide for further research direction on functional materials, advanced printing technologies, and new designs	[2]
2021	Hierarchically porous membranes for lithium rechargeable batteries: Recent progress and opportunities	Mechanisms for membranes with hierarchically porous frameworks or ordered channels can be employed as electrodes, separators interlayers, electrolyte transport, and charger transfer. In addition to future prospects of optimizing membrane development for advanced battery applications	[22]
2020	Evolution of 3D Printing Methods and Materials for Electrochemical Energy Storage	Materials and method requirements for 3D printable batteries as well as supercapacitors with future perspectives for printable energy-storage materials, casings, and direct printing electrodes and electrolytes	[11]
2020	3D printing of structured electrodes for rechargeable batteries	Materials, technologies, and structures for 3D printing. Optimization strategies for batteries, along with challenges and critical directions toward 3D printing electrodes/electrolytes	[12]
2020	3D Printing for Electrochemical Energy Applications	Overview of the motivation for 3D printing electrochemical energy storage applications and how they are affected by various 3D-printing technologies and post-modification techniques. In addition to future perspectives	[3]

(*Continued*)

Table 1. (Continued).

Year	Title	Focus	Refs.
2020	Additive Manufacturing of Batteries	Significant achievements in 3D printing batteries, along with challenges and potential research frontiers in developing 3D printing techniques and materials for batteries	[10]
2020	Recent advances and future challenges in printed batteries	Recent advances in 3D-printed batteries are separated by lithium-ion batteries, Zn/MnO_2 batteries, and other battery types. In addition to future challenges in the area of printed batteries	[30]
2019	3D Printing for Electrocatalytic Applications	3D printing benefits, potential, limitations, and current development trends for electrocatalytic applications. The future perspective of electrodes is based on size, printing resolution, and cost. In addition to future perspectives and developments for electrocatalytic applications	[31]
2019	3D printed electrochemical energy storage devices	Design on printed materials, printing process, and electrochemical performance of printed devices as well as an overview of future designs	[6]
2017	Emerging 3D-Printed Electrochemical Energy Storage Devices: A Critical Review	Recent advantages of the sandwich-type and in-plane architectures for energy storage devices. In addition to future perspectives with unique challenges and important directions	[23]
2017	3D printing of components and functional devices for energy and environmental applications	Recent advances regarding the implementation of 3D printing for energy and environmental applications	[32]
2017	Progress in 3D Printing of Carbon Materials for Energy-Related Applications	Recent developments in 3D printing energy-related applications, electronic circuits, and thermal-energy applications at high temperatures, in addition to future designs and developments	[19]

types of solid electrolytes, including oxide-solid electrolytes (OSEs), solid-polymer electrolytes (SPEs), and composite-solid electrolytes (CSEs). Each section focuses on material choices, design trends, process rationale and optimization, and system performance. Lastly, section five of the review provides new insights and perspectives for advanced manufacturing energy storage device studies. To this end, we cover some current challenges in discovering new feedstock materials for AM, as shown in Figure $1b_1$. Figure $1b_2$ highlights the lack of printing resolution for microporous patterning and complex hierarchies in the current 3D printing methods. Figure $1b_3$ brings attention to new methods of co-design and co-manufacturing concepts to fabricate a complete battery in a single step. Figure $1b_4$ brings a call to action of incorporating uncertainty prediction through machine learning (ML) and artificial intelligence (AI) for optimization and data analysis while navigating around the risks in Figure $1b_5$ through implementing recycling methods for batteries. Additionally, the current challenges in the AM for electrochemical energy storage (EES) applications, including limited materials, low processing precision, co-design/co-manufacturing concepts for complete battery printing, machine learning (ML)/artificial intelligence (AI) for processing optimization and data analysis, environmental risks, the potential of4D printing as shown in Figure $1b_6$, a lack of rare metals, and further development of advanced computer technology in advanced battery applications, are also presented.

2. Additive Manufacturing Methods

2.1. Light-Based Printing

2.1.1. Stereolithography (SLA)

SLA utilizes a light source to polymerize a photocurable resin (i.e., photoinitiator and monomer) and create delicate printable structures. SLA has diverged with many different mechanisms and uses (i.e., scanning, projection, continuous, and volumetric), diversifying the SLA systems with continuous improvements for the 3D printing resolutions and processing rates.[33] Depending on the platform elevation direction, there are two approaches when depositing one layer of cure resin on another, i.e., top-down and bottom-up.[33] The bottom-up method is more advantageous than the top-down method due to the faster printing speed and non-sealed environment, which can prevent oxygen inhibition during photopolymerization, as presented in **Figure 2**a. Resin curing-based 3D printing is particularly attractive for a few reasons: high levels of building resolution (μm and better), good z-axis strength due to chemical bonding between layers, and the ability to print transparent objects.[34] Critical parameters for the SLA include the machine parameters (e.g., light wavelength, typically ultraviolet light (UV), light-resin interactions), material parameters (e.g., photoinitiator, quenchers, inhibitors, diluents, rheology, solvents, monomer types, surface tension, particle additives), and printing parameters (e.g., scan speed, spot size, exposure duration, layer thickness, patterns of masks or scans). Over the years, SLA printing has evolved and expanded its technological capabilities by drawing inspiration from its original roots. This has led to the emerging of various new types of printers. Henceforth, the following subsections will cover DLP, CLIP, CAL, and TPP/MPP technologies, summarized in a systematic order (from older to newest) with updated trends, limitations, and perspectives.

2.1.2. Digital Light Processing (DLP)

While DLP works similarly to SLA, the main difference is that DLP uses a digital micromirror device (DMD) projector instead of a raster laser, allowing it to print an entire layer simultaneously. As a result, DLP is useful for sequential processes aiming

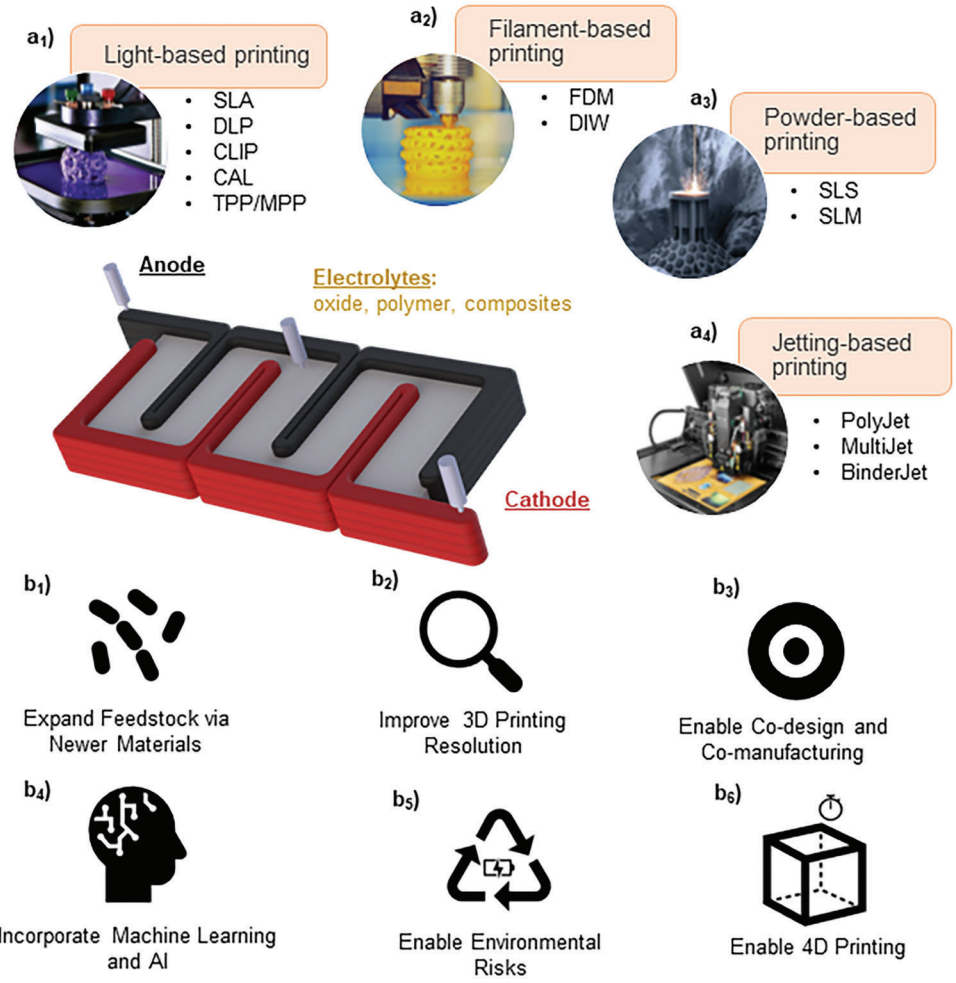

Figure 1. Additive manufacturing (AM) techniques for batteries, including a_1) light-based printing, a_2) filament-based printing, a_3) powder-based printing, and a_4) jetting-based printing, depicted with their respective subtypes. The schematic also illustrates future advancements to b_1) expand the feedstock of printers via new materials, b_2) improve the printing resolution, (b_3) adopt co-design and co-manufacturing methods, b_4) incorporate machine learning (ML) and artificial intelligence (AI) for optimized in-situ fabrication methods, b_5) navigate around the risks through implementing recycling methods for batteries, and b_6) enable 4D printing of energy storage devices.

to minimize trial and error. This concept was developed in 1997 by Texas Instruments,[35] shortly after the SLA technology was introduced. It should be noted that DLP technology operates at a different wavelength and exhibits major differences in terms of rheology, which makes it faster and more adaptable than SLA technology. For example, one of the major and most distinctive differences between DLP and SLA is the printing platforms. As previously mentioned, DLP uses a DMD scanner that creates 2D images of light and dark pixels, generating desirable XY-plane resolution and allowing it to print faster by virtue of layer printing versus dot printing in general SLA. In addition, DLP can print in a bottom-up shown in Figure $2b_1$ or top-down in Figure $2b_2$ configuration, similar to the general SLA. The bottom-up prints are inverted on the build head, and that light will come from the bottom to the top. Conversely, the top-down configuration prints from the top of the vat, meaning the exposure to light will come from the top to the bottom. Furthermore, DLP is not limited to photosensitive resins and shows high flexibility to print ceramic- and metal-loaded suspensions with post-processing (i.e., debinding and sintering) techniques. Moreover, DLP can be fused with other printing platforms, such as DIW[36] and binder jet printing (BJP),[37] to print multiple materials at once, opening new applications, such as dental implants, bone scaffolds, and innovative biomaterials, soft robotics, smart wearables, and microfluidic devices.[38,39]

2.1.3. Continuous Liquid Interface Production (CLIP)

To further improve the light-based 3D printing, DeSimone et al. designed and assembled a new 3D printing method called CLIP, which used an oxygen-permeable window below the ultraviolet (UV) light source as a "dead zone" for the persistent liquid interface and layerless processing shown in Figure 2c.[40] This platform allows for photopolymerization at a high rate of hundreds of millimeters per hour, showing a significantly improved printing speed with acceptable processing resolutions. The unique advantages of CLIP are the quick curing speed, layer-less printing,

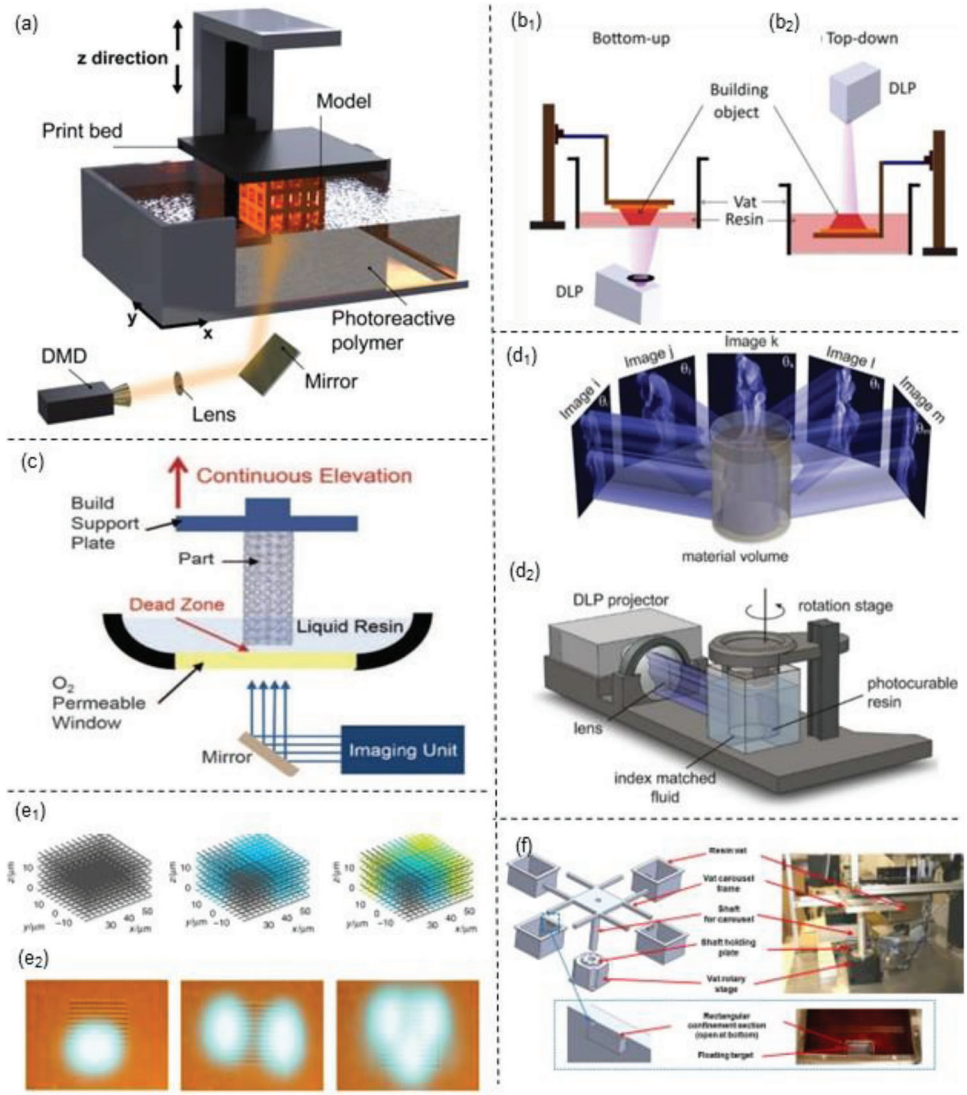

Figure 2. a) General stereolithography (SLA). b_1,b_2) Bottom-up and top-down digital light processing (DLP) configurations. Reproduced with permission.[38] Copyright 2022, Springer Nature. c) Schematic of the printing platform for continuous liquid interface production (CLIP). Reproduced with permission.[40] Copyright 2015, AAAS. d_1) The representation of the volumetric computed axial lithography (CAL) printing platform and the d_2) manufacturing mechanism. Reproduced with permission.[46] Copyright 2019 AAAS. e_1) Two-photo polymerization (TPP) examples of using a single laser split into multiple points with e_2) simulation of the laser splitting up to three times covering most of the model. Reproduced with permission.[47] Copyright 2019, Springer Nature. f) Multi-photopolymerization (MPP) with possible multiple resin vats in a rotary stage set for high resolution and scalable 3D printing.[48] Copyright 2012, Elsevier.

and high accuracy. As a result, CLIP supports various production materials, such as cross-linkable monomers, rigid ceramics, and biological materials.[41,42] However, CLIP has still been slower than conventional methods, such as injection molding or mold casting. Therefore, in 2022 DeSimone et al. enhanced the CLIP design to the injection continuous liquid interface production (iCLIP), where a direct injection into the "dead zone" alleviates suction forces to accelerate printing speed up to five to ten folds over CLIP.[43] As an additional benefit, the iCLIP allows for multi-material printing due to the direct injection of photopolymerization materials. Ongoing research in CLIP has been focused on new materials and geometries with superior mechanical and electrical properties for intelligent systems (e.g., 4D printing) and on developing better predictive models for multi-material printing.[44,45]

2.1.4. Computed Axial Lithography (CAL)

CAL is based on tomography reconstruction inspired by computed tomography (CT), typically used in medical imaging.[46] Using photosensitive liquid in a volumetric rotational stage, the projected 2D images are displayed through light energy as the printing stage rotates and reconstructs the 2D images into 3D printable objects, as shown in Figure $2d_1$,d_2. This new manufacturing method does not need layer-by-layer deposition as in

DLP or CLIP, thus enabling exceptionally smooth surfaces and rapid fabrication. Besides, it does not require support structures, even with overhanging features or separate parts.[46] In addition, CAL allows for new highly viscous photopolymer materials to be printed, whereas traditional SLA or other conventional photopolymerization methods could not. Therefore, the usability of CAL can be extended in general photopolymers and their composites containing reasonable loading of glasses, ceramics, and metal powders.[45,46,49]

2.1.5. Two-/Multiphoto Polymerization (T/MPP)

Another AM method with ultrafast nanofabrication was developed by Geng et al. using a TPP process in conjunction with a DMD scanner.[47] The DMD allows for a single-focus or multi-focus hologram generation laser scanning, enabling the laser to split into multiple focal points for an ultrafast print without compromising the pattern resolution illustrated in Figure 2e$_1$,e$_2$. It is worth noting that the total printing time remains constant regardless of the sequence or complexity. Henceforth, the TPP equipped with the ultrafast random-access DMD scanner gives a precise 3D printing process with complex structures through advanced photonic resin for nanoscale applications.

The MPP can create small features in a photosensitive material without the need for complex optical systems or photomasks. This method relies on the multi-photon absorption process in a transparent material, using a laser to create patterns. By scanning and modulating the laser, a chemical change, typically polymerization, occurs at the focal spot, allowing for the creation of 3D patterns.[48] However, high-resolution printing using MPP often comes at the cost of slower printing speeds and limited scalability. One possible solution is to combine MPP with other techniques, such as hybridization with multiple resin vats as shown in Figure 2f.[48] This approach enables sequential printing of different materials, allowing for the creation of multi-material structures. It is important to note that MPP is commonly employed in DLP configurations due to the flexibility and versatility it offers. MPP holds great potential in the 3D printing industry, particularly in terms of enhancing the mechanical, optical, electrical, and biological properties of printed objects.

2.2. Filament-Based 3D Printing

2.2.1. Fused Deposition Modeling (FDM)

FDM is a popular 3D printing technique known for its layer-by-layer deposition of mostly thermoplastic polymers (i.e., polylactic acid (PLA), acrylonitrile butadiene styrene (ABS), polyethylene terephthalate (PET), polyether ether ketone (PEEK), polyphenylene sulfide (PPS), polycaprolactone (PCL)). FDM printers typically come in Cartesian and delta models.[50,51] The main difference between these two is the movement linearity of the print beds. Precisely, the Cartesian model moves linearly via Cartesian coordinates, while the delta model moves circularly with its print bed featuring a circular motion. Standard features for these models include a heated nozzle to soften/melt filaments. For example, two stepper motors connected to the extruder head facilitate pushing the filament by gripping the filament wire to prevent slippage and depositing it into the substrate. Generally, the substrate will move in the x/y (Cartesian model) or radial/tangent (delta model) directions while the nozzle/extrusion mechanism moves in the z-direction. With a similar goal for 3D structural control, the printhead can also be based on a mechanism to move along the in-plane (i.e., x/y-direction or rotational) while the substrate moves along the out-of-plane (i.e., z-direction).

It is worth noting that the FDM mechanism is reliant on the deposited layer to cure/harden and build upon the previous layer to achieve complex structures. One of the tradeoffs for FDM is the printing resolution, which decreases as the printing speed increases. To rectify this issue, introducing multi-material/multi-nozzle printing allows for faster feedstock deposition without sacrificing the printing speed. **Figure 3**a$_1$–a$_4$ show printing setups with different printhead configurations for individual or multiple feedstocks to be extruded via one or more printheads. Multifilament mono-extruder printing, represented in Figure 3a$_1$, utilizes a filament selector, similar to the mono-filament, but selects a single filament to print and can change to a different filament without the need for any human interference (e.g., Ultimaker S model). Alternatives can be multifilament through multiple independent (Figure 3a$_2$, e.g., Flashforge) dual extruder FDM as shown in Figure 3a$_5$ or dependent printing nozzles (Figure 3a$_3$, e.g., Createbot). Mono-filament extrusion, shown in Figure 3a$_4$, is a neat feature that uses an individual feedstock that is either single-phased or may combine multiple materials to create a mono-filament layer through the extruder.

While independent extruders are available in the market, having more than two is not expected due to the difficulty of calibration, the complexity of nozzle movement, and conflicts of temperature control, as viewed in Figure 3a$_2$. For example, the dependent multi-extruder-based printhead in Figure 3a$_3$ is a unique configuration where the extruders are all on the same axis and are not free to move and deposit feedstocks independently.[52] Further manufacturing features to consider during 3D printing may include i) material factors (i.e., melting temperatures, viscosity behaviors, solidification rates), ii) machine factors (i.e., nozzle sizes, fiber supply), iii) process parameters (i.e., feed rate/printing speed, raster width/gap/angle, contour width/thickness, layer thickness/orientations), and iv) environmental factors (i.e., the temperature of the nozzle/bed/chamber, humidity degrees, oxygen content).

2.2.2. Direct Ink Writing (DIW)

DIW is the most versatile technique due to its broad range of printing feedstocks in colloids, solutions, and gels. Any polymers and powders can be used if the fluidic ink meets rheological requirements/behavior.[53,54] Generally, the inks should experience shear thinning when extruding, behave as a yield-stress-decreasing fluid during ejection, and recover their elastic properties after printing.[53-55] Most inks require a post-treatment healing process after printing (i.e., liquid evaporation, gelation, thermal treatment, and solvents for etching/debinding materials).[54] The printing platform consists of an ink depositor/dispenser (i.e., syringe pump, delivery path), an extruder nozzle with tunable sizes, a substrate, and printable ink, as shown in Figure 3b$_1$. The

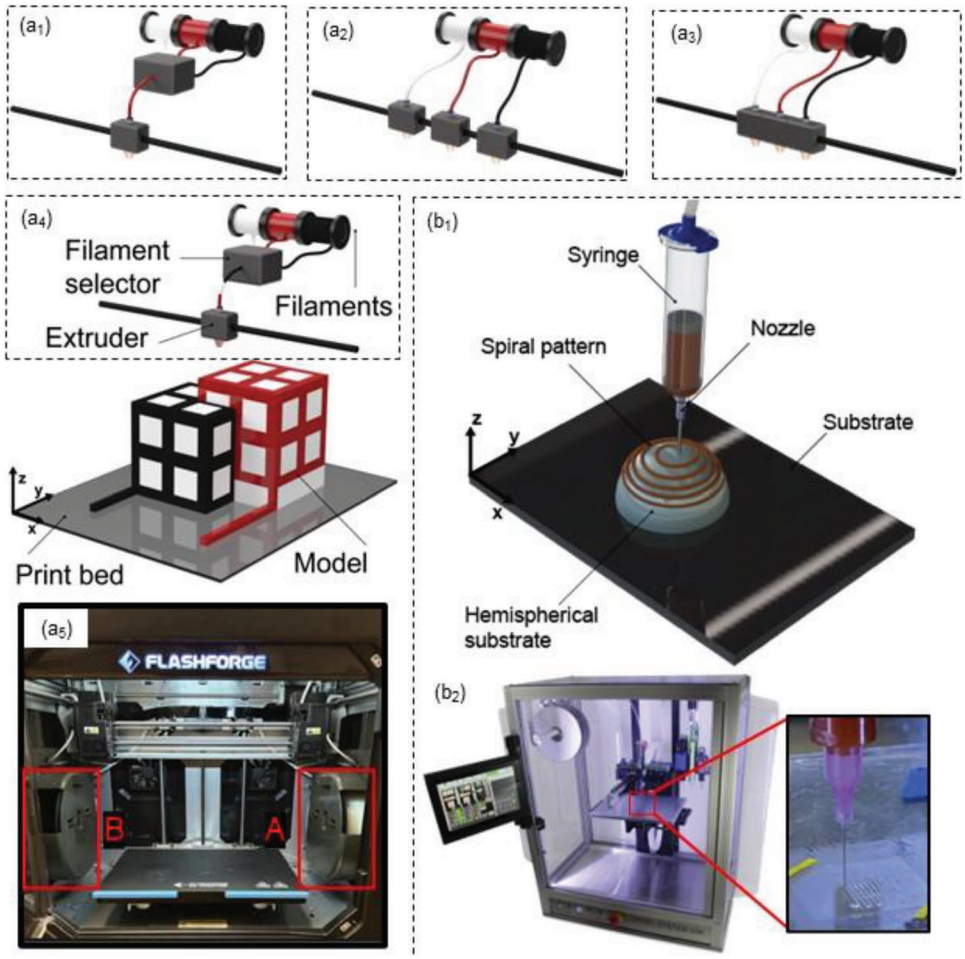

Figure 3. a_1–a_4) Schematic illustrations of the different multi-material fused deposition modeling (FDM) configurations. a_1) Monoextruder with selective feedstock from multifilament setting, a_2) multi-extruder multifilament with independent printheads, a_3) multi-extruder multifilament with dependent printheads, a_4) mono-extruder setting with a concept multi-material print, and a_5) an example of multifilament multi-extruder 3D printing platform, i.e., Flashforge multimaterial printer with a dual-extruder-based setup having independently controlled printheads. b_1) Direct ink writing (DIW) concept with a 3D spiral pattern printed on a hemispherical substrate with b_2) an example of DIW platform, i.e., Hyrel 3D printer with a customized printhead connected with high-pressure dispensers for designing and processing cellular solids.

simplicity of the mechanism allows structural freedom, environmental stability, biological multifunctionality, and cost-effective manufacturing methods. In addition to being highly platform-customizable, the DIW also allows it to be more multi-material versatile. Figure $3b_2$ shows an example of a Hyrel 3D printer used as a DIW with modular printing accessories and tunable hierarchies. It is also worth noting that the freedom to print directly in 3D substrates is superior to other mechanisms (e.g., flat or non-flat printing substrate, as in Figure $3b_1$). However, DIW has been limited by liquid-based inks (e.g., solutions, suspensions, gels) that require strict curing or hardening strategies.[54] Besides, the scalability and safety of ink design/preparation remain a concern regarding hazardous materials. For example, limited nonconductive materials (e.g., macromolecules) must be added to the active materials to increase printability and maintain good electrochemical performance for energy storage devices. Some typical additives include stabilizers, surfactants, and viscosity modifiers.[54] These additives allow for fine tunability to printability but should be washed through high temperatures after printing.

2.3. Powder Bed Fusion (PBF)-Based 3D Printing

2.3.1. Selective Laser Sintering (SLS)

SLS involves feeding powders and rapidly heating them to fuse the powder surfaces via neck formations or phase changes for specific shapes, sizes, and structures as shown in **Figure 4**a. Unlike the FDM, which fuses continuous filaments, the SLS fuses noncontinuous particles for complex solid-state dimensions. Based on the state of the sintered phases, the sintering process can be categorized either as a solid-state shown in Figure $4b_1$, more common in SLS, or a liquid phase with binder coatings or mixtures, as viewed in Figure $4b_2$. Compared to the particle fusing in solid-state, the liquid-state sintering would rely on binders to display liquid-like behaviors upon heating and gluing particles together. SLS powder bed can be composed of a single material or multi-materials with binders.[56] However, SLS primarily uses semicrystalline thermoplastic polymer and, in some cases, amorphous polymer powders.[42,57-59] Characteristics for the

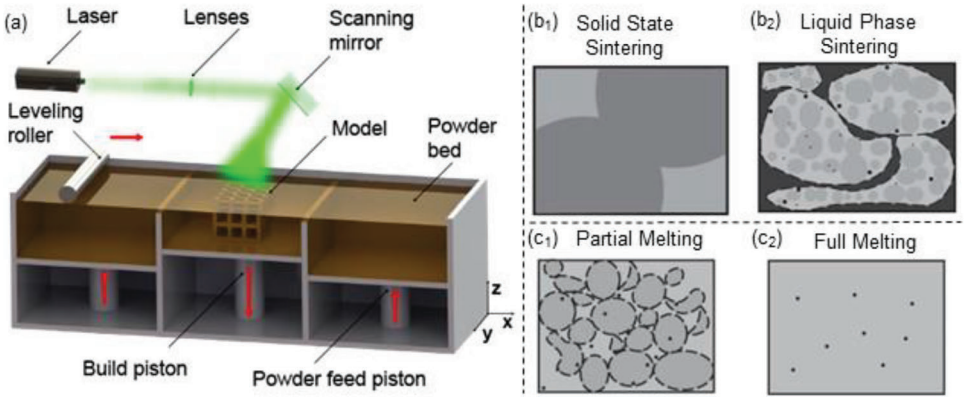

Figure 4. a) Schematic of the manufacturing platform of powder-bed-fusion-based 3D printing, i.e., selective laser sintering (SLS) & selective laser melting (SLM) representing their close similarities in the manufacturing tools. Representation of the main difference printing method for SLS in b_1) solid-state sintering (SS), where powders are compressed and heated under pressure to create a solid mass. In contrast, b_2) liquid-phase sintering involves the addition of a small amount of liquid to the powder mixture before sintering. Schematic of the printing difference for the SLM in both c_1) partial melting, where a portion of the material gets melted, and c_2) full melting, where the entire material is melted.

feedstock powder quality include size, distribution, shape, flowability/viscosity, surface tension, surface charges, and transition temperatures of powders, each of which will influence the product quality, e.g., particle packing factor, surface roughness, or defect density.[60] Although SLS has shown advanced capabilities to process polymer and ceramic particles, further improvements over material candidates and manufacturing precisions are still needed. For example, many SLS platforms face challenges in underperforming and need to improve to match traditional manufacturing methods, such as high surface roughness or a lack of mass production capabilities. Besides, powder aggregation due to electrostatic forces and heterogeneity from the particle synthesis in the powder feedstock are vital factors negatively affecting printed product performance. Additionally, the SLS manufacturing process is more expensive and complex to operate than the conventional processing of casting, molding, or other smaller-footprint printers (e.g., FDM, SLA).

2.3.2. Selective Laser Melting (SLM)

SLM has a similar setup to the SLS and works with approximately the same procedures. The main difference is in the materials, as SLS uses primarily metal particles, which leads to SLS fusing particles thermally, while SLM uses the complete melting of materials. SLM was developed to produce fully dense objects (i.e., smaller layer thickness, smaller pores) with higher mechanical properties, in addition to the benefit of avoiding prolonged post-processing cycles typically seen in SLS.[61] There are two different degrees of melting, for example, partial melting, typically seen when a partial section turns into a liquid state through melting, represented in Figure 4c_1. As the name suggests, complete melting is when an entire area is intended to melt completely, which is often the case in metallic SLM, represented in Figure 4c_2. However, "partial melting" and "full melting" are ambiguous, especially when the intention is to have near-full densified parts.[61] It is worth noting that both polymers and metals are compatible with SLM. Nonetheless, it is more commonly seen in metal 3D printing, where there are different configurations for metal-based 3D printing, such as single component/single powder and single component/multiple alloyed powder particles. Generally, the powder particles range from 20 to 50 μm in diameter, and a single layer thickness ranges from 20 to 100 μm.[62] For those with a laser beam of a bandwidth smaller than 40 μm (e.g., lasers of Nd:YAG, fiber, CO_2), a layer thickness of less than 10 μm and a particle size of less than 10 μm would be formed to be considered a μ-SLM.[62]

2.4. Jetting-Based 3D Printing

2.4.1. Inkjet-Based 3D Printing of PolyJet and MultiJet

Inkjet-based printers deposit and solidify polymer powders layer by layer through a jetting head, followed by built-in UV irradiation, heat transfer, or chemical reaction. The MultiJet (from 3D Systems) and PolyJet (from Stratasys) are currently the major commercialized 3D printers based on a material jetting (MJ) mechanism.[63,64] The printer heads would jet liquid resins or particles through tiny needles selected from many linearly aligned nozzles during the MJ shown in **Figure 5**a. In this way, the jetting droplets will disperse with highly complex geometries and high surface smoothness. As a result, surface finishing is not mandatory since layer dimensions at the microscale are possible.[64] Commercial companies provide proprietary jetting inks, from rigid plastics to flexible urethane-acrylate. These inks are immediately UV/thermally cured and solidified upon jetting to build the 3D structure during crosslinking or fusing as responses to external energies represented in Figure 5a. For example, curing reactions can be performed by dispersing two reactive components using alternative nozzles induced by heat or UV light (e.g., UV curing of photoresponsive monomers, and the nanoparticle (NPs) may require thermal curing or annealing). In addition to these sprayable or injectable inks, support materials are often used during the printing process to form overhangs that are removable through solvent dissolution or mechanical means such as peeling or scraping. The layer deposition repeats can be spatially designated to create structures with spatially

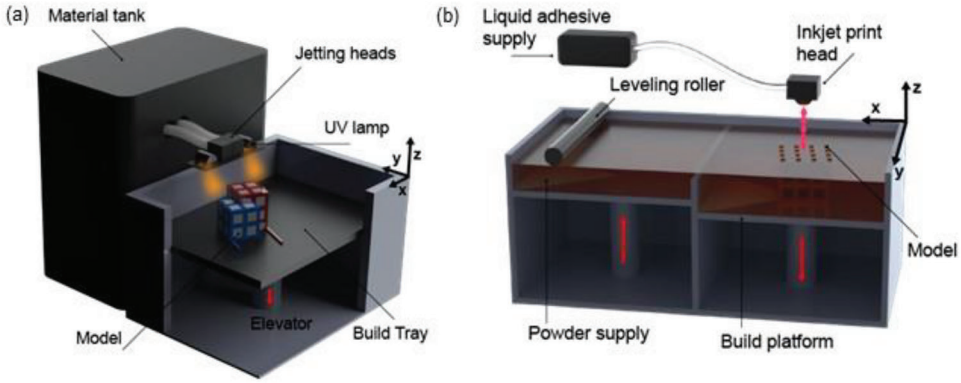

Figure 5. Examples of jetting-based 3D printing techniques. a) Illustration of inkjet-based 3D printing process utilizing a double ultraviolet (UV) irradiation-facilitated curing process on a stack cube model. The ink droplets are deposited and cured layer by layer to create the 3D structure. b) Schematic of binder jetting-based 3D printing process with a powder bed, leveling roller, and two different platforms for powder supply and printing. The binder is selectively deposited to bind the powder particles layer by layer, forming the 3D object.

varying or graded features. Functionally graded designs are also manufacturable by depositing materials with different ratios or chemistries (e.g., methacrylate or acrylate).[65] Inkjet-based 3D printing can process vendor-sold colloids and in-house prepared monomers, polymer solutions, or NP dispersions.

2.4.2. Binder Jetting-Based 3D Printing

Binder jetting-based printing deposits a binding material onto one powder layer and forms 3D structures to repeat this process.[66] As a result, binder jetting-based 3D printing involves powders and adhesive binders without external energies, illustrated in Figure 5b. In comparison, PBF 3D printing also involved similar powder materials.[66] However, PBF depends on material sintering and melting from laser sources as extra energy contributions. Besides, this binder jetting technology allows multi-material processing, including multi-colored printing across the whole color spectrum. Binder jetting in powders gives access to a broader range of materials, including polymers, ceramics, metals, and combinations, to manipulate their physical, mechanical, and chemical properties.[67–69]

3. 3D-Printing Electrodes

Conventional LIBs with thin film electrodes face many challenges related to poor ionic conductivity, energy density, safety, and cycling stability. The mass loading of active materials per footprint is typically low due to the trade-off between energy and power density, increasing the inactive material ratio (current collectors and separators).[70,71] Therefore, the primary goal of improving battery performance is to reduce the proportion of inactive materials while increasing the percentage of active materials to optimize energy storage capacity. Thick electrodes would decrease the use of current collectors and separators and increase the active material ratio. In effect, the transport distance of Li-ions and electrons increases with thick electrodes, resulting in declined rate performance due to the slow charge transfer kinetics.[71] With the capability of desirable layer deposition, 3D-printing technology can design and process directionally ordered pores within the electrodes to mitigate this risk. **Tables 2** and **3** list the 3D printing methods that are commonly used for anode and cathode electrodes and show trends in processing techniques and printing materials. For example, FDM and DIW are popular in 3D printing due to the easy use of filaments/inks.[53,54] Printing feedstock-wise, the anodes are primarily comprised of lithium titanium oxide (LTO), with the cathodes dominant of lithium iron phosphate (LFP). LTO has high rate capability, long cycle life, and stability, due to its ability to intercalate the Li-ions, making it a suitable electrode for high-power applications. Ni–Sn & SnO_2 are also commonly used for higher theoretical capacity. Similarly, AgNP@CC is known for its high electrical conductivity, while GO has a high surface area and can be used for energy storage and conversion devices requiring high cycles. Henceforth, this section will systematically discuss different AM techniques for anode and cathode materials. The specific details for the LIB application regarding the material types, manufacturing procedures, and cell-assembly characteristics will be discussed.

3.1. 3D-Printing Anode Materials

3.1.1. Light-Based 3D Printing for Anodes

SLA printing is a well-established AM technique that has gained prominence in ESS, particularly in the field of anodes and solid electrolytes. For example, Golodnitsky et al. developed a quasi-solid rechargeable 3D microbattery via SLA 3D printing.[72] One of the main challenges that batteries face is the low power and capacity, which the short ion-diffusion path could mitigate. Increasing the thickness can achieve a better capacity, but it may also hinder ionic kinetics by increasing the current path and reducing power density. Therefore, more complex 3D architectures are necessary, which convert the entire thin-film battery into a network placed on a small footprint (e.g., **Figure 6**a_1).[72] Figure 6a_2,a_3 illustrates the cross-section of the full cell with the juxtapose film layers on the nickel (Ni)-current collector, cathode, polymer membrane as the separator, and LTO-contained anode. As a result, the fabrication of 3D microarrays in the form of cylinders with Cartesian coordinate grid holes was conducted. However, the microarray morphology was not limited to

Table 2. Examples of AM methods for anodes used in LIB. See terminology below and also in Section 6 (AgNPs, silver nanoparticles; AgNWs, silver nanowires; CC, carbon cloth; CMC, carbon methyl cellulose; DIW, direct ink writing; DLP, digital light processing; FDM, fused deposition modeling; GO, graphene oxide; Gr, graphene; Gt, graphite; KB, ketjenblack; LAGP, $Li_{1.5}Al_{0.5}Ge_{1.5}P_3O_{12}$; LFP, lithium iron phosphate; $Li_{0.7}$PAA, lithium poly(lactic acid); LiM, lithium metal; LMO, lithium manganese oxide; LNMO, lithium nickel manganese oxide; LTO, lithium titanium oxide; Mg, magnesium; MWCNT, multiwalled carbon nanotube; N/A, not applicable; NaOH, sodium hydroxide; Ni, nickel; Pd, palladium; PEDOT:PSS, poly(3,4-ethylenedioxythiophene) polystyrene sulfonate; PF, phenolic resin; PLA, polylactic acid; PVP, poly(vinylpyrrolidone); Si, silicon; SiNP, silicon nanoparticles; SiO, silicon monoxide; SLA, stereolithography; SLS, selective laser sintering; Sn, tin; SnO_2, tin(IV) oxide; WPF, pinewood powder; Zn, zinc).

	Manufacturing					Materials		Properties				Refs.
Anode	Method	Print diameter [μm]	Speed [mms^{-1}]	Layer Number	Post-treatment	Particles	Additives	Cell assembly	Specific capacity	Voltage	Cycles	
	SLA	20	–	1	Air drying etching	LTO	$Li_{0.7}$PAA	Full-Cell (LTO/LAGP/LFP)	400–500 (μAh cm^{-2})	1.9–3.2	200	[72]
		15	–	1,2,3	Etching	Ni–Sn	photoresist (AZ9260) (III) and Ni	Half-cell (LMO/Ni–Sn)	–	0.0–3.2	200	[74]
	DLP	0.0018	–	1	N/A	Zn	GO	Symmetric-cell (3DGr@Zn)	3.76 and 3.13 (mAh cm^{-2})	0.12–0.27	500	[75]
		40-60	≈0.28	40	Debinding Sintering	SnO_2	Camphor quinone	Full-Cell (Sn/Ni)	100-1000 (mAh g^{-1})	1-2.5	50	[73]
	FDM	1.4–1.75	–	≈1-2	Vacuum drying	LTO	PLA	Half-cell (LTO/LiM)	80 (mAh g^{-1})	2.6–3.8	100	[76]
		1.75	40	≈1	Air drying	LTO	Gt, PLA	Half-cell (LTO/LiM)	3.34-4.84 (mAh cm^{-3})	2-3	100	[77]
		1.75	0–200	1	N/A	Gt	PLA	Half-cell (Gt/LiM)	200 (mAh g^{-1})	–	6	[78]
		1.75	30	–	Chemical (NaOH)	Gr	PLA	Half-cell (Gr/LiM)	500 (mAh g^{-1})	0.01–3	60	[79]
		–	–	≈5	N/A	Gr	PLA	Half-cell (Gr/LiM)	40 (mAh g^{-1})	0.01–3	3-120	[80]
	DIW	100	5	6	Freeze-drying	LTO	GO	Half-cell (LTO/LiM)	169 (mAh g^{-1})	2–4	20	[81]
		205	2	10	Freeze-drying	LTO	GO, AgNWs	Half-Cell (LTO/LiM)	4.74 (mAh g^{-1})	1–2.5	100	[82]
		100	–	16	N/A	LTO	KB, PVP	Full-cell (LTO/LFP)	4.45 (mAh cm^{-1})	1–2.6	2	[83]
		60-100	4–8	6,12,18	Freeze-drying	LTO	CMC, acetylene black	Half-cell (LTO/LiM)	4.8 4.45 (mAh cm^{-1})	1.2–2.4	100	[84]
		210	4–8	4,8,12	Freeze-drying	LTO	KB, MWCNT	Half-cell (LTO/LiM)	145 (mAh g^{-1})	1–2.5	100	[71]
		100	1	7	Vacuum drying	Gt	SiO_2	Full-cell (Gt-(Gt-SiO)/LNMO)	3.52 (mAh cm^{-2})	3.5–4.85	120	[85]
	SLS	10.5	<1	20	Etching, purifying, drying	Gr	Ni/sucrose	–	–	–	–	[86]
		10	–	1	N/A	Mg	Mg_2Cu $MgCu_2$	Half-Cell (Mg/LiM)	250 (mAh g^{-1})	0.005–1.5	10	[87]
		100	2500	1	Vacuum drying	Carbon	PF, WPF	–	–	–	–	[88]
	Inkjet	–	–	25	N/A	Si	PEDOT: PSS	Half-cell (SiNP/LiM)	1714 and 961 (mAh g^{-1})	0.01–0.25	100	[89]
		80	50	8	N/A	Gr	Ethyl-cellulose	Half-Cell (Gr/LiM)	942 (mAh g^{-1})	0.01–3.0	100	[90]
		60	–	47.7	Annealed	AgNP@CC	Carbon	Half-Cell (AgNP@CC/Zn)	184 (mAh g^{-1})	-0.3–- 1.0	1200	[91]
	Binder Jetting	100	–	3	De-powdering impregnation of Pd	GO	Phosphoric acid	–	430 (mF cm^{-2})	0.0–1.0	1000	[92]

Table 3. Summary and comparison of 3D printed cathodes for LIB. See terminology below and also in Section 6 (Al, aluminum; CNT, carbon nanotubes; ITO, indium tin oxide; LMFP, lithium manganese iron phosphate; NCA, lithium nickel cobalt aluminum; NMP, N-Methyl-2-Pyrrolidone; PC, propylene carbonate; PEI, polyethylenimine; PVDF, polyvinylidene fluoride; PVDF-co-HFP, poly(vinylidene fluoride)-co-hexafluoropropylene; SCMC, sodium carboxymethyl cellulose; Se, selenium; SY LEP, super yellow light-emitting polymer; THF, tetrahydrofuran; ZnO, zinc oxide).

Cathode	Manufacturing					Materials		Properties				Refs.
	Method	Print diameter (μm)	Speed (mm/s)	Layer Number	Post-Treatment	Particles	Additives	Cell Assembly	Specific Capacity	Voltage	Cycles	
	SLA	15	–	1,2,3	Etching	LMO	Photoresist (AZ9260) (III) and Ni	Full-cell (LMO/Si-Np)	–	0.0–3.2	200	[74]
		20	–	1	Air drying etching	LFP	–	Full-cell (LTO/LAGP/LFP)	400–500 (μAh cm^{-2})	1.9–3.2	200	[72]
	FDM	1.75	–	≈4	N/A	LFP	PLA	Half-cell (LFP/LiM)	15 (mAh g^{-1})	2.6–3.8	10	[94]
		1.4–1.75	–	≈1-2	Vacuum drying	LFP	PLA	Half-cell (LFP/LiM)	60, 50, 20 [mAh g^{-1}]	2.6–3.8	100	[76]
		150–200	5,6	2,5,10	Freeze-drying	Se	CNT	Half-cell (Se-x/LiM)	538.1 (mAh g^{-1})	0.8–3	200	[95]
		1.75	40	100	Air drying	LMO	MWCNT, PLA	Half-cell (LMO/LiM)	6.99–8.1 (mAh cm^{-3})	3.3–4	100	[77]
	DIW	100	5	6	Freeze-drying	LFP	GO	Half-cell (LFP/LiM)	170 (mAh g^{-1})	2–4	20	[81]
		100	–	16	N/A	LFP	KB, PVP	Full-cell (LFP/LTO)	4.45 (mAh cm^{-1})	1–2.6	2	[83]
		250	2	2,4,8,10,12	Freeze-drying	LFP	PEDOT: PSS	Half-cell (LFP/LiM)	5.63 (mAh cm^{-1})	2–4	100	[96]
		60	1–30	150–550	Calcination	LMFP	PVDF	Half-cell (LMFP/LiM)	150.21 (mAh g^{-1})	2–4.5	1000	[97]
	SLS	0.4–1.0	17,21,25	100	N/A	NCA	–	–	167.7 ± 7.6 (mAh g^{-1})	–	–	[98]
		0.4–1.0	17,21,25	100	N/A	NCA	–	–	167.7 ± 7.6 (mAh g^{-1})	–	–	[98]
	Inkjet	50	–	1	Sintering	ITO	(Al:ZnO:PEI)	ITO/(Al:ZnO:PEI)/SY LEP/DEDOT: PSS	–	–	–	[99]
		20	–	1	Vacuum drying	LFP	CB and SCMC	Half-cell (LFP/LiM)	134.7 and 129.9 (mAh g^{-1})	2.0–4.0	9	[100]
		1.4	–	1	Air drying	MnO_2	PC, (PVDF-HFP), THF	N/A	270 (mAh g^{-1})	0.5–1.7	–	[101]
	Aerosol	80	–	1	Calendering	LFP	Carbone, NMP	Half-cell (LFP/LiM)	140 [mAh g^{-1}]	2.5-4.0	100	[102]
		170	–	1	Vacuum drying	LFP	Carbone, Kynar 1800, NMP	Half-cell (LFP/LiM)	105 to 151 (mAh g^{-1})	3.4	50	[103]

NANO · MICRO small
www.small-journal.com

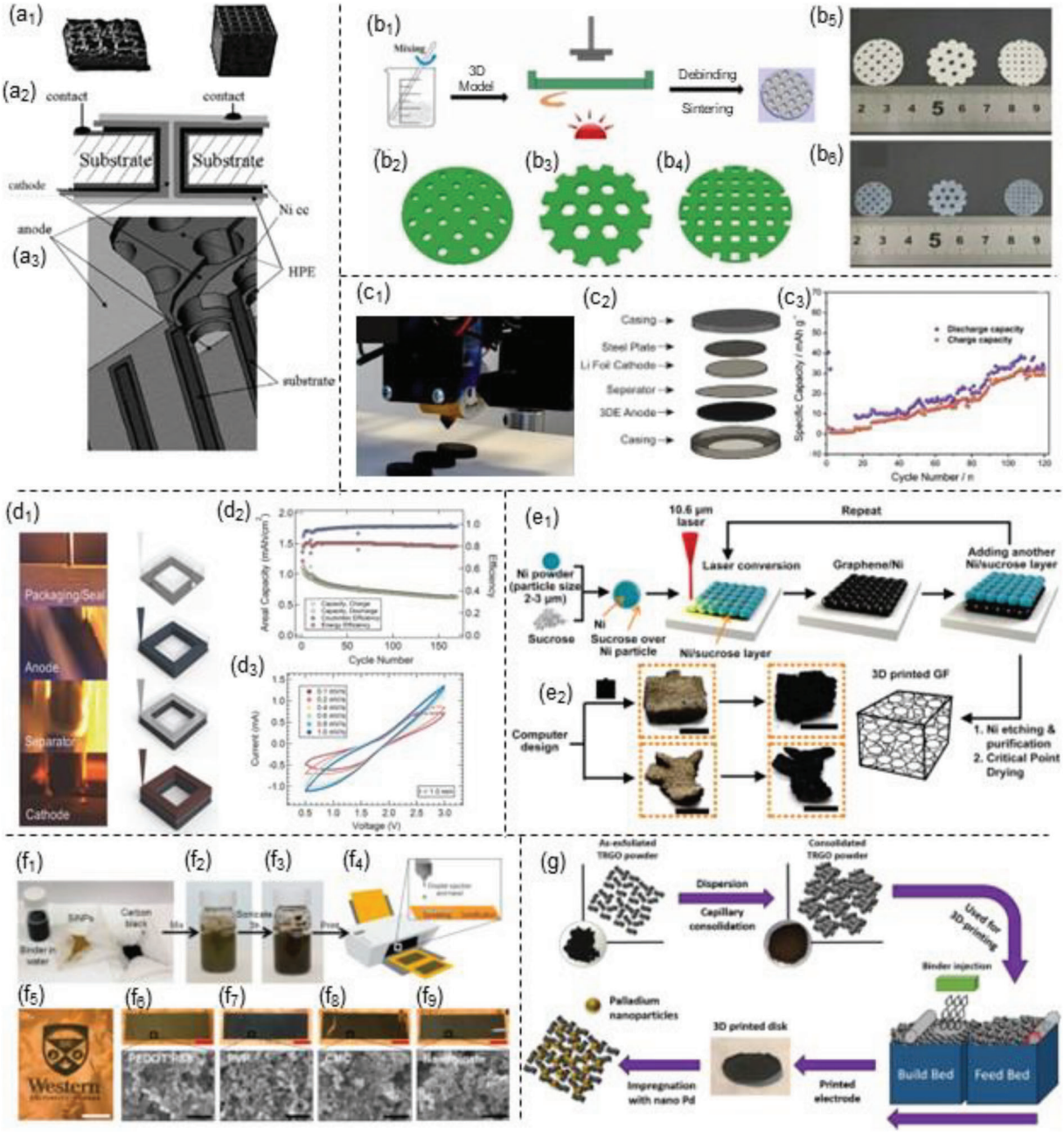

Figure 6. a_1) Photos of the SLA-printed polymer-based substrates for electrode applications. a_2–a_3) Cross-sectional view of the nickel (Ni)-based current collector as the substrate, the cathode, the polymer membrane, and the anode contact points. Reproduced with permission.[72] Copyright 2018, Elsevier. b_1) DLP diagram of SnO_2-based porous anode electrode with b_2) round holes, b_3) hexagonal holes, and b_4) square holes in configuration. b_5, b_6) Photos illustrating the printed electrodes before and after the debinding and sintering processes with different porous configurations for anodes. Reproduced with permission.[73] Copyright 2023, Elsevier. c_1) FDM printing for graphene (Gr)-based electrodes with the c_2) casing configuration and the corresponding c_3) charge/discharge cycles with the specific capacity. Reproduced with permission.[80] Copyright 2017, Scientific Reports. d_1) DIW manufacturing method of an entirely 3D printed LIB (e.g., cathode, separator, anode, and packaging seal) with corresponding d_2) current versus voltage (*C*–*V*) graph and d_3) areal capacity showing *C*–*V* relationship as a function of the cycle number for the fully 3D printed battery. Reproduced with permission.[83] Copyright 2018, Wiley-VCH. e_1) Schematic representation of the 3D printed Gr foams via SLS with e_2) the comparison between different computer design models before and after printing, showing consistent processability. Scale bars are 5 mm. Reproduced with permission.[86] Copyright 2017, American Chemical Society. f_1–f_4) Representation of processing 3D printable silicone NPs via an Inkjet printer. f_5) Example of the "Western University" logo printed on a copper foil in addition to optical images and scanning electron microscope (SEM) images of f_6) poly(3,4-ethylenedioxythiophene) polystyrene sulfonate (PEDOT: PSS), f_7) poly(vinylpyrrolidone) (PVP), f_8) carbon methyl cellulose (CMC), and f_9) Na-alginate. Scale bars red, white, and black represent 3 cm, 5 cm, and 500 nm, respectively. Reproduced with permission.[89] Copyright 2017, Elsevier. g) Schematic illustration of the binder-jetting technique by first introducing thermally reduced graphene oxide (TRGO) powders, then dispersing them in a capillary consolidation powder to spread onto a feed bed. After the binder injection to create 3D-printed disks, the impregnation of nano palladium (Pd) is implemented to improve the performance of the electrode. Reproduced with permission.[92] Copyright 2017, Elsevier.

honeycomb, triangular, or cylindrical shaped holes, providing more freedom in tuning the density of the models as well as the mechanical strength. Figure 6a_1 shows an example of a 3D-printed anode later tested into a full-cell configuration. The electrochemistry characterization showed acceptable cyclability with an areal capacity of 400 to 500 μAh cm^{-2} tested at a rate from 0.1 to 4C. In addition, when comparing the model for a silicon (Si) chip, it has at least one order of magnitude higher in areal capacity than the commercial system. In contrast, the model with the 3D printed polymer substrate is three times larger by volume than the planar thin-film batteries.[72]

DLP is another method used in light-monomer interactive printing. For example, Chen et al. used DLP and fabricated zinc-ion battery electrodes with circular, hexagonal, and square holes (Figure 6b_1). As shown in Figure 6b_2–b_4, these porous channels had different inner diameters of 1.5 mm, 2 mm, and 1 mm, keeping all the heights constant at 1.5 mm.[73] Figure 6b_1 illustrates the general fabrication of the SnO_2-based porous anode in a three-step process (i.e., mixing, printing, and debinding/sintering). It is worth noting that the debinding/sintering process shrank the printed anodes, as shown in Figure 6b_5,b_6. To minimize the shrinkage, the anode was doped with Sb_2O_3 at 0.5, 3, 6, and 9 wt%, which caused an average shrinkage of 26.6, 26.8, and 32.3%, respectively, while keeping a relative density of 73.5%.[73] Compared with traditional fabrication methods, these DLP printed anodes showed a 1/25 reduced charge transfer impedance, better cycle stability and rate performance, and improved capacity retention by ≈29%. Hence, this work demonstrated the potential of using DLP as a manufacturing method to improve high-load porous, thick electrodes used for batteries.

3.1.2. Filament-Based 3D Printing for Anodes

FDM is known for its simplicity and rapid prototyping of anodes of any shape and size, using filaments and a heated nozzle for deposition. For example, Banks et al. demonstrated an FDM printable electrode via graphene (Gr)-based PLA filaments, as shown in Figure 6c_1.[80] Though the output/performance of the half-cell assembly shown in Figure 6c_2,c_3 was not highly competitive compared to previous literature, this method did not require a metallic current collector for the LIB, which could reduce the manufacturing cost. Similarly, Golodnitsky et al. 3D printed a complete microbattery via FDM.[76] For the anode material, the LTO and PLA were synthesized into printable discs, spiral, and double-spiral shaped composites. While the results only used about 50 to 60% of the theoretical capacity, they proved the capability of printing a biodegradable electrode for the LIB application. Furthermore, Wiley et al. demonstrated the FDM printability of LTO/PLA electrodes.[77] Their work showed a printable profile for a full battery, with a high loading of active fillers into the polymer (i.e., a maximum of 30%). Due to the constraint of low active material in the PLA, the performance was about two magnitudes lower than the LTO and LMO electrodes.[77] Maurel et al. also demonstrated FDM printable graphite (Gt)/PLA electrodes.[78] In their studies, the Gt load was used as high as possible to increase electrochemical performance, while the amount of plasticizer was optimized to be at a 40% ratio of the PLA to increase ductility and decrease stiffness.[78] Most recently, Banks et al. used the same material composition of Gr/PLA via FDM manufacturing.[79] However, they introduced a new post-treatment method using NaOH to create micro-porous within the electrode matrix while maintaining its 3D structure. More importantly, the pre-treatment significantly enhanced the charge and discharge profiles by a 200-fold increase in the specific capacity.[79]

Similarly, DIW can be helpful for 3D printable anodes when the filaments are not feasible. For example, Hu et al. DIW printed graphene oxide (GO) in electrodes featuring a fully 3D-printed battery.[81] GO was used in the LTO electrode as an anode in 6, 12, and 18 layers for the thick electrodes. The GO-based inks showed excellent rheological properties maintaining high apparent viscosities and shear thinning behavior, benefiting DIW printing. The performance validation was done in a half-cell configuration with a capacity of 171 mAh g^{-1} after 10 cycles, indicating a stable charge transfer and good electrochemical conductivity, as shown in Table 2.[81] Likewise, carbon black (CB) and carbon nanotubes (CNTs) are compatible with DIW printable inks and can also increase the electrical conductivity in electrodes. For example, Lewis et al. used conductive ketjen (KB) carbon with a mixture between lithium salts (lithium bistrifluoromethane sulfonamide (LiTFSI)) and propylene carbonate (PC) to stabilize the active particles.[83] With optimized compositions, the square-based 3D printed battery, as shown in Figure 6d_1, displayed complex hierarchical structures potential for wearable electronics, sensors, and other complex geometries. Figure 6d_2,d_3 shows the areal capacity plots as a function of cycle numbers, while also displaying the current versus voltage profiles for the DIW 3D printed battery. Also, Chen et al. used highly conductive KB carbon and multi-walled carbon nanotubes (MWCNTs) to improve electronic conductivity.[71] Additionally, they focused on finding the effects of electrode designs (i.e., porosity, active material particle diameter, thickness, line width, and pore size) on their electrochemical performance. The study showed that introducing vertically aligned pores and increasing their porosity alleviated the trade-off between energy and power density at rates below 1.0C.[71] Nonetheless, when the discharge rate was over 2.0 C, the 3D-printed thick electrodes notably decreased their energy and power density. Hence, the application for their electrodes may be used in areas requiring a high energy density below 1.0C but not at a discharge rate over 2.0 C. Another example is Chen et al., who 3D printed porous electrodes with a high LTO concentration via DIW.[84] The unique curing process involved maintaining the printing chamber below −7 °C and storing the printed electrodes in a refrigerator at −20 °C for over 12 h.[84] They could print 6, 12, and 18 layer-LTO electrodes with exceptional values of ≈4.8 mAh cm^{-2} at a rate of 0.2C. After increasing the charge/discharge rate to 2.0 C, it maintained above ≈3.6 mAh cm^{-2}.[84] It also retained excellent cyclability in specific capacities after 100 cycles. However, their thick electrodes were more susceptible to degradation at higher charge/discharge rates of up to 5.0C and relatively slow kinetics of electrochemical reactions at higher rates due to the nature of the thick electrodes that slowed the ionic transportation. Most recently, Chen et al. developed a DIW printable gel for thick electrodes.[82] Using silver nanowires (AgNWs), Gr, and LTO as functional ink, they showed the electrodes capable of retaining 95.5% of their original capacity after 100 cycles.[82] Hence, their rate capability, areal capacity, mechanical strength, and conduc-

tivity showed competitive values in Table 2. Yet, Zhang et al. in 2021 decreased the swelling of the electrodes while preventing degradation and improving the ionic kinetics after extensive cycling by 3D printing a multilayer "biscuit" structure electrode.[85] Using Gt as the first gradient pattern followed by a mixture of Gt and silicon dioxide (SiO_2) in a 4:1 mass ratio known as (GS), they were able to achieve a multilayer biscuit structure via DIW deposition. The concept behind the biscuit structure was to constrain the volume expansion of the GS with two outer layers composed of Gt. Their unique structure improved ionic transportation while limiting the volume expansion of the electrode. Furthermore, their full cell (3D Gt@GS/lithium nickel manganese oxide (LNMO)) delivered a high reversible capacity of 5.3 mAh cm^{-2} at 1.8 mA cm^{-2} and good cycling stability (i.e., a reversible capacity of 3.52 mAh cm^{-2} at 3.6 mA cm^{-2} after 120 cycles).[85]

3.1.3. PBF-Printed Anodes

SLS is typically known for 3D printing metals. However, ceramics and polymers are also compatible with the SLS. For example, Tour et al. demonstrated the ability to print Gr foams via SLS by manually placing sucrose powder and Ni together to process in the SLS platform.[86] The sucrose powder acted as the solid carbon source while the sintered Ni metal served as the catalyst/template for the Gr to take shape. Figure $6e_1$ shows the in-situ synthesis of 3D Gr foams starting with the Ni powder (particle size 2–3 μm) and sucrose powder over the Ni particles. Afterward, the CO_2 laser around 10.6 μm in diameter fused/sintered the materials allowing the Gr/Ni to take the first layer shape. Then another coat of Ni/sucrose was added with the process being repeated. After the desired shape was achieved, the etching of Ni and purification was needed while drying and solidifying the material. Figure $6e_2$ shows the comparison of the computer design before and after printing, allowing the Gr formation to take place. While no characterization was performed for the LIB, the material was used as an anode in batteries. However, some preliminary work for the battery application was done using the same SLS method at the same year but added MWCNTs as a reinforcing bar which showed some improvements in the thermostability, storage modulus (290.1 kPa) and conductivity (21.82 S cm^{-1}).[93] It also showed a stable performance as an anode with an energy density of 32 Wh kg^{-1} with a 78% energy retention after 500 cycles of testing at high current densities of 6.50 mA cm^{-2}.[93] This work further paved the way for battery manufacturing via SLS 3D printing. Similarly, Hong et al. focused on magnesium (Mg) matrix anode via SLS 3D printing for LIBs.[87] Printing at 50 W with a laser size of 70 μm and without the need for CB or binders, the results showed particles being columnar crystals covering the entire surface of the printed area. This behavior was due to the instant vaporization and cooling deposition of the material during the SLS printing. The resulting nanostructure increased the surface area, providing greater access to lithium ions' insertion and extraction.[87] The porosity of the microstructure also helped with the expansion after charging and discharging, which prolonged the battery's cycle life. Due to the laser heat, a thin film of low-resistance intermetallic compound between the copper and Mg composed of Mg_2Cu and $MgCu_2$ was formed. This thin layer increased the bonding capability between the Mg and Cu substrate, buffered the expansion of the active materials, and increased the battery's cycle life. This study showed a stable SLS-made anode with a capacity exceeding 150 mAh g^{-1} after 10 cycles under a 0.1C current rate. Moreover, the anode showed high thermal stability, e.g., when the temperature increased to 55°C, the capacity increased to 250 mAh g^{-1} after 10 cycles under a 0.1C current rate.[87]

3.1.4. Ink-Based 3D Printing for Anodes

Inkjet printing is mostly used for homes and offices with recent applications in printing electrode materials for energy storage devices. For example, Sun et al. demonstrated the printability of thin film Si anodes via inkjet printing for LIBs while comparing four different types of polymer binders to achieve good electrochemical performance.[89] Figure $6f_1$ shows the mixture of binder polymers in water with silicone nanoparticles (SiNPs) and CB. The mixture was then sonicated for 3 hours before it was ready to be transferred into a cell-cleaned HP 61 cartridge to be printed, as shown in Figure $6f_2$–f_4. Note that the printing sheet was copper where the electrode was deposited (Figure $6f_5$) where the "Western University" logo was demonstrated. The printability and performance were compared between four different conductive polymers. Figure $6f_5$–f_9 show these polymer-based printing (i.e., poly(3,4-ethylenedioxythiophene) polystyrene sulfonate (PEDOT:PSS), poly(vinylpyrrolidone) (PVP), CMC, and Na-alginate conductive polymers, respectively) on the copper substrate. Among them, PEDOT:PSS binder had superior durability and performance, with a capacity retention over 1000 cycles at a discharge of 1000 mAh g^{-1} when compared to other conductive polymer binders. The anode displayed high capacities of over 1700 mAh g^{-1} for 100 cycles, which contributed to the rapid transfer of SiNPs as well as the flexibility to accommodate for large volume expansion during high charge and discharge rates. Another example of inkjet printing for anode electrodes in LIBs is from Gupta et al., who most recently fabricated a continuous graphene film on different substrates (i.e., glass and copper) via inkjet printing to demonstrate its versatility.[90] The graphene ink was composed of graphene and ethyl cellulose to be printed before being thermally annealed at 350 °C in an argon gas atmosphere for 1.5 h. It was found that the resistance decreased with the increased number of layers (8 layers to reach a low value of ≈0.15 kΩ sq^{-1}). Looking at the electrochemical performance and behavior, the reversibility and cycling stability was excellent for the electrode, retaining ≈87% of the delithiation capacity after 100 cycles.

Binder jetting is another form of ink-based printing not as common as inkjet in energy applications. For example, Pope et al. fabricated thick graphene-based electrodes for supercapacitors demonstrating the capabilities and new avenues for energy storage, conversion, and sensing applications.[92] Figure 6g shows the general process for 3D printing GO anode electrode by first dispersing the powder in a capillary consolidation to have a homogenous distribution across the build bed. Then the binder-injected samples containing >90% water, 8% glycerol, and 2% other humectants were applied at 8-bit grayscale colormap distribution.[92] The ink was then 3D printed as a GO disk around 300 μm in thickness, which was then depowered, dried,

and impregnated with palladium (Pd) to improve the performance of the electrode. Compared to conventional mechanical pressing, the binder jetting showed a more porous microstructure leading to an interconnected pore structure that facilitated ion kinetics. The impregnation of Pd helped the contact resistance from powder agglomerates while improving the gravimetric conductivity by a factor of two and the areal capacitance by a factor of seven.[92] Furthermore, the supercapacitor showed a capacity retention of 80% >100 cycles, demonstrating potential of binder jet printable anodes for battery applications.

3.2. 3D-Printing Cathode Materials

3.2.1. Light-Based 3D Printing for Cathodes

Light-based 3D printing for cathode materials is very limited due to their complex composition, structure higher melting point, and brittleness than anode materials. However, Ning et al. focused on developing microbatteries via SLA 3D printing.[74] Combining lithography and conventional photolithography allowed for a fine tunability of the internal mesostructures. **Figure 7**a_1 shows the overall process for printing microbattery mesostructured hierarchies. The first step was the fabrication of the holographic lattice on the indium tin oxide (ITO) substrate and then filling the lattice with SU-8 (10 μm thick) before exposing it to four interfering laser beams arranged in an umbrella geometry for 0.5 s. After drying, the infiltration of positive photoresist AZ9260 was photopatterned using the SLA printer. Then the electroplating of Ni was done, followed by removing the polymer template, leaving an interdigitated 3D Ni structure before etching the free ITO. The final step was the electroplating of active materials, such as cathode (LMO) and anode (Ni–Sn), in an interdigitated pattern (Figure 7a_2). As a result, a high energy density of 6.5 μW cm^{-2} $μm^{-1}$ for the microbattery was achieved that possessed supercapacitor-like power at the peak of 3600 μW cm^{-2} $μm^{-1}$.[74] Figure 7a_3 plotted the voltage and current over time at different cycles. The results showed that the 10 μm thick electrode at 200 cycles had a 12% capacity fade for the lithium-ion microbattery. The internal structure of the design shows the relation between the width of the active materials and the gap (15 μm). The gap allows faster Li-ion kinetics to transfer back and forth, producing high power and energy typically seen in lithium-ion supercapacitors. Moreover, the capacity was measured against the electrode digit width at different C-rates from 1 to 1000.[74] The trend showed that the cell with the lowest tortuosity (largest porous) had the best power performance.

3.2.2. Filament-Based 3D Printing for Cathodes

Filament-based 3D printing has gotten a lot of attention for energy storage applications. Table 3 offers a detailed comparison between filament-based 3D printable cathodes. For example, Golodnitsky et al. made 3D printable microbatteries using the LTO as the anode and the cathode of the LFP conductive materials via FDM.[76] With the unique shape of having an interlaced electrode, it was hypothesized to alleviate the continuous volume changes during the charge and discharge cycles of the battery. However, it was found that only about 50% of the theoretical capacity was used for the LFP. Hence, further optimization of the active material, composition, morphology, compatibility, and printability is necessary to achieve a higher-performance battery. They also suggested looking into new hierarchies for a more continuous charge/discharge volumetric change while operating as a multimaterial system.[76] Wiley et al. also demonstrated a completely 3D-printed LIB via FDM.[77] However, they decided to use LMO as the main cathode material while adding PLA and MWNTs for improved printability and robustness. While their studies focused on finding the relationships between filler loading, conductivity, charge storage capacity, and printability. They found that the maximum load of conductive filler into the polymer must be less than 30% by volume to maintain acceptable printability.[77] This is reflected in lower performance when compared to the conventional LIBs using LTO and LMO. For future work, they suggested that wrapping the active materials with conductive filler before mixing them into the polymer chains could potentially improve the electrical contact when present at low concentrations in the polymer.[77] Hence, Maurel et al. not long after demonstrating a 3D printable anode in 2018 developed both cathode (LFP/PLA) and separator (SiO_2/PLA) materials to be printable via FDM, as shown in Figure 7b_1 b_3.[78,94] A max load of 52 wt% of active materials were used for the cathode while still maintaining printable parameters. A pool of thermal, electrical, and electrochemical analyses was done to arrive at an optimal filament for both the cathode and the separator. Hence, using their previous 3D-printed anode,[78] they were able to create a fully 3D-printed battery via the FDM method. With the freedom to tune the separator thickness, they could balance the cell to improve the performance of the LIBs illustrated in Figure 7b_4 for their specific capacity versus the cycle number at different C-rates.[94] Shortly after, Sun et al. FDM-printed a selenium(Se)-based cathode containing CNTs with mechanical blockage and dendritic penetration.[95] Note that the Se had a high load of 20 mg cm^{-2} that generated an areal capacity of 12.99 mA h cm^{-2} at a high current density of 3 mA cm^{-2}. This is the highest reported areal capacity for quasi-solid-state lithium–Se batteries.[95]

3D-printing electrodes were introduced by Lewis et al. via DIW for both LTO and LFP electrodes.[104] Then, Hu et al. 3D printed a complete battery using GO-based electrodes using LTO as the anode and LFP as the cathode.[81] Both cathode and anode contained GO in their matrix, but the LFP-GO cathode performed better than the LTO-GO anode due to the smaller NPs, which shortened the Li^+ transportation distance.[81] Another consideration was that the LTO-GO had lower electrical conductivity, making the capacity more susceptible to decay.[81] Another example is from Pan et al., who developed 3D printable $LiMn_{0.21}Fe_{0.79}PO_4$ (lithium-iron-manganese-phosphate (LMFP)) nanocrystal cathodes achieving one of the highest rate LMFP-battery capabilities (i.e., 150.21 and 140.67 mAh g^{-1} after 1000 cycles at 10C and 20C, respectively) and high reversible capacity performance.[97] The LMFP material is not the limiting factor for the battery; instead, it is a combination of electrolyte diffusion factors (i.e., efficient porosity, electrode thickness, and diffusion coefficient) that need to be optimized for higher rate performance. In 2020, Liang et al. 3D printed highly conductive thick electrodes via DIW using AgNWs, GO, and LTO as the cathode for a symmetrical cell configuration.[82] Figure 7c_1 shows the synthesis process in four

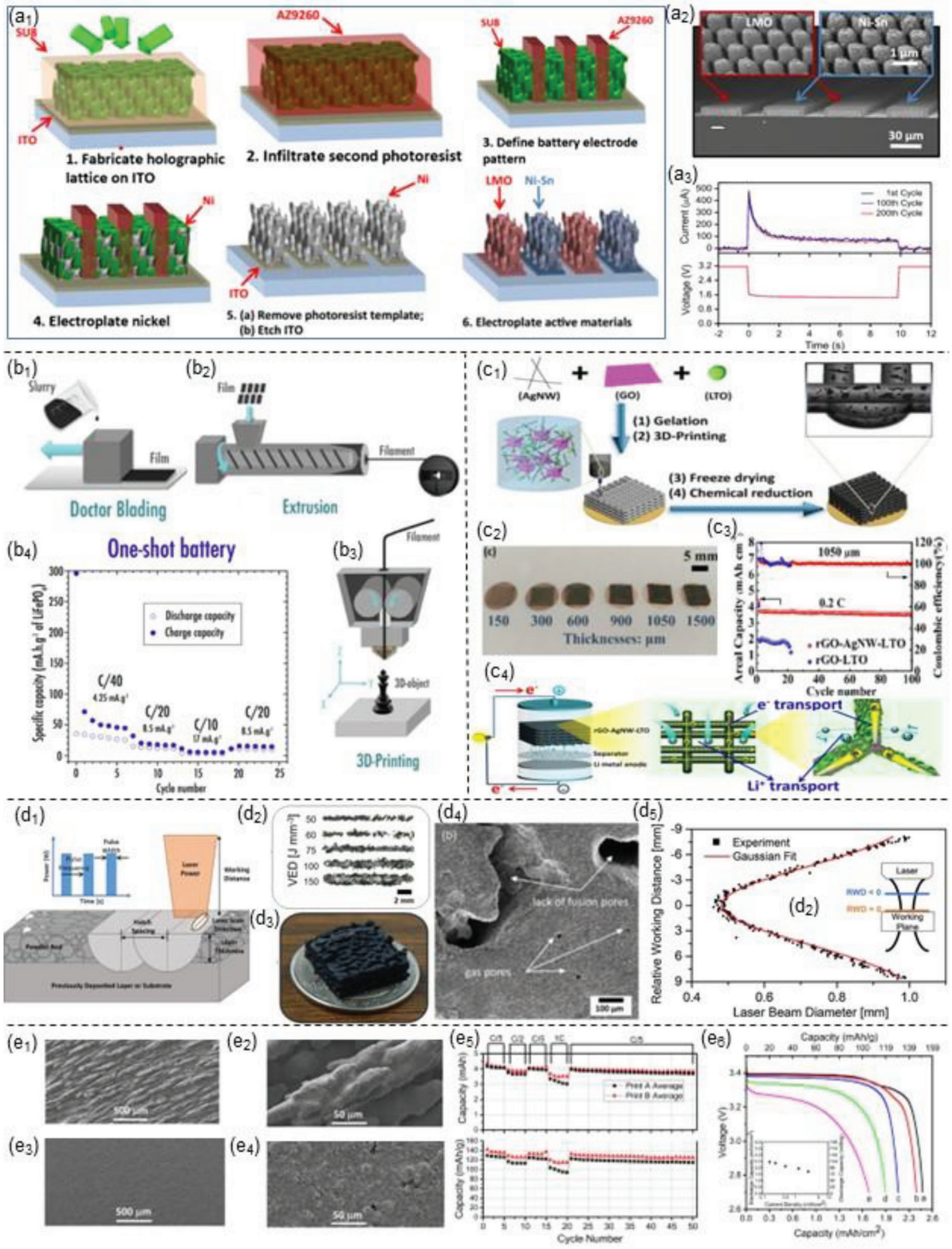

Figure 7. a_1) Representation of the 6 steps for microbattery production using SLA. a_2) Cross-sectional SEM image of the interdigitated electrode with the alternating lithium manganese oxide (LMO) cathode (red) and nickel–tin (Ni–Sn) (blue) anode. a_3) (*V*–*C*) versus time profile for the 1st, 100th, and 200th cycle. Reproduced with permission.[74] Copyright 2015, National Academy of Science. b) Filament production for lithium iron phosphate (LFP)/graphite (Gt) electrode: b_1) mixing components into a solvent to be spread out by doctor blading to create films. b_2) Films are introduced into an extruder and spooled into a filament. b_3) Filament is introduced into an FDM 3D printer. b_4) Capacity retention plot at different C-rates for a completely 3D printed battery with a Hilbert curved pattern separator at 70% infill and layer thickness of 50 µm and a second separator at 100% infill density and thickness

steps. The printable electrodes are then tested at different thicknesses ranging from 150 to 1500 µm as viewed in Figure 7c_2. The areal capacity versus the cycle life at the maximum thickness for the electrodes was tested with and without the AgNWs at 0.2C, as shown in Figure 7c_3. The results showed a capability of 121 mAh g^{-1} at 10C, a high areal capacity of up to 4.47 mAh cm^{-2}, and a capacity retention of ≈95.5% after 100 cycles.[82] LTO is a typical anode electrode, but in this configuration, it acted as the cathode electrode (Figure 7c_4).

Shortly after, Cui et al. fabricated a new LFP cathode using additives in pursuit of higher energy density and areal capacity.[96] The use of PEDOT: PSS nanofibers, carbon methyl cellulose (CMC), and super-P were successful to create printable (i.e., LFP-PEDOT-CMC) inks.[96] The cathode inks demonstrated high conductivity due to the interconnected network, providing high ionic kinetics throughout the charge and discharge cycles. Note that the LFP-PEDOT-CMC had a high-capacity retention of 92% after 100 cycles at 0.2C for a 1.43 mm thick electrode.[96] Any other electrode bigger than 1.43 mm significantly decreased the discharge capacity rate and cycle capability. As previously mentioned, the transport distance increases with the thickness which hinders the Li^+ and electrons transportation. Nonetheless, the work described above illustrated the potential for researchers to mitigate current challenges.

3.2.3. PBF-Based 3D Printing for Cathodes

Powder-based 3D printing can be useful for processing cathodes. As demonstrated by Schoenung et al., lithium nickel cobalt aluminum (NCA) oxide cathode could be 3D printed via SLS.[98] Figure 7d_1 illustrates the major components of SLS printing as well as the pulse width and frequency to further tune the printability (Figure 7d_2–d_5). However, finding the optimal laser beam diameter to print cathodes was their research objective. Figure 7d_5 shows the relative working distance in mm versus the laser beam diameter in mm distribution to experimentally determine the laser beam profile. For example, the laser scan speed and laser beam diameter could influence the morphology of the single tracks, as shown in Figure 7d_2. Therefore, the volumetric energy density was varied from 50 to 150 J mm^{-3} for the laser beam profile while keeping constant the laser beam diameters (0.85, 0.75, 0.65, 0.55, and 0.47 mm). It was found that discontinuous printing happened below 75 J mm^{-3} while continuous printing suffered from extensive cracking when the beam is below 0.65 mm in diameter.[98] Figure 7d_3,d_4 shows an example of the printed NCA cathode on a coin for reference while exposing the surface porosity (2–3 µm grains) and the internal porosity with gas pores and a lack of fusion pores within the SEM micrographs. Hence, this study focused on optimizing the printability parameters of the SLS with binder-free NCA with micron-sized grains and pores. Further characterization and cell assembly need to be done to determine the practicality and performance of battery applications. Nonetheless, it shows potential for processing advanced 3D-printed cathodes in LIBs.

3.2.4. Ink-Based 3D Printing for Cathodes

Inkjet printing has been primarily applied to text and graphic processing. However, Gu et al. studied the physical and chemical properties of LFP aqueous-based cathode fabricated via inkjet printing with different initial pH values.[100] To begin, the cathode powder was mixed with the conductive agent and binder as well as with different pH solutions (i.e., pH of 3, 5, 7, 9, and 10) to determine the ionic concentration based on the initial pH values versus the aging time relationships. Their results showed that the pH values of different samples reached identical final values of around 9.13 after 1 h, regardless of the initial pH value. For the pH to change, it must consume active materials (LFP) and introduce impurities. In other words, samples below 9.13 pH needed to consume protons to raise their pH value, while samples above 9.13 needed to consume hydroxide to lower their pH value. They also found that the particles of LFP decreased in size when initial pH values were below 9.13. On the other hand, the particle size increased with aging when the initial pH was above 9.13 with less amount of oxygen. Hence the electrochemical performance is still poor due to the impurities ($LiAlO_2$ and $AlPO_4$) between the Al current collector and active materials. However, there was a strong attraction between CNT and active materials confirmed via SEM. Ultra-thin film nano-MnO_2 cathode was also developed using an inkjet printer. For example, the morphology, voltammetry, and electrochemical impedance were studied by Jiang et al. As a result, the discharge capacity of the cathode film was found to be 270 mAh g^{-1} at the current density of 4.01 A g^{-1} (Table 3).[101] The ink synthesis was using nanosized MnO_2, PC, binder poly(vinylidene fluoride-co-hexafluoropropylene), and solvent tetrahydrofuran (THF).[101] One of the unique features of printing via inkjet was preventing agglomeration due to the challenges of maintaining homogenous suspensions/emulsions and achieving the same average size of particles from the commercial NPs. Hence, the average thickness of the printed electrode was 1.4 µm with a high discharge rate of 14.4C, showing the potential for micro-thin film batteries via inkjet printing.

of 100 µm referred to as "One-shot battery." Reproduced with permission.[94] Copyright 2019, Scientific Reports. c_1) Schematic illustration of the 3D printing process via DIW for the graphene oxide (GO)-AgNWs-LTO ink. c_2) Image of the 3D printed electrodes with different thicknesses (e.g., 150, 300, 600, 900, 1050, and 1500 µm) after lyophilization. c_3) Areal capacity and Coulombic efficiency for the GO-AgNWs-LTO and GO-LTO of 1050 µm thickness at 0.2C for 100 cycles. c_4) Illustration of the ion and electron transportation during the discharging process for the GO-AgNW-LTO electrode. Reproduced with permission.[82] Copyright 2020, Elsevier. d_1) SLS schematic with the pulse profile for the sintering process. d_2) Optical micrographs of single tracks as a function of volumetric energy density and laser beam diameter at 0.85, 0.75, 0.65, 0.55, and 0.47 mm. d_3,d_4) photograph and SEM micrograph revealing the surface porosity as well as the internal porosity showing lack of fusion pores and gas pores in the cross-sectional area of the sample. d_5) Laser beam profile as a function of relative working distance and laser beam diameter. Reproduced with permission.[98] Copyright 2021, Elsevier. e_1,e_2) SEM microscopy image of LFP cathode fabricated via tape casting in comparison with e_3,e_4) aerosol jet printing. e_5) Average discharge capacities versus cycle number for "Print A" (average discharge capacity for two battery samples) and "Print B" (average discharge capacity for three battery samples). e_6) Voltage versus discharge capacity for aerosol jet printed LFP cathode at a) C/15, b) C/10, c) C/5, d) C/2, and e) 1C. Reproduced with permission.[103] Copyright 2019, Wiley-VCH.

Aerosol jet printing of cathode electrodes for LIBs focuses on conductive ink being deposited onto a substrate through an aerosol stream. For example, Deiner et al. showed the printability of cathode-based electrodes manufactured via aerosol jet printing.[103] What they found when looking at the microstructures were aligned needles that are several hundred microns long and ≈50 µm wide, as shown in Figure 7e_1,e_2. Whereas Figures 7e_3,e_4 are the microscopy images of the tape casting using a conventional LFP cathode. Interestingly, aerosol jet printed cathode had more than three times porosity in the range of 1.7 nm to 300 nm than the conventional tape casting method.[103] Figure 7e_5 shows the average discharge capacities which are stable during the 50 cycles of charge/discharge from varying C-rates of C/5, C/2 to 1C. Additionally, the batteries showed promising capacity retention of 93% for the first five cycles. Figure 7e_6 illustrates the voltage versus the discharge capacity for the aerosol jet printer. It was found that the discharge capacity is 151 mAh g^{-1} at 0.32 mA for the C/15 rate. When the C-rate increased to C/10, the specific capacity decreases to 145 mAh g^{-1}, which can be seen as the trend that increasing the C-rate would cause a decrease in the specific discharge capacity.[103] Yet, the overall performance suggests that aerosol jet is a promising technique for the fabrication of high capacity and rate capability in ESS applications.

4. 3D-Printing Electrolytes

LIBs have demonstrated enormous potential as a primary energy storage technology in various applications, including EVs, portable electronics, and grid energy storage systems. However, the liquid electrolytes used in LIBs can pose significant safety concerns due to their potential to leak, leading to fires and distortions in the battery's internal structure during swelling. Consequently, researchers have focused on developing SSEs as a promising alternative to liquid electrolytes, offering improved safety, performance, and durability. SSEs can function as a separator in the battery, making it less flammable, non-volatile, non-corrosive, and thermally stable (**Table 4**). In recent years, 3D-printing technology has emerged as a promising approach to producing customized SSEs with precise microstructure and nanostructure designs (Table 4). This approach allows for creating complex geometries, improving the battery's performance, and reducing its weight. 3D printing also enables the production of SSEs with controlled porosity, which can enhance their electrochemical performance. 3D printable SSEs include the following categories.

- Oxide solid electrolytes (OSEs) typically comprise lithium-containing oxides, which provide high ionic conductivity and electrochemical stability. Researchers have developed various printing methods for OSEs, including light- and extrusion-based printing. These methods allow for the precise deposition of OSE ink onto a substrate, creating customized SSEs with desired properties.
- Solid polymer electrolytes (SPEs) are another type of SSE that has received considerable attention in 3D printing research. SPEs offer several advantages, including high flexibility, good adhesion, and excellent mechanical properties. Extrusion-based printing for SPEs is the most common, allowing for complex geometries with high-resolution control.
- Composite solid electrolytes (CSEs), which combine the advantages of OSEs and SPEs, have also been developed using 3D-printing technology. CSEs offer improved electrochemical properties and mechanical strength compared to single-component SSEs. In addition, researchers have developed various CSEs via AM, including nanocomposites, microfibers, and microspheres.

4.1. 3D Printing Strategies for Oxide Solid Electrolytes (OSEs)

SSEs have attracted considerable attention in energy storage due to their high energy density, longer lifetime, and improved safety characteristics compared to conventional liquid electrolytes.[2,17,29] In addition, among various types of SSEs, OSEs have shown great potential due to their high ionic conductivity, thermal stability, and compatibility with different electrode materials.[106] As a result, OSEs have been extensively researched for their potential applications in solid-state batteries, fuel cells, and other electrochemical devices. To further enhance the production and performance of OSEs, researchers have explored various strategies, including 3D printing mechanisms. 3D printing is a promising OSE processing technique for fabricating complex structures with high precision, reproducibility, and flexibility. Different 3D printing techniques have been explored to produce OSEs, including inkjet printing, extrusion-based printing, SLA, and laser-based techniques. However, the current AM of OSEs is still limited to only a few printing techniques, which restricts the diversity and complexity of structures that can be fabricated. Moreover, researchers have only explored a limited number of OSE materials, such as lithium lanthanum zirconium oxide (LLZO), lithium aluminum titanium phosphate (LATP), and lithium garnet oxide (LGO), to fabricate high-performance OSEs.[122] LLZO, for example, has demonstrated high ionic conductivity and stability against moisture and air, making it an attractive candidate for use in solid-state batteries. LATP has shown high ionic conductivity and excellent chemical stability, making it suitable for high-temperature applications. LGO has also demonstrated high ionic conductivity and stability, making it a promising candidate for use in fuel cells.

Ceramic lithium-ion conductors have drawn much attention for their potential in next-generation batteries. However, their brittle nature and high resistance at grain boundaries have posed challenges to their practical application. Furthermore, conventional manufacturing techniques cannot achieve the required thin microstructures, limiting their effectiveness. In response to these challenges,[122] Bruce et al. proposed a 3D printing method via SLA to create microarchitectures using sacrificial materials (**Figure 8**a_1–a_4).[105] Specifically, templates such as cubes, gyroids, diamonds, and bijel-derived structures were produced, as shown in Figure 8a_5–a_8.[105] The use of light-based 3D printing enabled the creation of finer structures (Figure 8a_9–a_{12}) through the use of light instead of physical nozzles. Therefore, after the template was 3D printed, the ceramic lithium-ion conductor ($Li_{1.4}Al_{0.4}Ge_{1.6}(PO_4)_3$ (LAGP)) was filled and then calcinated/sintered to extract the sacrificial material while filled with non-conductive polypropylene (PP) or epoxy polymer (Figure 8a_1–a_4).[105] To check the electrochemical characteristics, the change in resistance (R: total resistance, R1:

Table 4. Summary and comparison of the materials, manufacturing techniques, and performance of 3D printed electrolytes for LIBs. See terminology below and also in Section 6 (ADP, ammonium dihydrogen phosphate; ANN, aluminum nitrate nanohydrate; BAPO, phenylbis(2,4,6-trimethyl-benzoyl)phosphine oxide; BBP, benzyl butyl phthalate; BMITFSI, 1-butyl-3-methylimidazolium bis(trifluoromethyl sulfonyl)imide; CSE, composite-solid electrolyte; EMI-TFSI, 1-ethyl-3-methyl imidazolium bis(trifluoromethanesulfonyl)imide; ESL 441, proprietary texanol-based composition; ETPTA, ethoxylated trimethylolpropane triacrylate; IBoA, isobornyl acrylate; JA-UPy, jeffamine with quadruple-hydrogen bonds; LCO, lithium cobalt oxide; LiDFOB, lithium difluoro(oxalato)borat; LiNO3, Lihtium nitrate; LiTFSI, Lithium bis(trifluoromethanesulfonyl)imide; LiTriflate, lithium trifluoromethanesulfonate; LLZO, $Li_7La_3Zr_2O_{12}$; MEG, ethylene glycol; NMC, lithium nickel-manganese-cobalt oxide; OSE, oxide-solid electrolyte; PDMS, polydimethylsiloxane; PEGDMA, poly(ethylene glycol) dimethylether; PEG-UPy, polyethylene glycol with quadruple-hydrogen bonds; PEO, polyethylene oxide; PEO-CTA, poly(ethylene oxide) macro-chain-transfer agent (macro-CTA); POEGMEA, poly(oligoethylene glycol methyl ether acrylate); PVB, polyvinyl butyral; SPE, solid-polymer electrolyte; TMOS, tetramethyl orthosilicate; TMPTA, trimethyl propane triacrylate; TPO, diphenyl(2,4,6-trimethylbenzoyl) phosphine oxide).

Electrolytes	Manufacturing features				Materials		Properties			Refs.
	Method	Features [μm perlayer]	Speed [mm s^{-1}]	Layer number	Particles	Additives	Cell assembly	Capacity	Electrical conductivity [mS cm^{-1}]	
OSE	SLA	67	–	≈18	LAGP	MEG, LiNO3, ANN, ADP	Symmetric cell (LiM|OSE|LiM)	0.5 (mAh cm^{-2})	0.16	[105]
	DIW	12.5, 25, 125	0–500	1–2	LLZO	PVB,BBP, ESL 441	Symmetric cell (LiM|OSE|LiM)	–	0.05	[106]
SPE	SLA	0.05	0.01	100	$LiClO_4$	BAPO, Sudan I, PEGDMA	Full-cell (LFP|SPE|LTO)	0.0014 (mAh g^{-1}) @1.5–4.2 V	4.8 @25 °C	[107]
	SLA	100	–	1–2	LiTFSI	BAPO, PEGDMA	Half-cell (LiM|SPE|LFP)	166 (mAh g^{-1}) @ 0.1C	0.37 @25 °C	[108]
	DLP	50	3	7,11,15	BMITFSI	PEO-CTA, IBoA, TMPTA	Symmetric cell (carbon/PVDF|SPE|carbon/PVDF)	–	0.3 @22 °C	[109]
	DLP	11	15 s/layer	≈5	BMITFSI	POEGMEA, IBoA, TMPTA, TPO	N/A	–	1.2 @ 30 °C	[110]
	FDM	1750	0–150	≈2	LiTFSI	PEO	N/A	–	2.18 @90°C	[111]
	FDM	1400–1700	–	≈1	LiTFSI-Pyr_{14}TFSI	PLA-PEO	Symmetric cell (LiM|SPE|LiM)	–	0.2 @60 °C	[112]
	FDM	330	10	4	LiTFSI	JA-UPy PEG-UPy	N/A	–	10^{-7}–10^{-9} @80 °C	[113]
	DIW	200	–	1	LiTFSI	ETPTA, PDMS, $LiPF_6$	Full-cell (NMC111/SPE/LTO)	>120 mAh g^{-1}	–	[114]
	InkJet	800	–	–	Pyr_{13}.Li-TFSI	TMOS	Full-cell (LFP/SPE/LTO)	300 μAh cm^{-2}	–	[115]
CSE	DIW	100	5	6,12,18	PVDF-co-HFP	Al_2O_3	Full-cell (LFP/CPE/LTO)	150	–	[81]
	DIW	200	2	5	EMI-TFSI	SiO_2	Half-cell (LCO/CSE/LiM)	100 (mAh g^{-1}) @ 0.1 C	2.9 @25 °C	[116]
	DIW	250–840	5–20	1–2	PVDF	Al_2O_3	Half-cell (LFP/CSE/LiM)	154 ±2 (mAh g^{-1}) @0.2 C 101 ±5 (mAh g^{-1}) @5.0 C	0.82	[117]
	DIW	150	5	1	PVDF-co-HFP	TiO_2	Full-cell (LTO/CSE/LFP)	148 (mAh g^{-1}) @ 16 mA g^{-1}	0.78	[118]
	FDM	330	–	6	LITFSI, PEG-UPy	SiO_2	N/A	–	0.032	[119]
	FDM	200	–	1	LiTFSI	Al_2O_3/SiO_2, PLA, PEO	Full-cell (LTO/CSE/LFP)	–	0.03 @ 120°C	[120]
	Aerosol	10–50	–	60,35, 25	LiDFOB	Al_2O_3, PEO	Half-cell (LFO/CSE/LiM)	162 mAh g^{-1}	0.5 @ 55 °C	[121]
	Aerosol	200–300	–	≈240	LiTriflate	Al_2O_3, PEO	Half-cell (LFO/CSE/LiM)	41 mAh g^{-1}	0.7 @ 85 °C	[121]

NANO · MICRO small
www.small-journal.com

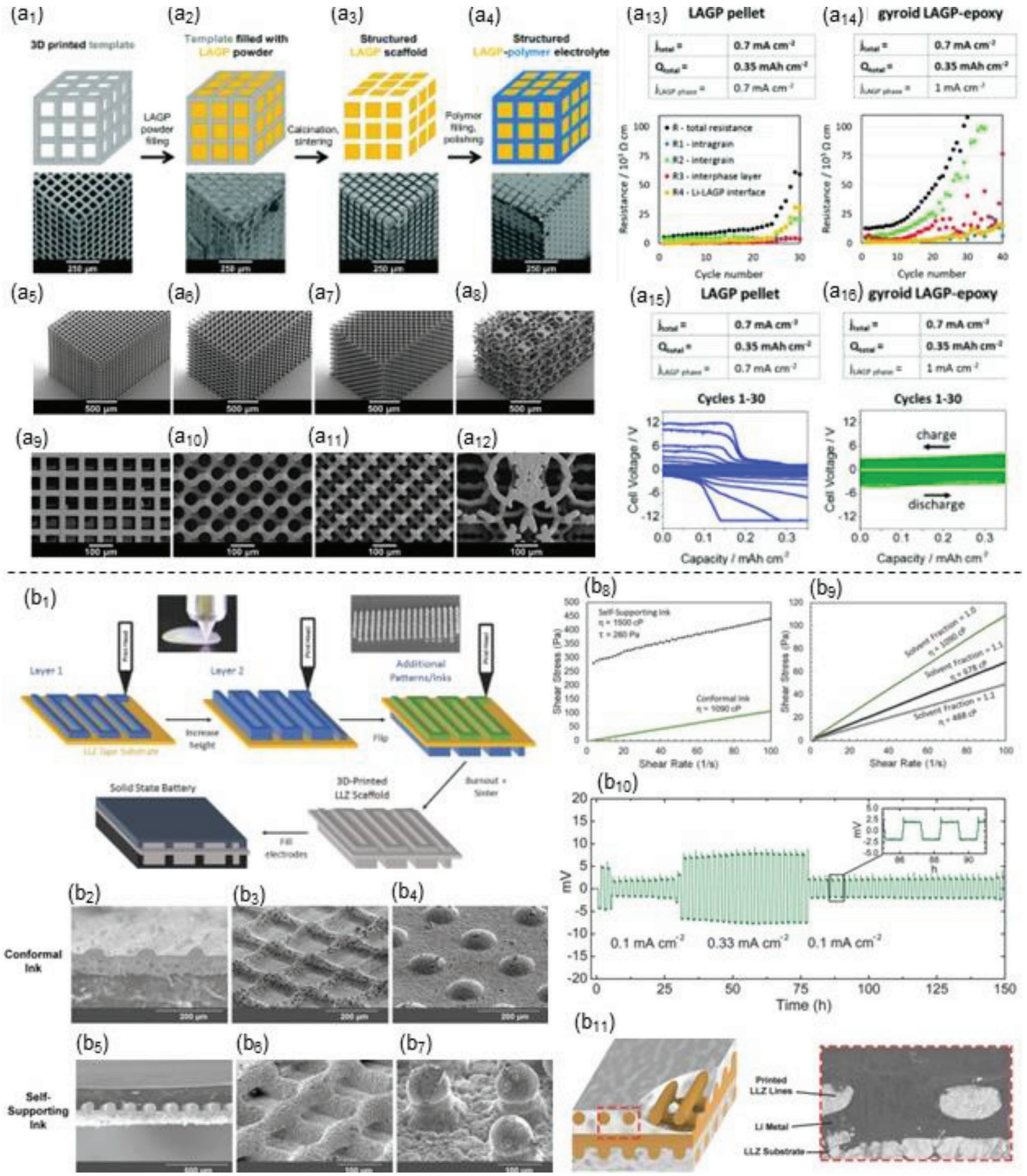

Figure 8. a_1–a_4) SLA illustration of the $Li_{1.5}$ $Al_{0.5}Ge_{1.}5P3O12$ (LAGP)–polymer electrolyte, including SEM of the 3D printed templates for a_5) cube, a_6) gyroid, a_7) diamond, and a_8) bijel-derived with a_9–a_{12}) the zoomed-in SEM for each template at a scale of 100 µm. Resistance versus cycle number for a_{13}) LAGP-pellet and a_{14}) gyroid-LAGP-epoxy as well as the cell voltage versus cell capacity for a_{15}) LAGP pellet and a_{16}) Gyroid-LAGP-epoxy. Reproduced with permission.[105] Copyright 2018, Royal Society of Chemistry. b_1) 3D printed LLZO schematic via DIW on an LLZO tape substrate, with SEM for the conformal ink configuration for b_2) lines, b_3) grids, and b_4) column patterns. b_5–b_7) Respective patterns with the self-supporting ink behavior. Rheology characterization for the shear stress versus shear rate for the b_8) self-supporting inks and conformal inks, and the b_9) solvent fraction to control the ink viscosity. b_{10}) DC cycling profile for the symmetric cell at varying current densities. b_{11}) Schematic grid structure used in the symmetric cell with the Li metal filling the 3D printed LLZO pores. Reproduced with permission.[106] Copyright 2018, Wiley-VCH.

intragrain, R2: intergrain, R3: interphase layer, R4: Li-LaGP interface) was measured concerning the cycle number for the LAGP-pellet and gyroid LAGP-epoxy as shown in Figure 8a_{13},a_{14}, respectively. It was found that the structured pellet had an increase in interface resistance from the 10th cycle onwards.[105] In addition, Figure 8a_{15},a_{16} illustrates the galvanostatic cycling for LAGP pellet and gyroid structure at a voltage range of 12 V and capacity range of 0.3 mAh cm^{-2}. The gyroid LAGP-epoxy performs better at retaining a gradual increase in voltage polarization while the pellet electrolyte increases rapidly during the 30 cycles.[105] The study shows the potential of printing OSEs while maintaining good ionic conductivity and improving mechanical properties.[105]

As another example, Wachsman et al. investigated the feasibility of 3D printing OSE based on ceramics. Specifically, they studied the printing of LLZO solid electrolytes using the DIW method.[106] Figure 8b_1 illustrates the general printing of multiple layers on an LLZO tape substrate to be sintered and create a 3D LLZO scaffold ready to impregnate electrodes. This study reported two types of printable inks for different structural purposes. By tuning the printable inks with binders and plasticizers, a "conformal ink" shown in (Figure 8b_2–b_4) and "self-supporting ink" (Figure 8b_5–b_7) demonstrated the capability to print lines, grids, and columns for both configurations. The tunability of inks can be viewed through the rheology characterization of the solvent fraction as shear stress versus shear rate concerning the overall self-supporting ink and conformal ink (Figure 8b_8,b_9). It is worth noting that an atomic layer deposition (ALD) was applied on electrolytes to facilitate the wettability of the lithium metal (LiM) to the LLZO scaffold.[106] The results showed a low area-specific resistance (ASR) of 20 Ω cm^{-2} during cycling, demonstrating the high and stable conductivity in Figure 8b_{10} of the 3D-printed LLZO electrolyte. The data presented in Figure 8b_{11} suggests that the connections between the 3D-printed LLZO layers and the Li metal were continuous without any noticeable defects. However, additional investigations are required to optimize and carefully examine the impedance of the cell, mechanical robustness, and the 3D architectures of the printed components.

4.2. 3D Printing Strategies for Solid Polymer Electrolytes (SPEs)

Light-based printing is more common for SPEs and most notable for being transparent or stretchable, depending on their material properties. For example, Chen et al. successfully 3D printed an SPE for a lithium-ion micro battery via SLA.[107] The electrolyte was printed in a zig-zag pattern using UV-cured polyethylene glycol (PEG)-based polymer and sandwiched between the LFP and LTO active materials. The zig-zag print was carefully considered further to increase the contact between the electrodes and electrolytes and decrease internal resistance. Another example can be seen in **Figure 9**a_1, where Liu et al. 3D printed SPEs using PEO and lithium salts via SLA with an Archimedean spiral structure to shorten the Li-ion transport pathway between the electrode and electrolyte.[108] Figure 9a_2–a_3 demonstrates the spiral structure with interdigitated patterns (Archimedean spiral structure) to increase the contact area between the electrode and electrolyte and decrease internal resistance.[108] Figure 9a_4,a_5 shows the cross-sectional SEM images of the 3D-printed SPE with the interface between the electrolyte and electrode, while Figure 9a_6 shows the electrolyte flexibility and transparency. Hence, the performance shows a higher specific capacity of 166 mAh g^{-1} with an improved capacity retention of 77% after 250 cycles at 50 °C than structure-free SPEs.[108]

Using a different AM method, such as DLP, to print SPE was demonstrated by Boyer et al., who developed a reversible addition–fragmentation chain transfer (RAFT)-based polymerization-induced microphase separation (PIMS) system to fabricate SPE with tunable nanoscale morphological features, as shown in Figure 9b_1,b_2.[109] Using 1-Butyl-3-methylimidazolium bis(trifluoromethylsulfonyl)imide (BMITFSI) as the liquid electrolyte and varying the load between 40, 50, and 60 wt% did not affect the inhibition period or the overall reaction rate.[109] Figure 9b_3 shows the storage modulus in relation to temperature for the current SPE compositions. Also, it was found that varying the BMITFSI content or poly(ethylene oxide) macrochain-transfer agent (macro-CTA) (PEO-CTA) slightly reduced the shear modulus. Still, the mechanical properties of the SPEs in response to the temperature had no notable change. Schematic of the symmetric carbon cell assembly in Figure 9b_2–b_4 displays the high Columbic efficiency and excellent long-term cycling behavior from 100 to 3000 cycles. In addition, EMITFSI and $EMIBF_4$ were tested to substitute the BMITFSI liquid electrolyte. However, PEO-CTA was not soluble in $EMIBF_4$, and instead, the EMITFSI gave excellent printable SPE with robust mechanical strength and ionic conductivity (G' = 180 MPa, $\sigma = 9.0 \times 10^{-5}$ S cm^{-1}).[109] This work shows the printable SPE with enhanced mechanical and conductive properties.

FDM is another AM technique that has shown the ability to 3D print SPE. For example, Binder et al. studied the effects of three different telechelic polymer quadruple-hydrogen bonds (UPy) to tune the printability of CSE used in LIBs, as shown in Figure 9c_1.[123] It was found that the JA-900-UPy was most suited for easy self-healing showing amorphous elastic and transparent properties, illustrated by the optical images in Figure 9c_2,c_3. Compositions with too little salt concentrations were found to be too crystalline and unsuitable for testing during the rheology characterization. Figure 9c_4 shows that the PEG-1500-UPy with a molar EO/Li ratio of 10:1 and 5:1 was too sticky and viscous. Thus, using specific ratios from EO/Li 20:1, 10:1, to 5:1, the rheological profile can be tuned for printable filaments. Figure 9c_5 shows the ionic conductivity profile concerning frequency at temperatures of 0, 25, and 80 °C for the JA-900-UPy-12 set, demonstrating that lithium ions weakened the UPy-bonds and reduced the crystallinity of the polyethylene oxide (PEO) units.[123] Therefore aside from the melt-rheology, lithium salt, and polymer crystallinity, it adds an additional toolbox to tune the printability of electrolytes via FDM. Note that more examples of filament-based printing can be found in Table 4.

Displaying the capabilities of 3D printing SPE via the DIW method is another avenue that offers a greater range of materials to be produced. For example, Chung et al. fabricate a complete LIB via DIW (Figure 9d_1) by tuning the rheology inks for the LTO and LFP cathodes, silver (Ag) and carbon current collector, UV-cured SPEs and polydimethylsiloxane (PDMS) for packing the battery.[114] Figure 9d_2,d_3 shows microbattery arrays (4×3) in 10 mm by 10 mm and the structure of a single LIB in

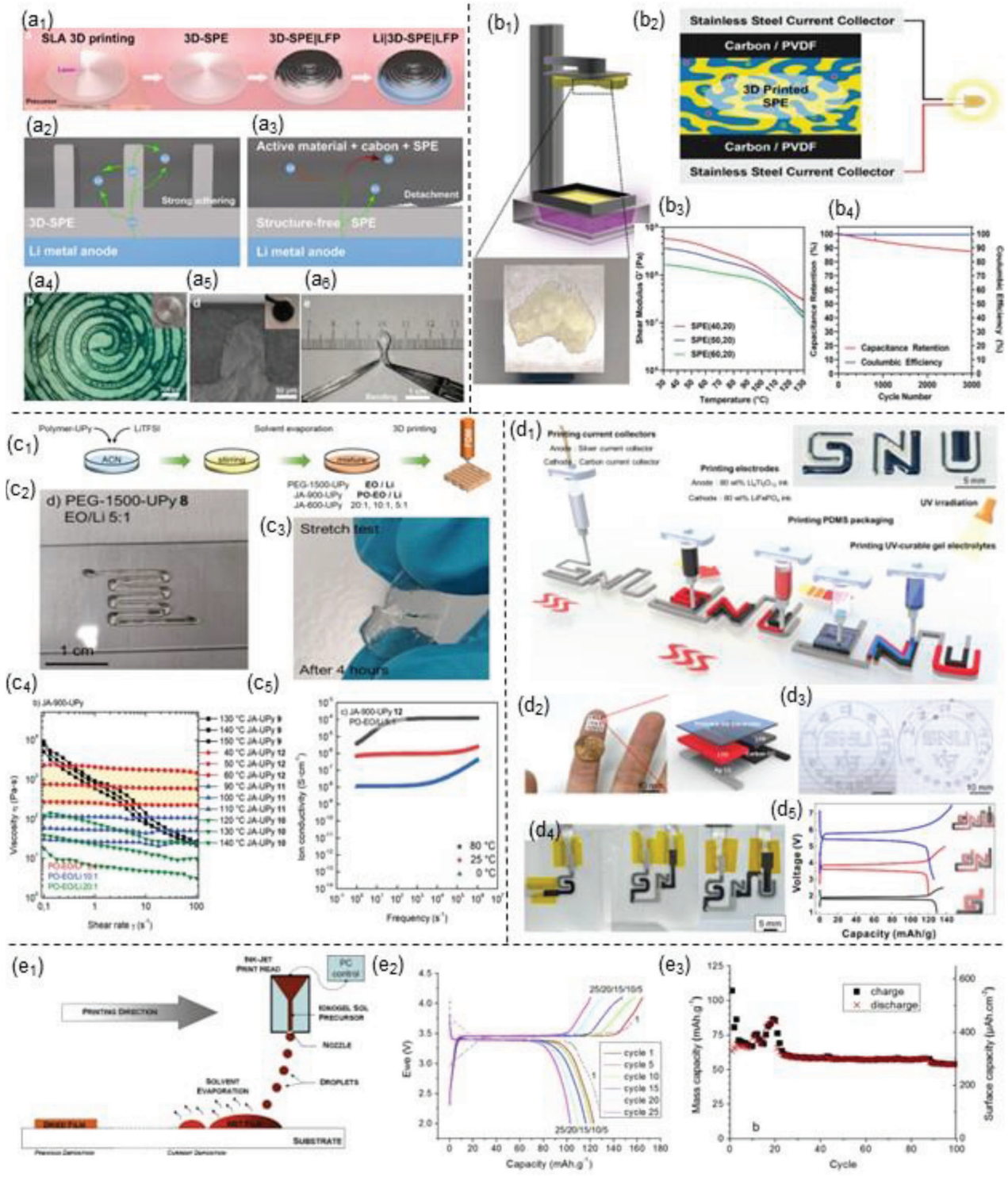

Figure 9. a_1) Illustration of the manufacturing process via SLA for the solid-polymer electrolyte (SPE) and cell assembly. Schematic representation between the a_2) interdigitated structure with improved interface adhesion versus the a_3) conventional contact interface with weak adhesion prone to have low conductivity. a_4) Optical image of the top view for the spiral-interdigitated SPE and a_5) SEM cross-sectional view of the interface between the electrolyte and cathode material. a_6) Flexibility and transparency of the 3D printed SPE. Scale bars are 300 mm, 50 µm, and 1 cm for a_4–a_6. Reproduced with permission.[108] Copyright 2020, American Chemical Society. b_1) DLP 3D printed of the SPE with high modulus, conductivity, and transparency. b_2) Symbolic representation of the symmetric cell assembly using carbon/polyvinylidene fluoride (PVDF) as electrodes and stainless steel as current collectors on two sides of the 3D printed SPEs. b_3) Shear modulus with respect to temperature for the SPE at varying 1-butyl-3-methylimidazolium bis(trifluoromethylsulfonyl)imide (BMITFSI) concentrations of 40, 50, and 60 wt% while keeping a constant 2 wt% diphenyl(2,4,6-trimethylbenzoyl)phosphine oxide (TPO) concentration. (b_4) Ionic conductivity and shear modulus at ambient temperature with different BMITSI con-

addition to a side-by-side comparison of printed letters with conventional SPE (right) and the 3D printed GPE (left). As a demonstration of the charge and discharge cycles at different mass loadings (Black: 6.67 mg cm^{-2}, Red: 9.83 mg cm^{-2}, Blue: 10.9 mg cm^{-2}), Figure $9d_4$,d_5 shows that the increase in mass loading had small polarization changes.

Furthermore, inkjet printing was demonstrated by Bideau et al., who worked on silica-based electrolytes using ionogels' sol precursors and solvent evaporation, as shown in Figure $9e_1$. To determine the feasibility of the 3D printed SPE, Figure $9e_2$ shows the galvanostatic cycling on a half-cell composed of tape-casting LFP cathode, 3D printed SPE, and the LiM as the counter electrode at a C/30 rate in ambient temperature with voltage profile from 2.0 to 4.0 V.[124] The half-cell test showed low polarization due to the difference between the oxidation and reduction potential, which is around 100 mV. Furthermore, using an LFP cathode and LTO anode for a full-cell assembly was done to study the mass capacity and surface capacity with the charge and discharge cycles shown in Figure $9e_3$ at a C/10 rate in ambient temperature. This study showed a surface capacity of 300 μAh cm^{-2} up to 100 cycles, which is competitive compared to microbatteries based on conventional manufacturing, such as PVD.[124]

4.3. 3D Printing Strategies for Composite Solid Electrolytes (CSEs)

The CSEs are widely recognized for their ceramic filler, primarily Al_2O_3 and SiO_2. For the AM of FDM, Golodnitsky et al. 3D printed PLA:PEO:LiTFSI with ceramic fillers to compare SiO_2 and Al_2O_3. **Figure 10**a_1,a_2 shows the extrusion mechanism with different coils, springs, and similar shapes. While proposing a new co-axial printing method via FDM, the focus of the paper is characterizing the CSE with different ceramic fillers. Figure $10a_3$ shows the 3D-printed semitransparent CSE with a diameter of 19 mm and thickness of 200 μm.[120] First, the optical SEM images were taken of PLA:PEO:LiTFSI: SiO_2 (59:20:20:1%) and of PLA:PEO:LiTFSI: Al_2O_3 (59:20:20:1%) (Figure $10a_4$,a_5), respectively, to determine the thickness of the electrolytes. The silica-based electrolyte was around 210 to 220 μm while the aluminum-based was around 102 to 108 μm. The ionic conductivity measurements compared with conventional cast neat PEO-based electrolytes showed a lower conductivity value for printed electrolytes possibly due to the incomplete mixture of polymers/ceramic fillers.[120] Hence further optimization is needed for the FDM print on CSE.

DIW has shown versatility in printing SPEs and CSEs. For example, Durstock et al. focused on establishing an approach to 3D print electrolytes with controlled porosity via DIW (Figure $10b_1$) using a dry phase inversion (PI) method and comparing the structure and performance (Figure $10b_2$,b_3) with and without CSEs (Figure $10b_4$–b_7).[117] With acceptable durability and processability (Figure $10b_8$,b_9), Al_2O_3 as nanosized fillers with the PI method-processed CSE (Figure $10b_{10}$–b_{12}) enabled uniform sub-micrometer pore formation with nanofillers impregnated in the pores. Note that the rheology characterization in Figure $10b_9$ indicates that the CPE has a higher shear thinning behavior than other electrolyte compositions. However, adding ceramic fillers in the PI method allowed high flexibility of the electrolyte (Figure $10b_8$). The results in this study gave a high current rate of 5C with improved thermal stability and better wetting characteristics between the electrolyte and electrode (Figure $10b_2$,b_3) for the cross-sectional SEM images and the specific capacity versus cycle number at different C-rates. Not to mention that the PI method was also applied to the electrode inks, improving the electrochemical properties and better flexibility, which is beneficial to non-planar device surfaces by using AM.[117]

Another example from Hu et al. showed the 3D printing for a complete GO-based battery via DIW.[81] During the primary focus and novelty rest on 3D printing GO-based electrodes, they have also 3D-printed their CSE using poly(vinylidene fluoride)-co-hexafluoropropylene (PVDF-co-HFP) as their polymer electrolyte while adding Al_2O_3 as their ceramic nanofillers. The 3D-printed CSE functioned as an electrically insulated separator. However, $LiPF_6$ as a common liquid electrolyte and the 3D-printed CSE were injected into the cell to achieve a higher and more stable ionic conductivity. The full 3D-printed cell exhibited initial charge and discharge capacities of 117 and 91 mAh g^{-1} with good cycling stability.[81] While no data was reported on ionic conductivity, the capability of 3D printing a complete battery using interdigitated structures was displayed to demonstrate the versatility of AM. Note that PVD has been found to have good compatibility with LiTFSI, which is a lithium salt. The compatibility is due to the fact that PVDF has been observed to improve the movement of charged particles (ions) through the material. This is why LiTFSI is often included in battery formulation, as indicated in Table 4.

Aerosol jet printing further expands the AM methods for CSEs for the solid-state EES. For instance, Deiner et al. printed two distinct types of CSE using lithium difluoro(oxalate)borate (LiDFOB) and lithium trifluoromethanesulfonate (LiTriflate) as the main electrolytes. Each electrolyte was mixed with PEO and ceramic filler (Al_2O_3). Figure $10c_1$,c_2 shows the SEM cross-sectional area of the PEO/LiDFOB/Al_2O_3 and PLA:PEO:LiTFSI:

centrations. Reproduced with permission.[109] Copyright 2022, Wiley-VCH. c_1) Electrolyte mixture of telechelic, polyethylene glycol (PEG-1500-UPy), and bivalent (2-ureido-4-pyrimidinone) Jeffamine (JA-x00-UPy) with lithium bistrifluoromethane sulfonamide (LiTFSI) for 3D printable SEP via FDM. c_2) Illustrates the transparent 3D printed JA-900-Upy for a grid-like SPE structure as well as the c_3) stretchability after 4 h. c_4) Rheology characterization of the JA-900-UPy concerning viscosity as a function of the shear rate at varying temperatures to determine printing profiles of 200 to 2000 Pa s. c_5) Ionic conductivity profile with respect to the frequency at temperatures of 0, 25, and 80 °C for the JA-900-UPy 12 set. Reproduced with permission.[123] Copyright 2022, Wiley-VCH. d_1) Schematic illustration for a complete battery manufacturing process via DIW. d_2) Example of a 3D printed microbattery on fingertip with letters as d_3) Seoul National University (SNU) at the Korean Institute of Science and Technology (KIST). d_4) S, N, U battery assembly and the d_5) voltage of the complex cells in series at a C-rate of 0.2C. Reproduced with permission.[114] Copyright 2023, Elsevier. e_1) Inkjet printing representation for the SPEs. e_2) Mass capacity versus cycling at C/10 rate and room temperature of a full cell composed of LFP cathode and LTO as the anode electrodes. e_3) Galvanostatic cycling of half-cell with LFP/SPE/LiM from 2.0 to 4.1 V at C/30 rate and room temperature showing the mass capacity as a function of the cycle. Reproduced with permission.[124] Copyright 2015, Elsevier.

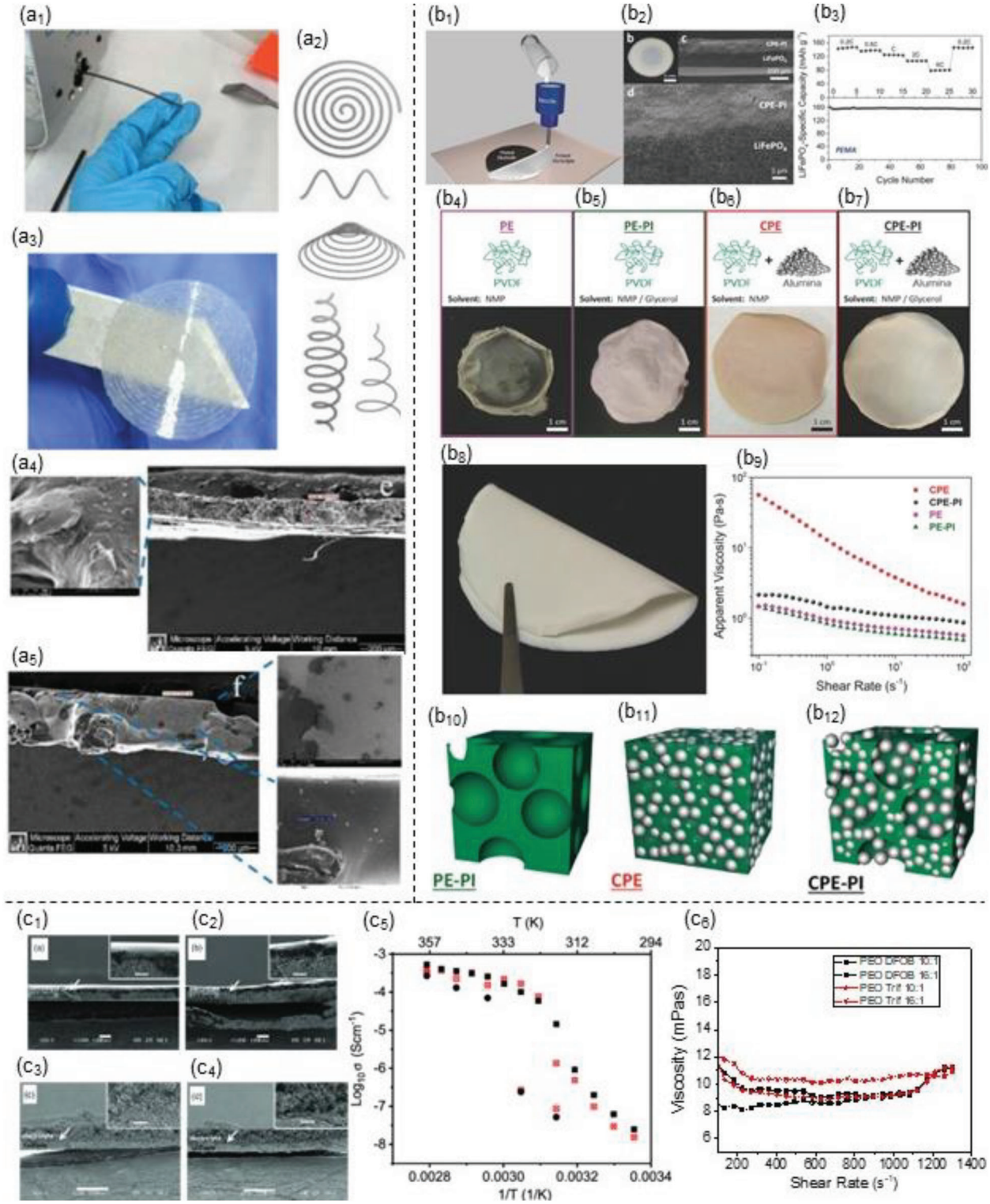

Figure 10. a_1) Optical image of FDM 3D printing using a filament-based extrusion with different a_2) schematic designs. a_3) Example of the transparent 3D printed spiral disk composite solid electrolyte containing polylactic acid (PLA): polyethylene oxide (PEO):LiTFSI and ceramic fillers, such as SiO_2 or Al_2O_3, at the following concentrations (50:20:20:1% w/w). a_4) SEM cross-sectional images of PLA:PEO:LiTFSI: SiO_2 (59:20:20:1%) electrolyte and a_5) PLA:PEO:LiTFSI: Al_2O_3 (59:20:20:1%) electrolyte. Reproduced with permission.[120] Copyright 2020, The Electrochemical Society. b_1) Schematic representation of the electrolyte printed directly on top of the electrode via DIW. b_2) SEM images of the composite-solid electrolyte (CSE) interface with the LFP cathode from the b_3) rate performance (top image) and cycling performance (bottom image) at 0.2C. b_4–b_7) Schematic and photos of the printed electrolyte composition and corresponding dried films. b_8) Flexible CPE-phase inversion (PI) membrane at a 6 cm diameter disk. b_9) Rheology studies

Al_2O_3, where the interface between the electrolyte and cathode (LFP) could be compared (Figure 10c_3,c_4). More interestingly, the PEO/LiDFOB/Al_2O_3 (EO:Li = 10:1) had better conductivity than the LiTFSI-based electrolyte at $>1 \times 10^{-5}$ S cm^{-1} at 45 °C (Figure 10c_5). Looking at the rheology characterization in Figure 10c_6 concerning viscosity versus shear rates, the PEO/LiDFOB/Al_2O_3 (EO: Li = 10:1) showed a slight increase in viscosity as the shear rate increased that did not impact the printability significantly. Thus, the production via aerosol jet printing opens a new path for higher resolution control than often used FDM or SLS in fabricating solid-state LIBs compared to other 3D printing methods.

5. Current Challenges and Future Perspectives

The demand for versatile energy storage devices requires quick tunability, customization, and cost/time efficient production that is highly possible through 3D printing. However, to meet a wide range of needs (i.e., microbatteries, transparent, flexible/wearable, biocompatible, high-energy, high-power density, porous, and lightweight), a few challenges must be addressed. Henceforth, this section will cover essential topics to improve the next generation of LIBs via AM techniques. First, expanding newer materials is necessary as rising applications, manufacturing methods, and industry demands grow. Second, 3D printing resolution is also limited due to specific AM processing characteristics that may hinder the 3D printed microstructure and overall performance. Third, many AM techniques struggle to incorporate complex designs (e.g., porous structures) in flexible manufacturing (e.g., submicron scales) on time, making them unsuitable for scalable applications, though accommodating mass customization is not problematic for 3D printing nowadays. Thus, we would need new manufacturing technology that promises to print complete battery components in a single step or on the same platform with possible comanufacturing techniques applicable to the EES. Fourth, we highlight a few challenges that have hindered uncertainty prediction in ML and AI for the in-situ examination/optimization and data analysis. In addition, we address the environmental challenges related to the reuse and recycling of battery materials. Furthermore, we provide a concise overview of 4D printing, which employs various stimuli sources, as a promising approach for innovative energy storage devices. Additionally, it is crucial to explore alternative materials, including rare metals, considering the finite availability of lithium storage on Earth. Finally, we emphasize the importance of advancing computer technologies, such as artificial intelligence and machine learning, to enhance modeling, prediction, and validation capabilities in the field of energy storage.

5.1. Expand Feedstock Types via Newer Material Synthesis

Exploring new materials for the AM methods is needed to improve the performance of current EES devices. Various printing principles demand materials that are compatible with different AM techniques. For example, a new concept of manufacturing transparent LIBs with flexible, stretchable, and optical properties will require different feedstock formats via complex processing procedures (e.g., possibly a combination between 3D printing and conventional manufacturing).[125,126] Carbon nanomaterials (i.e., CNT, graphene, fullerene) have been preferable due to their fabrication flexibility, transparency at low loadings, and excellent electrical and mechanical properties.[127] For instance, Niederberger et al. developed transparent, flexible thin films and hybrid supercapacitors for energy storage devices through micromolded patterns.[128] They used an ordered mesoporous carbon and nickel-iron-oxide@reduced GO as a high-power anode for a lithium-ion capacitor with a hexagonal grid structure to optimize the transparency. The grid shape pattern strongly influenced the transparency due to the light transmission through the micromolded patterns could enable.[128] The ability to bend to a radius of 3 mm without losing electrochemical properties over 1000 cycles showed an EES with high transparency and flexibility. In contrast, 3D printing can not only rapidly prototype printed patterns but also use a broader range of materials in addition to the nanoscale carbons.

Similarly, many other materials have been developed for energy applications with multiple functionalities. For example, Cui et al. fabricated a flexible, grid-structure electrode with 78, 60, and 30% transparency with an energy density of 5, 10, and 20 Wh L^{-1}, respectively.[129] The electrode was primarily using 90% active materials, either LMO or LTO with 7% CB and 3% aqueous binder to be fabricated by a microfluidic-assisted method. Later, Taylor et al. used single-walled carbon nanotubes (SWCNT) and vanadium pentoxide (V_2O_5) nanowires for anode and cathode electrodes, respectively, to achieve a transparent (>87% transmittance) energy storage device via spin-spray layer-by-layer assembly.[130] This concept required transparent current collectors and electrolytes to complete a functional battery. Thus, they used three Celgard separators in between the electrodes, which showed a capacity retention of ≈5 mAh cm^{-2} over 100 cycles and proved the concept of a fully transparent battery. With higher processing autonomy similar to industry, Salot et al. fabricated a grid-structured thin-film solid-state battery using photolithography and etching processes.[131] Their work showed superiority over previous literature in their discharge capacities ranging from 0.15 to 0.6 mAh at transmittances between 60% and 20% while offering good cyclability over 100 cycles with an average capacity loss of 0.08% per cycle.[131] Achieving these flexible electrochemical devices through various processes requires

with the viscosity as a function of shear rates for several electrolyte composites (i.e., PE, PE-PI, CPE, CPE-PI). Schematic illustration of the b_{10}) polymer electrolyte with PI (i.e., PE-PI), b_{11}) composite electrolyte with ceramic fillers (i.e., CPE), and b_{12}) composite electrolytes with PI (i.e., CPE-PI). Reproduced with permission.[117] Copyright 2017, Wiley-VCH. SEM images of the aerosol jet printed c_1) PEO/lithium difluoro(oxalato)borate (LiDFOB)/Al_2O_3 (ethylene oxide monomer:lithium ion (EO:Li) = 10:1), c_2) (EOS:Li = 16:1), c_3) PEO/lithium trifluoromethanesulfonate (LiTriflate)/Al_2O_3 (EO:Li = 10:1), and c_4) (EO:Li = 16:1), respectively. c_5) Temperature-dependent conductivity graph with PEO/LiDFOB/Al_2O_3 (squares) and PEO/LiTriflate/Al_2O_3 (circles). c_6) Rheology characterization with the viscosity versus shear rate plots for different electrolyte compositions from supporting information. Reproduced with permission.[121] Copyright 2019, Wiley-VCH.

Table 5. Materials potentially used in AM technology for EES. Section terminology in Section 6 (ACT, silver/titanium/chromium; CMC, carboxymethylcellulose; GaInSnZn, gallium-indium-tin; LiPON, lithium phosphorus oxynitride; PAN, polyacrylonitrile; PBuPy, poly(1-pyrenebutyl methacrylate); PBuPyMAA, poly(1-pyrenebutyl methacrylate-co-methacrylic acid); PDHBQS, poly (2,5-dihydroxyl-1,4- benzoquinonyl sulfide); PDI, 3,4,9,10-perylenetetracarboxylic diimide; PEC, poly(ethylene carbonate); PMA, poly(N-methyl-malonic amide); PPC, polypropylene carbonate; Pt, platinum; PTMC, poly(trimethylene carbonate); SWCNTs, single-walled CNTs; Ti, titanium; Ti_3C_2, titanium carbide; ZTO, zinc doped tin(IV) oxide).

Categories	Materials	Compatible AM methods	New applications but not limited to
Current collector	ITO,[133] Ti/Pt[131]	SLA, FDM, DIW	Transparent LIBs
Cathodes	LFP,[133,134] LCO,[131] LMO,[129]	SLA, FDM, DIW, inkJet	
Anodes	Si,[129,131] (ZTO/ACT/ZTO),[133] LTO[129]	SLA, FDM, DIW, inkJet	
Electrolytes	LiPON,[131,133] PVDF-HFP[129]	SLA, FDM, DIW	
	LLZO,[106] LLZTO[135]	SLA, FDM, DIW	Garnet-type LIBs
	PVDF,[136] CMC, PBuPy,[137] PBuPyMAA,[137] PDHBQS-SWCNTs,[138] PDI[125,138]	SLA, FDM, DIW, SLS/SLM, InkJet	Flexible LIBs
	PEO,[139] Poly(ester), nitrile, PVDF-HFP,[140] PMA, polyimide, PEC,[141] PTMC, PPC, PAN[125]	FDM, DIW, SLS/SLM, InkJet	
General electrodes	2D and 3D MXene/Ti_3C_2,[142] GaInSnZn, Si[125,137]	SLA, FDM, DIW, SLS/SLM	
	CNT,[143-146] Gr,[147,148] MXene hydrogels and aerogels[149] 2D and 3D MXene/Ti_3C_2,[142,150] GaInSnZn, Si[125,137]	SLA, FDM, DIW, SLS/SLM	4D Printed LIBs

multistep fabrications. Therefore, additively manufacturing transparent, flexible, and lightweight batteries may take this concept to a new level for electrochemical devices. Expanding current EES materials in 3D printing and combining different nano/micro-sized features with fast customization will lead to better cost and time-efficient production.

Conventional manufacturing can process more battery materials than 3D printing since the latter methods are still primal (e.g., a lack of quick customization on delicate structures, defect density, ink tunability, and feedstock size/shape control). Besides, material innovation has hindered the expansion of 3D printable battery development. As a brief summary, the materials introduced in **Table 5** have been used for different battery components that must be tunable for different AM platforms. For example, the oxide powders (e.g., ITO, LLZO, LLZTO) are usually above the microscale, causing problems in fine-resolution printing. In comparison, the nanoscale carbons (e.g., Gr) of metal carbide/carbonitride (e.g., MXenes) are more flexible with proper pre-processing, such as colloid dispersion or mixing with fluidic monomers.[132] Polymers, on the other hand, are compatible with the majority of 3D printing mechanisms. As the feedstock of electrolytes, polymers can exist in dissolved solutions, dispersed particles in curable monomers, melts to disperse powders, and as binders in laser-printing techniques. However, the light source in lithography-based printing (e.g., SLA or DLP) must adjust these materials to be photo-curable, while the inks must be prepared to accommodate the AM rheology requirements. Though DIW can extrude any material if it meets the rheology parameters, clogging has been a common processing issue. Thus, the new materials-3D printing interaction is an urgent issue to study for battery and other energy-relevant applications.[133]

5.2. Increase 3D Printing Resolutions via Novel Processing Mechanisms

Efficient design and manufacturing of high power-density and energy-density batteries (especially micro-batteries and other microsystem energy devices) will need precise feature control. The printing resolution of specific AM techniques is limited by their manufacturing principles (Sections 1 and 2), especially for complex hierarchical designs (e.g., porous microstructures, layered hierarchies, nanoscale architectures). For example, light-monomer interaction-based printing (e.g., SLA, DLP, CLIP, CAL, TPP/MPP) has shown a printing capability with a satisfactory resolution on the nano-to-micro scale due to either light wavelength or resin monomer design control. **Figure 11**a_1 is an example of μSLA printing using a projection method where the images are sliced and projected to show to the subsequent layer in minutes with features ranging from 10 to 500 μm.[151] Still, the particle distribution and size play a role in the resolution of the prints, but most importantly, the material must be photopolymerizable to print. Figure 11a_2 compares light-based printing methods concerning price and feature size. Generally, the smaller the feature size, the more expensive and time-consuming the manufacturing methods. Therefore, there is room to optimize printing the submicron and micron scale in a cost and time-efficient manner. Nonetheless, light-based printing can accommodate various materials (e.g., polymers, ceramics, glass, and metals, as mentioned in Section 2.1). Yet, printing specific energy storage materials is limited, and most require tunability and post-printing techniques to achieve desired printing resolutions or hierarchies (e.g., Figure 11a_3). Further optimization of light-based printing platforms for a higher processing precision and a broader range of materials is still needed.

For the filament base printing method, the 3D printing resolution of the FDM machines is dependent on to the nozzle sizes, printing parameters, and material characteristics. For example, most printers will have a nozzle inner diameter of 0.1 mm to 0.8 mm based on nozzle types, and materials, object size, design complexity, and machine specifics that could also limit 3D printing resolutions.[152,153] Similarly, the DIW is also constrained to the nozzle diameter, typically found in conventional syringes or needles that can be custom-made.[154] Hence, the printing resolution for the filament-based method is primarily constrained to the nozzle diameters, particle sizes, and feedstock rheologies.

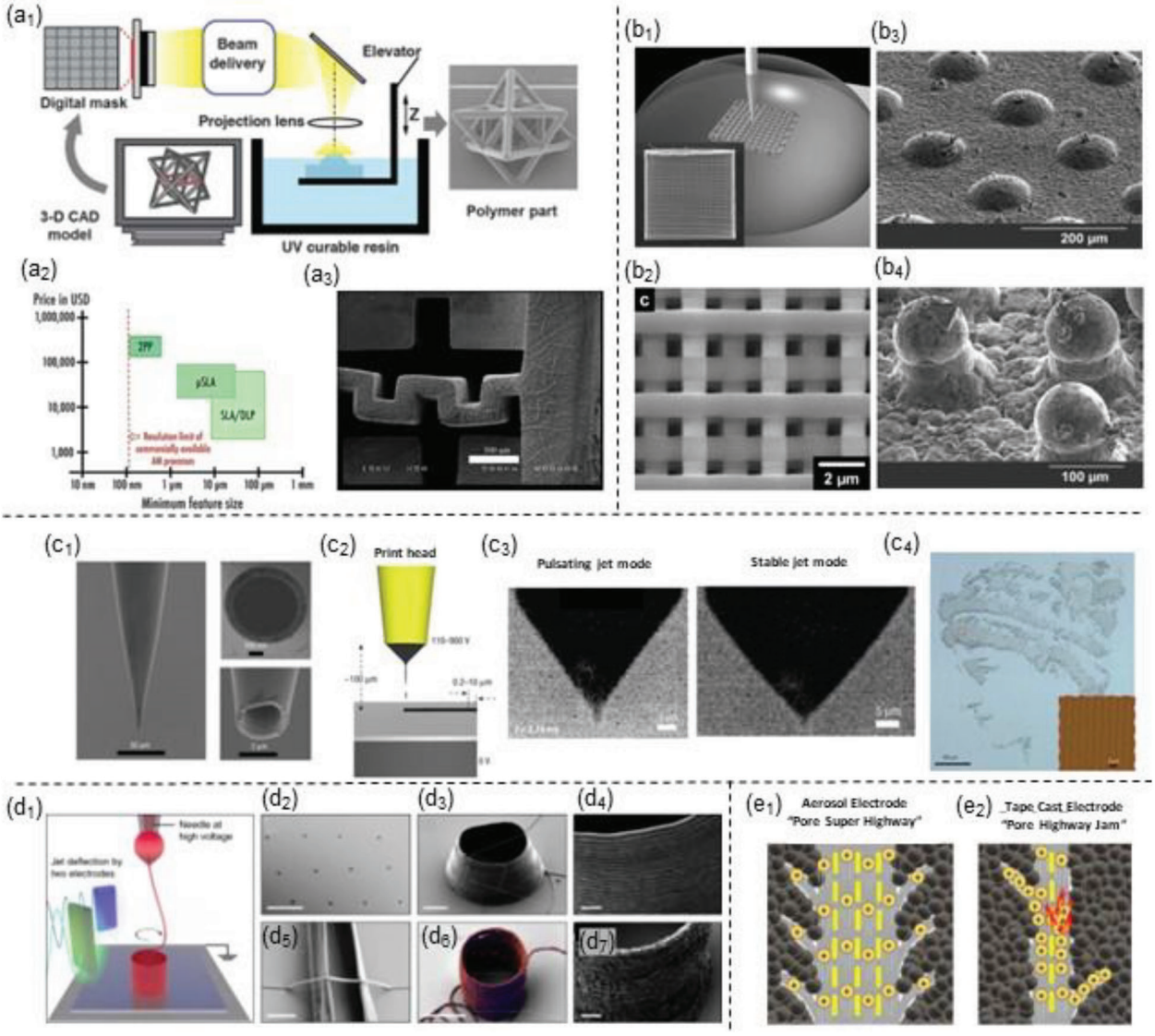

Figure 11. Comparing printing resolutions from different 3D printing techniques. a_1) Schematic of projection μSLA with the capability of producing ultralight, ultrahigh-stiffness, stretch-dominated micro-latices with a resolution of ≈5 μm. Reproduced with permission.[151] Copyright 2014, AAAS. a_2) Comparison chart of different light-based printers with price versus feature size. Reproduced with permission.[161] Copyright 2021, IEEE. a_3) Demonstration of solid electrolyte printed via light-based printing for a zig-zag patterning, with 500 μm scale bars. Reproduced with permission.[107] Copyright 2017, The Electrochemical Society. b_1,b_2) DIW of a 250 μm × 250 μm woodpile structure in addition to hollow-woodpile design with resolutions of up to 1 μm. Reproduced with permission.[155] Copyright 2006, Wiley-VCH. b_3,b_4) Example of DIW printed solid electrolyte in (b_3) conformal configuration and (b_4) self-supporting configuration. Reproduced with permission.[106] Copyright 2018, Wiley-VCH. c_1,c_2) Electrohydrodynamic (EHD) Jet-based 3D printing with a gold-coated glass microcapillary nozzle (2 μm internal diameter) c_3) comparing the pulsating jet mode versus the stable jet mode during printing (e.g., an image of c_4) Hypatia printed using polyurethane ink with a 500 nm internal diameter nozzle), at a 5 μm scale bar. Reproduced with permission.[162] Copyright 2007, Springer Nature. d_1) EHD representation using electrostatic jet deflection. d_2–d_4) SEM micrographs for 3D cylindrical PEO microstructures, with 200 μm, 5 μm, and 1 μm scale bars in (d_2–d_4), respectively. d_5) SEM micrograph of a PEO fiber. The scale bar is 2 μm. d_6,d_7) SEM and zoom-in micrographs of a PEO-(Ag) cylindrical structure. Scale bars are 5 μm and 1 μm. Reproduced with permission.[160] Copyright 2020, Springer Nature. e_1,e_2) Aerosol jet printing of LFP cathode with "pore superhighway" versus the tape cast electrode. Reproduced with permission.[102] Copyright 2021, American Chemical Society.

Moreover, complex structures in the macro-nano scale are helpful for battery processing, but more delicate architectural requirements can negatively affect the printing speed. This trade-off makes extrusion-based printing advantageous for submicron composition and physics design. For example, most ink-writing-based 3D printing methods have a limit of nozzle sizes that usually leads to a deposition feature of tens of microns. However, Ellis et al. demonstrated the ability to print high-resolution lattices of up to 1 μm, as shown in Figure 11b_1,b_2, for the 250 by 250 μm woodpile structure to achieve a microcapillary nozzle of a diameter of 0.5 to 5.0 μm.[155] Wachsman et al. also demonstrated the ability to print exceptionally fine resolutions via the DIW method, as shown in Figure 11b_3,b_4 for the LLZO SSEs in both "conformal" and "self-supporting" configurations,

respectively.[106] The ability to have multiple nozzles working simultaneously to print complete or large geometries to speed up the battery printing process is also worth mentioning. However, the calibration and coordination of multiple nozzles become more complex, which can lag the manufacturing process or require additional machine coding/data analytics. Besides, the control of thermodynamics and kinetics is significantly affected in printing large-format systems compared to small-scale parts.[156]

In contrast, PBF-based 3D printing (e.g., SLS and SLM) may rely on layer sizes, powder types, and laser-powder interactions to determine the manufacturing sizes. As a result, achieving ultrafine-size powders in the micro to the nanoscale is often labor-intensive and expensive, requiring multistep processes for breaking down the particle sizes. For example, the PBF production via SLS to print Gr, Ni, CNTs, GO, and similar 3D carbon materials show enormous potential to be used for battery application but requires the particle size to be in the submicron scale and have a uniform distribution to be printable in the submicron to micron scale.[86,157] Hence, the nature of the materials in a powder form often hinders the quick tunability of the feedstocks due to the rigorous process (mechanical milling, ultrasonication, sieving, and laser/thermal ablation) of synthesizing in each iteration. It is often common to see rougher surface finishes after printing, which requires post-processing (i.e., polishing, etching, coating), typically due to the particle size, distribution, shape regularity, diffusion of particles with the neighboring ones, and fluidity affecting the smoothness and thickness of the layer.[158] Generally, these 3D printing methods for batteries mostly produce a dot or line size above 10 μm and may lose the resolution below a single-digit micron size.

Conventionally, ink jet-based 3D printing has broad applications in quickly processing microscale energy devices. However, ink-based printers, commonly known as PolyJet or MultiJet, cannot print submicrometer dimensions, especially for energy applications involving powder particles. Figure 11c_1,c_2 show the new jet-based 3D printing, electrohydrodynamic (EHD) jet printing, which uses microcapillary nozzles that are turned from a pushing jet mode as compared with a stable jet mode, as shown in Figure 11c_3, which allows printing dimensions as small as 1 μm, as presented in Figure 11c_4 with an image of Hypatia as an example. EHD printing has broad material compatibility with insulating and conducting polymers, SiNPs, and SWCNTs. For example, Steiner et al. used EHD to print CNTs with resolutions as low as 50–80 μm.[159] Similarly, Cabot et al. developed an ultrafast EHD with submicron features using electrostatic jet deflection, as shown in Figure 11d_1. The team printed PEO and Ag nanoparticles with features in the submicron scale displayed in Figure 11d_2–d_7, further proving the potential for micro-nano battery manufacturing.[160] Another high-resolution 3D printer capable of high-resolution printing, aerosol jet, utilizes microcapillary nozzles that allow the resolutions to be in microns and nanometer size. For instance, Rottmayer et al. printed polymer composite electrolytes for SSB applications using aerosol jet printing capable of submicron scales.[121] Rodriguez et al. also printed LFP cathodes via the jet printer and demonstrated superior cycling performance due to the dual-pore network, otherwise referred to as "pore super highway," as shown in Figure 11e_1,e_2.[102]

5.3. Embed Codesign Concept via Integrated Comanufacturing at the System Level

While most of the papers in the AM for LIBs have focused on active materials, there has been a lack of focus on the materials used for battery packaging design, current collectors, and nonactive materials. Regarding 3D printing, most literature investigations have focused on printing a single nonactive component before integrating the entire battery. For example, Bruce et al. created a template using SLA to introduce only solid ceramic-polymer electrolyte structures, with a focus on achieving resolutions of up to 250 μm, a high resolution as the advantage.[163] Another example from Rapp et al. showed a 3D printable housing device for batteries before being used in microcontrollers for microfluidic sensors.[164] In an assembly, Kar et al. used carbon fibers to overlay the cathode, SPE, anode, and current collector through electrophoretic deposition and dip-coating methods in wearable electronics.[165] Also, Zhang et al. focused on fabricating Si/carbon nanofibers as a high-energy anode for LIBs via coaxial electrospinning as a facile and effective method to fabricate 1D free-standing nanofibers.[166] The resulting anode displayed a high storage capacity of 762.0 mAh g^{-1} at a specific current of 0.1 A g^{-1} after 100 cycles. Though with high performances, most of these studied battery components have focused on the single component fabrications before mechanically assembling them for practical devices, similar to practices in the industry. 3D printing as a supply chain disrupter can process many different materials for rapid prototyping, showing massive potential in fabricating and assembling individual components during manufacturing.

Those focused on manufacturing complete LIBs require multiple steps and pre/post-fabrication processes to achieve system-level batteries. However, not many studies reported the entire manufacturing and assembly of batteries via 3D printing to incorporate battery design, processing, and packaging.[71,77,83,104,118] To solve this problem, a few research groups have studied coaxial printing for batteries where the cathode, anode, electrolyte, and packaging can all be manufactured in a single print.[120,167] As one trial, coaxial printing, typically composed of an outer and an inner needle, allows for printing multi-material potentially useful for assembling multiple battery components during fabrications.[168] For example, Golodnitsky et al. fabricated all-SSEs sandwiched between electrodes and their core component of current collectors using a coaxial fabrication method, as shown in **Figure 12**a_1.[120] While their primary focus was on the electrolyte composed of LiTFSI, PEO, and PLA for enhanced mechanical properties, they carried out characterization methods through SEM, mass spectroscopy, and differential scanning calorimetry (DSC), with the electrochemical impedance spectroscopy (EIS) and charge and discharge cycles demonstrated in Figure 12a_2,a_3. They found that adding PLA in the FDM-printed electrolyte enhanced the mechanical properties of the PEO, but it also served as a Li-ion conductor. The corresponding bulk ionic conductivity showed a 3×10^{-5} S cm^{-1} at 90 °C and 156 Ω cm^{-2} SEI resistance that paved the way for free-form-factor flexible geometries for the all-solid-state batteries through coaxial printing.

Similarly, the same strategy via layering multiple materials can transfer to ink-based direct writing. Most recently, Ding et al. reported a universal coaxial 3D-printing strategy in 2022

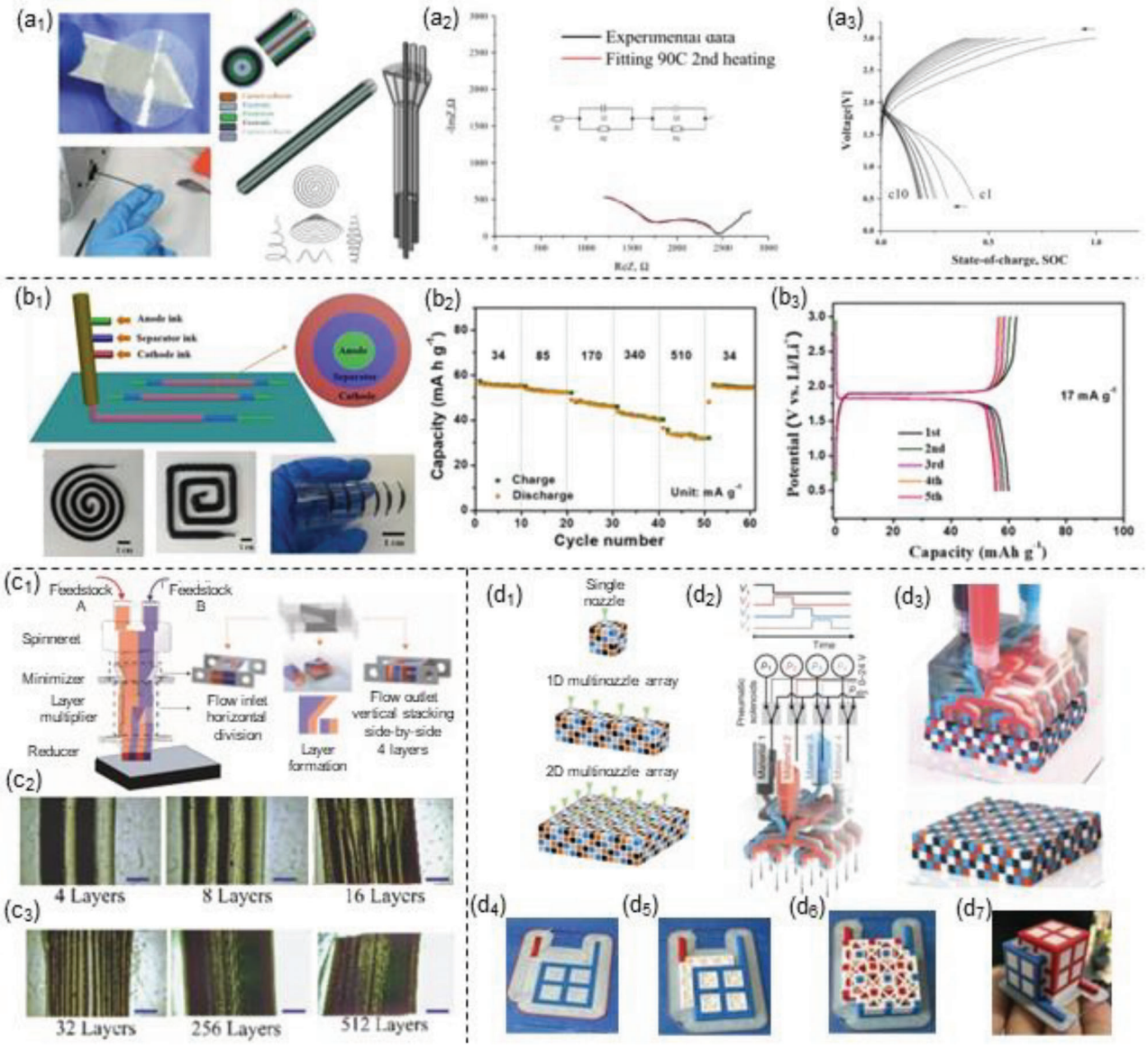

Figure 12. Representation of the co-design and co-manufacturing techniques. a_1) Schematic of the printhead design for FDM printing capable of multi-coaxial-cable battery processing, designed with different nozzle configurations for the flexible coaxial battery. a_2) Nyquistic plot of the composite solid-state electrolyte (SSE) and a_3) the charge and discharge profiles at consecutive 10 cycles. Reproduced with permission.[120] Copyright 2020, The Electrochemical Society. b_1) DIW for the coaxial printing of fibrous batteries with flexible straight lines, mosquito coils, and square coils. b_2,b_3) The electrochemical performances of the coaxial LIBs. Reproduced with permission.[167] Copyright 2022, Elsevier. c_1) Schematic of the multiphase direct ink writing (MDIW) with an intricate design of the unique 3D printhead showing the multiplying procedure capable of splitting multiple feedstocks, restacking them along different directions, and recombining them along the deposition direction. c_2,c_3) The MDIW-printed multiplied layers (i.e., 4, 8, 16, 64, 256, 512) showed distinct layers up to 256 layers (a resolution of 5 µm for sublayer features), while the 512 layers showed layer disruption due to the larger particle sizes than sublayer width. Reproduced with permission.[169] Copyright 2021, Elsevier. d_1) Voxalated architectures using the single, 1D multinozzle array and 2D multinozzle array, respectively. d_2) Schematic illustrates the printhead operation to print (d_3) up to four materials in a single deposition. Reproduced with permission.[170] Copyright 2019, Springer Nature. d_4–d_7) Photos show the preliminary results of printing multiple materials in a single deposition for battery applications via extrusion-based 3D printing. Reproduced with permission.[171] Copyright 2022, HAL.

to fabricate the all-in-one fibrous LIBs in one step, as shown in Figure 12b_1.[167] Using LTO and LFP as the active materials with the separator filament via DIW, they fabricated straight lines, mosquito coils, and square coils. For example, the LIBs displayed a high-storage capacity as 510 mAh g^{-1} and a long cyclability of 100 cycles which can be seen in Figure 12b_2 and the potential versus the capacity plot in Figure 12b_3.[167] It is worth noting that their work also focused on sodium-ion batteries (SIBs) and aqueous zinc-ion batteries (AZIBs), demonstrating the ability of coaxial printing to assemble/test different batteries through a single fabrication process quickly.

Coaxial printing has paved a new way for the battery application to facilitate and optimize the fabrication process cost-effectively and timely. Still, this technology needs further opti-

mization in the interlayers between the separator and active materials for higher performances since the current coaxial printing mechanism has a limit of structural parameters (e.g., the layer thickness or the sublayer numbers). Ravichandran et al. recently reported in the year of 2022 an alternative manufacturing technique, i.e., multiphase direct ink writing (MDIW), as shown in Figure 12c$_1$.[169] The MDIW could deliver feedstock materials A and B simultaneously before multiplying them in the order of 2^{n+1} to print in the range of 4, 8, 16, 64, 256, and 512 layers (Figure 12c$_2$,c$_3$). During the multiplying mechanism, the feedstocks were injected into two channels, split along the vertical direction, and re-stacking along the horizontal direction to maintain a good layer resolution (Figure 12c$_1$). The maximum number of layers from a single deposition could experimentally go up to 1024 sublayers with proper material selections, corresponding to an individual layer thickness as high as ≈44 nm. The structural robustness was demonstrated using polyvinyl alcohol (PVA) and CNTs, showing much-improved modulus, strength, and toughness. Via the same method, a few more polymers (i.e., thermoplastic polyurethane with varying polymer chain sizes and stiffness values) and NPs (i.e., iron oxide) were also incorporated for intelligent devices. The dual actuation in the printed composites showed high actuation efficiency responsive to thermal and magnetic fields. Thus, the potential to use the co-manufacturing technology in energy-relevant applications can apply to electrode fabrication or supercapacitor assembly.

Another unique technique is the multi-material multi-nozzle 3D (MM3D) printing method, where the design and materials are translated into a voxel design displayed in Figure 12d$_1$. The configuration of the MM3D printer can have a single nozzle, a 1D multi-nozzle array, or a 2D multi-nozzle array. Figure 12d$_2$ shows the printhead mechanism where the voltage is applied and changed to affect the deposition pressure with printable origami structures, soft-robotic walkers, and voxelated facilities while reducing the printing speed. It is worth noting that this method could implement up to four materials, as shown in Figure 12d$_3$, and get perplexing patterning and structures. More importantly, it brought attention to the capability of printing multimaterial batteries in a single deposition that can be cost- and time-efficient. As a result, Figure 12d$_4$–d$_7$ demonstrated the preliminary results of printing a complete cube lattice battery via FDM as a multimaterial method similar to the voxelated MM3D printer. It is worth noting that these methods with co-design and co-manufacturing capabilities are mostly extrusion-based, which needs further expansion in other printing mechanisms, better material form capability, and energy storage applications. In sum, the features of the co-design and co-manufacturing techniques will allow for faster customization, tunability, and integration of different energy storage devices.

5.4. Improve Uncertainty Prediction and In Situ Quality Examination Using Data Science

Current 3D printing for processing new materials or tuning printing parameters (e.g., ink rheologies or optimizing structure designs) has been done through empirical and trial-and-error methodology, which is expensive and time-consuming. The rapid development of advanced data analytics with ML and Artificial Intelligence (AI) allows fast research and development in battery 3D printing. These data analytics methods are based on powerful ML and AI algorithms (e.g., Bayesian analysis and deep neural network algorithms) facilitated by combining them with in situ monitoring via creative tooling engineering (e.g., 4D scanners, micro-CT, high-rate cameras, and on-platform optical microscopes).[172] ML and AI techniques have demonstrated tremendous promise in mining 3D printing data. Emerging research now seeks to find ML-driven solutions that can make anticipatory predictions and achieve born-qualified products beyond how traditional in-situ monitoring and control and ex situ evaluation have been done.[173] On the one hand, the datasets in the battery materials are relatively small, with multiple variables. The scarcity of data is one of the biggest problems. Future researchers should adopt multimodal in-process sensors to collect in situ measurements for numerous variables in real-time to address these limitations. The in-situ monitoring sensors measure various process signatures representing the links between process control and final part quality. Process signatures measure real-time dynamic characteristics of physical properties during 3D printing operations and give process physics and part quality information.[174,175] Examples of the process signatures are data measuring the real-time evolution of 2D or 3D part geometries and temperature during a build.[176] Such process signature data enable ML studies to understand better the mechanisms of 3D printing dynamics, e.g., thermo-dynamics, hydro-dynamics, fluid-dynamics, or chemical reactions.[177] In addition, data augmentation using advanced ML approaches, such as generative adversarial networks, can be considered to increase data availability.[178]

On the other hand, the lack of formal methodologies and standardized frameworks defining the model and experimental variables and parameters further delays the data acquisition for ML and AI modeling; a significant challenge for ML in 3D printing today is that data acquisition is still ad-hoc.[173] This challenge hinders the systematic adoption of advanced ML and AI in battery 3D printing. The variability of batteries with their shapes, sizes, materials, and applications comes with different relationship predictions and experiments and, therefore, other variables and parameters at multiple scales. Predictive ML using the variables and parameters entails the acquisition of data of interest, which needs to be guided by physics knowledge used in formulating ML and experimental requirements for battery 3D printing. In this sense, 3D printing data must be associated with physics knowledge about the batteries and their printing processes methodically. Such an association enables the systematic acquiring battery and 3D printing data from actual, physical, or simulated virtual 3D printing systems and extracting the data features representing the variables and parameters in terms of battery 3D printing.[179] By doing so, ML can be consistently based on the physical meanings of measurable quantities in iterations using associated mathematical relations.

Finally, the lack of model interpretation is also a challenge in ML due to the complexity and usability of the model when it comes to materials research.[180] It is crucial to overcome these challenges to increase in situ optimization and on-the-fly battery manufacturing. To address the challenge, studies in battery 3D printing need to adopt explainable AI (XAI), especially for deep learning methods.[181] Pursuing XAI, the interpretation must represent the findings of casual relationships in predictions from

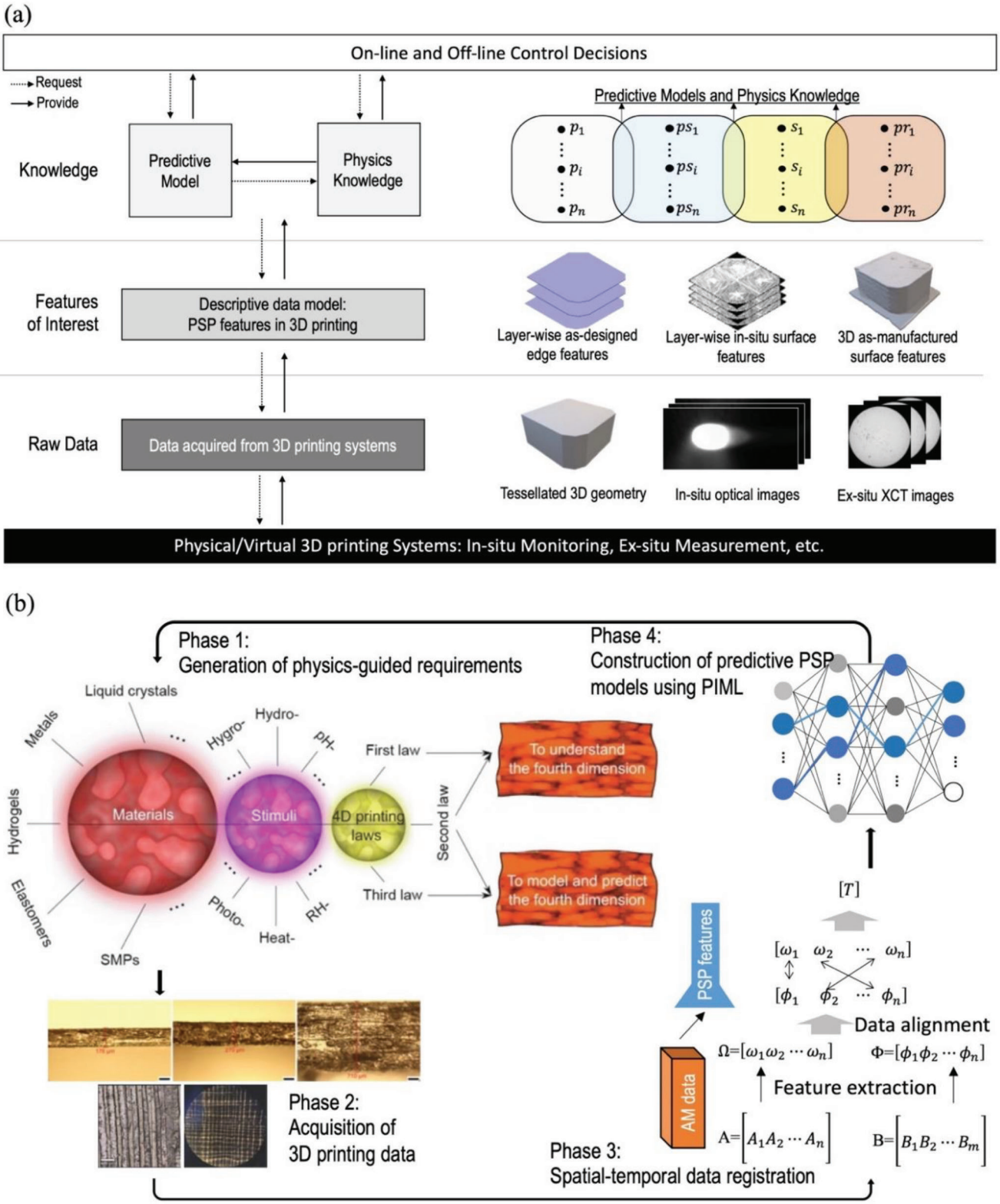

Figure 13. a) An overall framework for ML-driven process–structure–property (PSP) analytics in AM ($\{p_1, p_2,..., p_n\}$, $\{ps_1, ps_2,..., ps_n\}$, $\{s_1, s_2,..., s_n\}$, and $\{pr_1, pr_2,..., pr_n\}$ are sets of entities of process parameters, process signatures, structures, and properties, respectively). Reproduced with permission.[175] Copyright 2023, Elsevier. b) A process of learning PSP causality using physics-guided data acquisition and ML to improve the quality of 3D printing. A and B represent raw data sets. **Ω** and **Φ** represent PSP features extracted from A and B, respectively. T represents aligned data sets.

Table 6. Current challenges in the recovery and recycling of LIB with corresponding descriptions.

Challenges	Descriptions	Refs.
Safety and hazards	LIBs contain highly flammable and reactive materials, such as lead, cadmium, mercury, and lithium, requiring specialized equipment and protocols for safety	[206]
Collecting and sorting complexity	Batteries comprise a complex mix of (i) materials, including metals, plastics, and electrolytes; (ii) material physics and chemistry (e.g., sizes, shapes, compositions); and (iii) end-of-life stages, requesting advances in autonomous sorting and processing tools	[183]
Degradation	Degradation during the battery's initial use and subsequent recycling processes makes the performance standards challenging to meet, requesting new material synthesis and processing design	[207]
Scalability	Battery recycling involves complex processes (e.g., disassembly, crushing, and chemical treatment), which require specialized scalability	[183]
Economic viability	Direct recycling is still more expensive than mining and refining new materials due to the high cost of equipment, labor, and energy required to recover the valuable materials, making it difficult for the recycling industry to compete	[208]

ML in structured relationships.[182] Such techniques help provide the independence of the knowledge extracted from the ML models, which is expected to offer new opportunities to improve a priori physics knowledge.[182] Physics-informed (or -guided) ML for Process-Structure-Property (PSP) causal analytics can advance the interpretation of the models in battery 3D printing. The PSP approach can associate the XAI approaches with the critical causal linkages between process mechanisms and part characteristics in battery 3D printing processes. The physics-informed ML approaches can fuse physics equations with real-world data to enhance the interpretation of predictions resulting from ML about the physical meaning of 3D printing processes and battery characteristics in extracting the PSP causal linkages. The PSP linkages can be advantageous when they include the process signatures supporting monitoring constant dynamic changes during battery 3D printing processes, which helps better understand the dynamics of the printing processes. **Figure 13**a shows a framework driven by physics-guided ML for PSP causal analytics in 3D printing, consisting of three tiers: 1) knowledge of predictive PSP models and physics, 2) PSP features of interest, and 3) raw 3D printing data (Figure 13b) showing a process of learning PSP causality for 3D printing based on the framework.

5.5. Mitigate Environmental Risks via Battery Recovery

As demand increases, the material recovery from used batteries is crucial for developing more environmentally benign, chemistry-green, and cost-efficient batteries. However, battery recycling is a complex process that involves several technical, economic, and environmental challenges (**Table 6**). First, the recovery and recycling of metal salts and cathodes have three primary methods, which involve hydrometallurgical, pyrometallurgical, and direct recycling, as illustrated in **Figure 14**a.[183,184] Hydro and pyrometallurgical methods are preferred for recovering metals (i.e., lithium, cobalt, Ni, manganese, and aluminum) due to their well-established protocols and widely used instruments. Due to its ecotechnological advantages, direct recycling is preferred to conventional pyro and hydrometallurgical processes. Also, direct recycling is based on thermal or acid solution treatments for relithiation that allow the recyclability of primary electrodes, metals, and plastics. Categories under direct recycling consist of numerous methods (i.e., solid-state, electrochemical, ionic liquids, eutectic and solution-based) as shown in Figure 14b_1–b_5.

The first step in general battery recycling is electrolyte treatment, which involves extracting CO_2 and organic solvent from the electrolytes to be reused. However, recycling electrolytes is challenging due to i) the solvent's volatility ii) the Li salts' instability, iii) and the high processing cost of recycling electrolytes. Thus, electrolyte recycling may better adapt as all-solid-state batteries emerge in 3D printable batteries involving SSEs in polymers, ceramics, or composites. For example, Zhang et al. attempted to recycle garnet-type batteries for the c-LLZTO electrolyte demonstrated in Figure 14c.[185] Using ball-milling and sintering to purify the LLZTO SSE and then adding fresh LLZTO, they were able to obtain a relative density of 95.9%, close to the original garnet electrolyte. However, the reused particles of the LLZTO were not as stable as the new particles after they were sintered, causing weak grain fusion during sintering.[185] While the performance of the recycled SSE did not achieve the desired performance, it still showed the capability to be used as a sacrificial powder typically seen in synthesizing LLZO. It is worth noting that the manufacturing process of garnet-type electrolytes is often expensive, and finding a way to reuse the materials can bring the cost of the overall material and manufacture down.

After the separation of electrolytes, the electrode is processed for recycling. Direct recycling techniques have been the mainstream processing for recycling many electrodes (i.e., LFP, LCO, NCA).[183,186] For example, Cheng et al. developed a new method for directly recycling cathode material LFP using lithium salt (i.e., 3,4-dihydroxy benzonitrile dilithium salt, Li_2DHBN).[187] The lithium salt allowed for the Fe(III) purification, responsible for the capacity fades of the LFP cathode. Figure 14d_1 shows the crystal structure comparison for the degraded and restored LFP cathode using organic lithium salts, as shown in Figure 14d_2 for comparing organic versus inorganic lithium salts. The salts created an amorphous carbon layer coat in the LFP while purifying the LFP cathode enabling good cycling stability and low-temperature performance for the restored cathode material, as shown in Figure 14d_3.[187] According to the techno-economic analysis performed in the EverBatt2022 model, this study showed a higher potential financial benefit than many other recycling methods, further enabling a new recycling method that is both cost and time efficient. Moreover, there are a few selectively

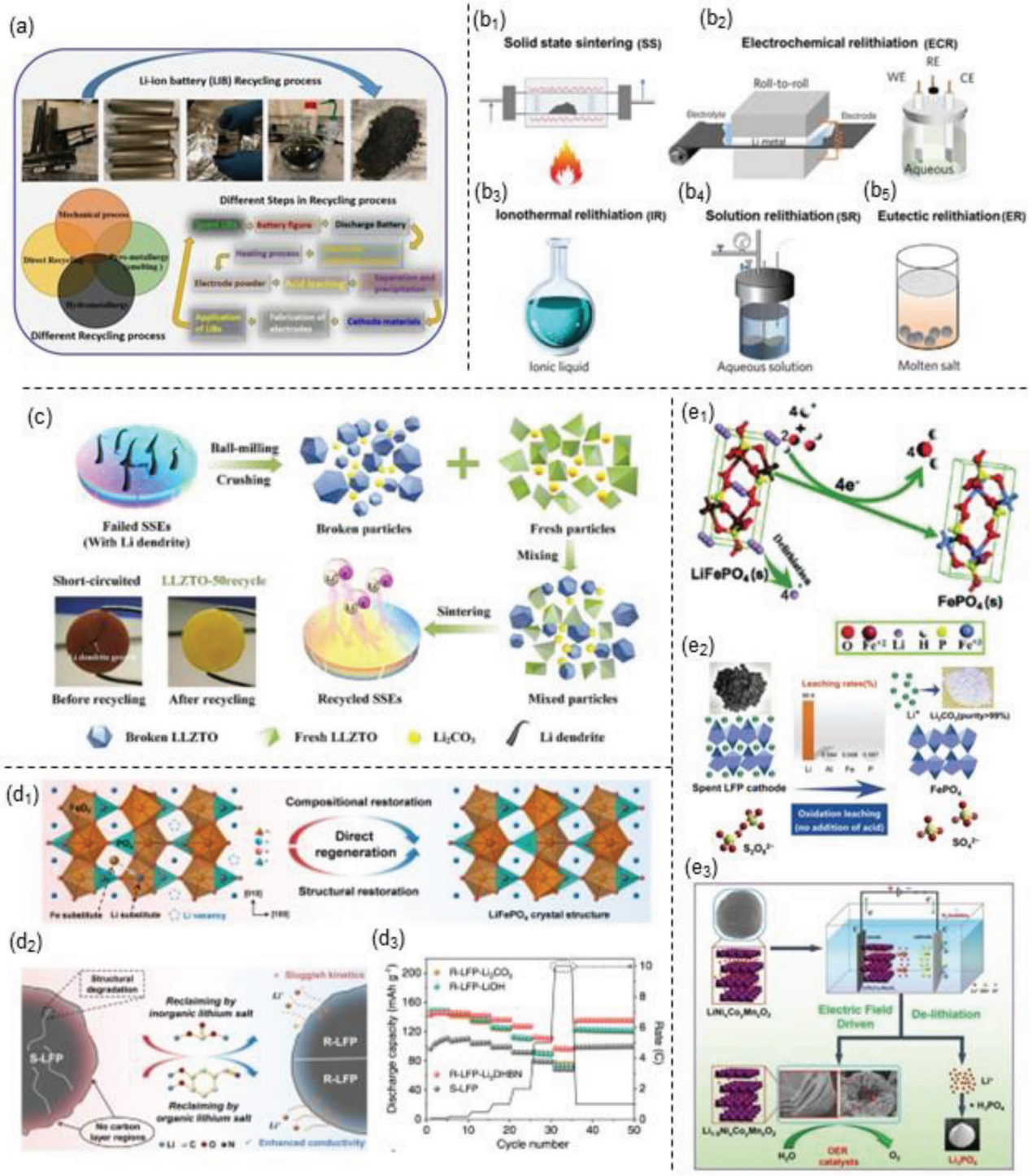

Figure 14. Different LIB recycling with a) four conventional battery recycling methods. Reproduced with permission.[184] Copyright 2021, American Chemical Society. Illustration of the direct recycling techniques of b_1) solid-state sintering (SS), b_2) electrochemical relithiation (ECR), b_3) ionothermal relithiation (IR), (b_4) solution relithiation (SR), and b_5) eutectic relithiation (ER). Reproduced with permission.[183] Copyright 2023, Wiley-VCH. c) Schematic representation of the recycling of ceramic-based tantalum doped, lithium lanthanum zirconium oxide (LLZTO) electrolyte. Reproduced with permission.[185] Copyright 2023, Elsevier. Regeneration of cathodes using lithium salts d_1) comparing the degraded and restored crystal structure for the LFP cathode. d_2) General recycling processes for the LFP comparing both the inorganic and organic lithium salts. d_3) Discharge capacity profile versus cycle number comparing the regenerated cathode and the degraded LFP. Reproduced with permission.[187] Copyright 2023, Spring Nature. Selective leaching methods for lithium metal (LiM) e_1) from cathode-based LFP materials with acetic acid and H_2O_2 versus e_2) persulfate and e_3) from lithium nickel-manganese-cobalt oxide (NMC) cathode using an electrochemical method. Reproduced with permission.[192] Copyright 2021, Royal Society of Chemistry.

leaching techniques when it comes to recycling LiM. For example, Sun et al. selectively recovered lithium from LFP cathode material using acetic acid and H_2O_2, showing a facile method of recycling lithium, as shown in Figure 14e$_1$.[188] Similarly, Wang et al. leached lithium from an LFP cathode using persulfate, as shown in Figure 14e$_2$.[189] Also, Goodenough et al. used similar materials, such as H_2SO_4 and H_2O_2. However, Sun et al. used hydrothermal treatment to selectively leach lithium from lithium nickel-manganese-cobalt oxide (NMC) cathode material.[190,191] Figure 14e$_3$ further shows the leaching of lithium from the NMC electrode but using an electrochemical method.[190,192]

The separation of materials is essential, and when it comes to polymer recycling, it is not as common as the active materials from a battery. In 2016, Jiangnan Graphene Research Institute filed a patent for a new method of recycling separator material of LIBs using organic solvent and ultrasonic washing, which promises efficient recycling of separators in a resourceful, cost, and economical manner.[193] In 2020, Aravindan et al. focused on regenerating polyolefin separators from secondary LIBs through cleansing and washing methods using only deionized water.[194] Through characterization techniques, including tensile strength, differential scanning calorimetry, ionic conductivity, electrolyte uptake, and interfacial resistance, they concluded that the recycled separator works as efficiently as the virgin material.[194]

Several companies are focusing on recycling polymers from batteries. Li-Cycle uses a process called "spoke and hub" recycling, while Retriev Technologies uses a hydrometallurgical process to recycle batteries.[195,196] Similarly, Umicore uses a combination of pyrometallurgical and hydrometallurgical processes to recover metals primarily from batteries, but also plastics and other materials from the batteries.[197] Fortum also uses a hydrometallurgical process to recycle batteries. In addition to these companies, many have expressed interest in recycled batteries for EVs. General Motors has announced plans to build a factory in Ohio to produce battery cells for its EVs, with a focus on sustainability and recycling.[198] BMW has partnered with recycling companies to create a closed loop for its EV batteries, while Tesla aims to become a "closed loop" company, meaning it wants to recycle its own batteries and reuse the materials.[199-201] Nissan has a program called "LEAF to Home," which allows Nissan LEAF owners in Japan to use their car batteries to power their homes during peak electricity usage hours. After a certain number of years, the batteries are returned to Nissan for recycling.[202] Furthermore, research groups and universities are also working on developing new and innovative methods for recycling batteries.

While presenting future outlooks and state-of-the-art recycling methods, the battery recycling industry remains deficient, facing many challenges (Table 6).

(i) Safety and Hazards—Recycling facilities need robust safety measures and protocols to prevent exposure to these hazardous materials.
(ii) Collecting and sorting complexity—Identifying, separating, purifying, and reusing materials is challenging to be cost-efficient and environmentally friendly.
(iii) Degradation—New material synthesis (e.g., biometallurgy[203] or processing electrochemically[204,205]) will benefit the material robustness in recycling.
(iv) Scalability—Developing efficient and cost-effective recycling technologies and instruments that can handle large volumes of batteries is necessary to ensure the sustainable use of materials.
(v) Economic viability—The economics of battery recycling depends on the market prices of the materials, which requires collaboration between various stakeholders, including government, industry, and academic researchers.

3D printable batteries and other electronics have shown enormous potential to revolutionize many industry fields, and the recycling of printed devices should be considered before similar contamination issues in conventional manufacturing appear.

5.6. Diversify Device Intelligence via 4D Printing

AM of intelligent/innovative dynamic structures, i.e., 4D printing, has primarily been composed of shape memory alloys (SMAs) and shape memory polymers (SMPs), which are smart materials capable of changing size, shape, or color under the influence of external stimuli (i.e., pressure, heat, light, water, pH, electrical or magnetic fields).[209-211] The potential applications of 4D printing are diverse and include self-assembling robots, medical implants that can adapt to the body's changing conditions, and building structures that can adjust to changing environmental conditions. For example, 3D printable PLA inks as SMP from direct writing retained excellent shape after UV-curing (**Figure 15**a$_1$) with thermal responsiveness.[212] Different structures rapidly prototyped from the 3D printing procedures, e.g., the spiral, wavy, and flower-like, exhibited high flexibility in changing their shapes upon heating and efficiently recovered to their original sizes upon cooling (Figure 15a$_2$–a$_4$).[212] Foldable assembly via 3D printing (Figure 15b) could also be susceptible to thermal stimuli that can act as a robotic gripper upon heating or cooling.[213] SMP is useful in 4D printing, with Figure 15c demonstrating the capability to print living materials, such as S.boulardii-TRP1 and LEU2, which grew upon appropriate biochemical stimuli.[214] Figure 15d$_1$–d$_4$ also shows a 4D-printed hand that accurately opens upon radiation, such as infrared light.[215] The functionality is not restricted to just the gripper but can also be used as a triggered alarm system. Figure 15d$_5$–d$_8$ shows an example of a dual-motor triggering alarm system that used 4D printing to be stimulated via radiation to switch to the alarm system.

Although 4D printing is still a relatively new technology being developed and refined, it opens new avenues for electrochemical applications, such as energy storage devices (e.g., batteries, capacitors, fuel cells, and sensors). Using innovative materials that can change their properties in response to external stimuli, 4D printing can create electrochemical devices that adapt to changing conditions or perform multiple functions. For example, 4D printing batteries can accommodate the volume change from the electrodes by changing their shape from outside stimuli, especially in soft packaging materials. Hu et al. designed a simple and scalable extrusion-based 3D printing on DIW for fiber-shaped LIBs.[216] The 3D-printed anode and cathode electrodes shown in Figure 15e$_1$,e$_2$ showed the merits of 3D printing with high manufacturing customizability and cost efficiency. More importantly,

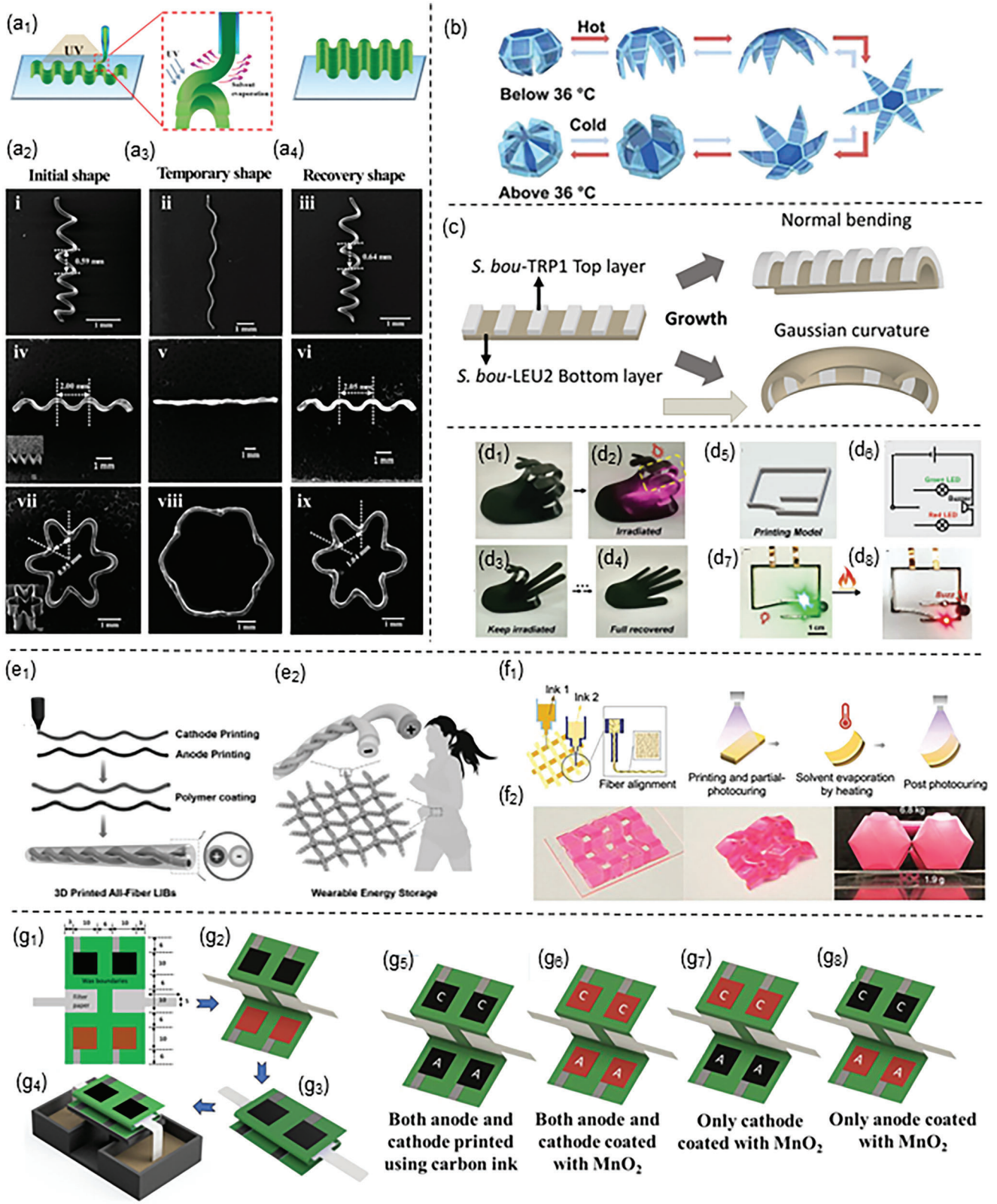

Figure 15. Schematic diagram of different 4D printing techniques for printing/assembling stimuli-responsive objects and their relationship to energy devices. a_1) 4D active shape-changing architecture through ultraviolet (UV) cross-linkable PLA-based ink and a_2–a_4) shape-morphing structures (i.e., the micro spiral pattern through heat stimuli in images (i–iii), waviness-like shape in images (iv–vi), and flower-like configuration in images (vii–ix). Reproduced with permission.[212] Copyright 2017 American Chemical Society. b) 4D printable, reversible, and self-holdable micro grippers in response to the thermal fields (i.e., temperature-responsive). Reproduced with permission.[213] Copyright 2015, American Chemical Society. c) Schematic of a

the extruded anode/cathode composites were automatically assembled and packaged within the fibers. The packaging of fibers showed excellent surface smoothness and continuous length, with initial charge/discharge capacities of 141.3 and 110 mA h g^{-1}, respectively. Most recently, Qi et al. 4D printed fiber reinforcement composites via DIW for self-morphing structures activated through thermal stimulation.[217] Figure 15f_1,f_2 illustrates the 4D printing process where a photocurable polymer is mixed with the glass fiber and fumed silica to be extruded via DIW and cured through UV light. The printed structure was then exited thermally, which evaporated the solvents and caused structural morphing. Hence, merging the fiber structure via 4D printing-based batteries for wearable electronics is another avenue with newer applications and functionalities.

Similarly, 4D printing has created self-folding origami-inspired fuel cells that can change shapes and sizes to maximize energy output. These fuel cells are made of a smart material that can respond to changes in temperature or pH and can be printed with complex geometries that would be difficult to achieve with traditional manufacturing methods. Goel et al. reported that the inkjet printed a portable microbial fuel cell as an origami array (Figure 15g_1–g_4).[218] A tabletop PCB inkjet printer was used to customize the electrode design, and the node was further modified with synthesized MnO_2 NPs before the entire cell was formed by folding the paper along predefined edges. Figure 15g_5–g_8 shows the different iterations of bioelectrode materials (e.g., carbon and MnO_2) to determine the morphological and structural optimization. The higher the MnO_2 loading, the higher the performance reaching a maximum power density of 15.9 μW cm^{-2} and current density of 130 μA cm^{-2} at an open-circuit potential for two connected MFCs of 0.534 V.[218] Such a 4D printing-enabled origami array was from simple electrode manufacturing and modification, showing potential in energy management, data monitoring, and Internet-of-Things. Additionally, 4D printing electrolytes can selectively create a pathway to a specific ion leading to faster charge and discharge cycles for electrode additives to serve as insulators or promote higher ionic conductivity. 4D printing is built upon 3D printing by virtue, and therefore one must thoroughly scrutinize the 3D printing capabilities while promoting 4D printing. First, the design of 4D LIBs with flexible shapes will need to fit the surface of many desirable targets, one of the most significant features of flexible/stretchable devices compared with their rigid counterparts. Second, new materials and device structures must be created for enhanced energy/power density to balance processing costs and feasibility. Overall, 4D printing has the potential to revolutionize ESS, enabling new functionalities and capabilities impossible in conventional manufacturing.

5.7. Explore beyond Lithium-Ion Batteries in Additive Manufacturing

Our focus on lithium-relevant batteries (e.g., lithium-ion, lithium-sulfur, and lithium-solid state batteries) in this review served as an illustrative example to elucidate the significance of 3D printing and related manufacturing techniques in the battery domain. However, we recognize that designing, processing, and utilizing lithium-ion batteries present their own set of challenges and limitations. The development of sodium-ion batteries, zinc-ion batteries, metal batteries, flow batteries, and other alternative battery technologies in recent years has been rapid. These emerging battery systems face distinct challenges and problems that set them apart from lithium-relevant batteries. The following lists some of the key challenges associated with these alternative battery technologies.

The first challenge is the low electrochemical performance. Sodium-ion, zinc-ion, metal, flow, and other batteries often exhibit lower energy density and specific capacity than lithium-ion batteries. Achieving comparable or superior electrochemical performance, including capacity, cycling stability, and rate capability is a significant challenge for these alternative systems. On the other hand, Li's availability is limited and its extraction is challenging as compared to Na, Zn, and certain metals used in alternative batteries. Still, sodium ions and zinc ions are larger than lithium ions, resulting in lower mobility within the electrode materials and electrolytes. Furthermore, the depletion of oxygen and subsequent exposure frequently pose challenges, resulting in oxidation and decreased efficiency for battery performance. Overcoming these limitations to achieve efficient ionic conductivity and diffusion is a critical aspect of enhancing the performance of these battery systems.

As discussed in the electrode materials and their design in Sections 5.1 to 5.3, developing suitable electrode materials that exhibit good electrochemical activity, stability, and compatibility with the specific chemistry of sodium-ion, zinc-ion, metal, and flow batteries is a challenge. Designing and synthesizing materials with high capacity, long cycle life, and good electrochemical reversibility remains an active area of research and development. Besides, the selection and optimization of electrolyte compositions for alternative battery systems can be challenging. Finding electrolyte formulations in the design phase that offer high ionic conductivity, good compatibility with electrode

3D printed bilayer composed of two engineered *S. boulardii* mutants with the top layer printed as stripes and the bottom layer as a flat sheet, showing the normal bending and Gaussian curvature upon growth for biomedical and biological applications. Reproduced with permission.[214] Copyright 2022, Wiley-VCH. d_1–d_4) Infrared-triggered thermoplastic polyurethane (TPU)/carbon nanotubes (CNT) shape memory hands with the ability to fully recover for motion control and sensing/actuating purposes. d_5–d_8) The ability to print a dual-motor triggered alarm system, where (d_6) is the circuit diagram while (d_7) shows a green light for indicating a safe state as opposed to (d_8). Reproduced with permission.[215] Copyright 2022, Wiley-VCH. e_1,e_2) 3D printed carbon fibers, such as CNTs used in the cathode (LFP) fiber and anode (LTO) fiber-based materials for textile batteries. Reproduced with permission.[216] Copyright 2017, Wiley-VCH. f_1,f_2) 4D printing of crystalline fibers with photocurable polymers and fumed silica as fiber-reinforced composites via DIW and stimulated through the heat to create shape-shifting structures. Reproduced with permission.[217] Copyright 2021, American Chemical Society. g_1–g_4) The schematic representation of the folded structures and the final origami-array structure. g_5–g_8) 4D printed via inkjet to fabricate a portable microbial fuel cell as an origami array using custom carbon cathodes and transition metal oxide MnO_2 nanomaterial. Reproduced with permission.[218] Copyright 2021, Elsevier.

materials, and long-term stability is crucial for achieving optimal battery performance and safety. At the same time, all battery systems experience some level of degradation over time, impacting their cycle life and overall performance. Issues such as electrode/electrolyte degradation, side reactions, and the formation of passivating layers can affect the stability and longevity of these batteries. As a result, the safety of alternative battery technologies is a significant concern due to their diminishing properties over time and the potential for accidents. Addressing challenges like dendrite formation,[219,220] which can cause short circuits and thermal runaway,[221] is crucial for improving the safety of sodium-ion batteries, zinc-ion batteries, metal-based, and flow batteries.

More importantly, developing scalable and cost-effective manufacturing processes for alternative battery systems is a challenge. Transitioning from laboratory-scale demonstrations to mass production while maintaining consistent performance and quality requires overcoming various technical and logistical hurdles. Therefore, the application of 3D printing technology in these alternative battery systems has proven instrumental in addressing specific problems and driving notable advancements.

First, 3D printing enables rapid prototyping and iterative design iterations, reducing development time and costs. This capability promotes faster innovation cycles, facilitating the exploration and optimization of novel materials, electrode geometries, and electrolyte formulations for sodium-ion batteries, zinc-ion batteries, metal-based batteries, and flow batteries. Second, 3D printing enables the fabrication of complex and intricate structures with high precision. This capability allows for the customization of battery components and the design of optimized architectures, leading to enhanced performance and unique characteristics[222-224] in sodium-ion, zinc-ion, metal, and flow batteries. Third, 3D printing facilitates the integration of various battery components into compact and space-efficient designs. This is particularly valuable in applications where size and weight constraints are critical, such as wearable devices or miniaturized electronics, expanding the battery applications. Fourth, facilitated by structural design and data analytics, 3D printing techniques can be employed to create well-defined electrode structures with tailored properties, such as specific porosity, surface area, and hierarchical architectures.[225-227] This level of control aids in optimizing electrochemical performance, including capacity, cycling stability, and rate capability.[10] Fifth, 3D printing techniques accommodate a wide range of materials, including advanced electrode materials and novel electrolyte formulations. This capability expands the material options for alternative battery systems and allows for the exploration of new compositions and combinations, ultimately contributing to the development of more efficient and sustainable energy storage technologies.[228,229] Last but not least, 3D printing controls processing parameters with high autonomy and achieves consistent performance characteristics, such as capacity, voltage, and cycle life.[230]

By leveraging 3D printing technology in the context of sodium-ion batteries, zinc-ion batteries, metal batteries, flow batteries, and related systems, researchers and engineers have made significant strides in addressing specific challenges, improving performance parameters, and advancing the state-of-the-art in alternative battery technologies. Considering more abundant and cost-efficient metals (e.g., potassium-ion,[231,232] magnesium-ion,[233,234] and aluminum-ion[235,236] batteries) and a lack of their applications in advanced manufacturing, the continued exploration and integration of 3D printing techniques hold great promise for further advancements and the realization of practical applications in the field of energy storage.

5.8. Leverage Advanced Computer Technology in 3D Printable Batteries

The transformation and upgrading of 3D-printed batteries through advanced computer technology offer significant potential for enhancing the entire battery lifecycle, including design, manufacturing, and recycling. Here's how advanced computer technology can be leveraged in each stage.

During the design stage, computational modeling and simulations can aid in the design and optimization of battery materials (cathode,[237-239] anode,[240] and SSE.[241-243]). It allows for exploring various material compositions, structures, and properties to improve performance characteristics, such as energy density, stability, and conductivity. For example, First-principle methods, such as density functional theory (DFT), enable the calculation of electronic structure and properties of materials from fundamental physical principles.[244] They can provide insights into the atomic-level behavior of battery materials, including their electronic structure, stability, and reaction mechanisms. Molecular dynamics (MD) simulations simulate the motion and interactions of atoms and molecules over time. They can provide information about the behavior and dynamics of materials at the atomic scale.[245] MD simulations are often used to study diffusion processes, phase transitions, and ion transport in battery materials. The finite element method (FEM) is a numerical technique for solving partial differential equations by dividing the domain into smaller elements.[246] In the context of battery materials, FEM can be used to model and optimize the electrochemical processes, heat transfer, and stress distribution within battery electrodes and cells. It aids in predicting performance characteristics and optimizing designs for improved efficiency and durability. The boundary element method (BEM) is a numerical method used to solve boundary value problems by discretizing the boundaries instead of the entire domain.[247] BEM can be employed in battery design to model the electrostatic potential distribution and electric fields within the battery system. It helps analyze the behavior of ions, charge distribution, and electrochemical reactions at the electrode-electrolyte interfaces. Multi-scale modeling integrates different modeling techniques, such as atomistic simulations (e.g., DFT, MD) and continuum models (e.g., FEM), to capture phenomena occurring at multiple lengths and time scales. It enables studying complex interactions between atomic, mesoscale, and macroscopic behavior in battery materials, offering a more comprehensive understanding of their performance and optimizing their properties. Besides, computer-aided design (CAD) software (e.g., SolidWorks) enables the creation and optimization of battery structures, including electrodes and cell configurations.[248] It allows for precise control over the internal geometry and arrangement of components, optimizing factors of packing density, surface area, and electrolyte distribution.

During the manufacturing stage, advanced computer technology, coupled with additive manufacturing software (e.g., slicing for additive layer control and multi-axis autonomy for structural variability), can facilitate the precise fabrication of electrodes and solid electrolytes. Computer-controlled printing processes enable the deposition of active materials in complex geometries, enhancing electrode performance and enabling the creation of custom electrode designs tailored to specific applications. More importantly, computer-guided assembly techniques, such as robotic automation, can streamline the manufacturing process of battery devices and battery performance. Automated systems can accurately position and connect components, ensuring consistency and reducing human error. As relevant, Section 5.4 described the role of data analytics during the material processing and assembly/disassembly procedures. For example, process optimization tools can help better manufacturing parameters, e.g., viscosity, shear rates, electrode mass loading, electrode thickness, and porosity. These tools include Reinforcement Learning (RL), Bayesian Optimization, Particle Swarm Optimization (PSO), and NeuroEvolution of Augmenting Topologies (NEAT), which are highly dependent upon advanced computational capabilities.[249,250]

During the lifecycle analysis stage, advanced computer technology (e.g., ANSYS Granta Edupack) can aid in conducting lifecycle assessments to evaluate the environmental impact of battery designs and manufacturing processes.[251,252] It enables the identification of opportunities for optimization, resource efficiency, and reduced waste generation. More importantly, computer-based sorting and separation techniques can be employed to recover valuable materials from spent batteries during recycling. Computer vision (e.g., convolutional neural networks (CNN), Object Detection algorithms (e.g., YOLO, SSD), Image Classification models (e.g., ResNet, Inception)), robotic systems (e.g., robotic arms, Gantry systems, Delta robotics, automated conveyor systems), and data analytics (e.g., machine learning, deep learning, artificial intelligence) as mentioned above, can assist in the identification, classification, and sorting of battery components and materials for efficient recovery and recycling.[253,254] For example, image analysis and computer vision tools, including OpenCV (Open Source Computer Vision Library), TensorFlow, PyTorch, MATLAB, Caffe, and scikit-image as a Python library for image processing and analysis, can assist with battery recycling in pyrometallurgical, hydrometallurgical, and biological recycling methods.

Overall, advanced computer technology plays a crucial role in advancing the transformation and upgrading of traditional 3D-printed batteries. It enables the exploration of novel materials and structures, enhances manufacturing precision and efficiency, and supports environmentally sustainable practices throughout the battery lifecycle. By leveraging computational tools and automation, the battery industry can achieve more remarkable performance, customization, and sustainability in battery design, production, and recycling processes.

5.9. Challenges and Opportunities in 3D Printable Batteries

While 3D printing offers several advantages in battery manufacturing, it also has some drawbacks to be addressed. Here are a few challenges and potential technological developments to overcome them:

Energy Density Limitations: 3D printing techniques, such as direct ink writing or powder-based processes, may have limitations in achieving high-energy-density batteries. Traditional winding processes used in battery manufacturing allow for tightly packed electrode structures, which can optimize energy density. To overcome this limitation, advancements in 3D printing technologies are required to enable precise control over the microstructure and porosity of printed electrodes. This could involve the development of new printing methods or optimized material formulations specifically designed for higher energy density, as we discussed in Section 5.2.

Post-processing Limitations: Coated electrodes, commonly used in conventional battery manufacturing, offer ease of handling and integration into battery cell designs. In contrast, 3D-printed electrodes may have complexities in terms of post-processing, assembly, and integration. Technological advancements should focus on developing efficient and automated post-processing methods, such as electrode surface treatment, stacking, and interconnection techniques, on ensuring the convenience and seamless integration of 3D-printed electrodes into battery cells, as we described in Sections 5.2 and 5.3.

Material Selection and Performance Limitations: The choice of suitable materials for 3D printing in battery manufacturing is crucial. While various printable materials are available, finding materials that exhibit high electrochemical performance, stability, and compatibility with 3D printing processes can be challenging. The development of new printable materials specifically designed for high-performance batteries is an ongoing area of research. This includes exploring novel electrode materials, electrolytes, and additives that can be successfully utilized in 3D printing processes while maintaining excellent battery performance. This content can be found in Sections 5.1 and 5.7.

Production Scalability and Processing Resolution Limitations: 3D printing, particularly for large-scale battery production, may face challenges in terms of scalability and production efficiency in the short term. Traditional manufacturing methods can achieve higher production rates and economies of scale. To address this, technological advancements are needed to enhance the speed and throughput of AM without compromising the processing quality and printing accuracy of the printed battery components. Specific approaches may help mitigate the scalability-resolution trade-off, including but not limited to multi-scale printing, hybrid manufacturing, advanced process control, iterative optimization, and new material innovation. This could involve innovations in printer design, multi-head printing systems, or novel fabrication strategies to increase productivity while not sacrificing manufacturing precision, as we have relevant content in Sections 5.1–5.3 and 5.6,5.7.

Integration of Multi-Material Component Limitations: Battery cells often comprise multiple components, such as electrodes, current collectors, separators, and electrolytes. Ensuring seamless integration of these components in 3D-printed batteries can be a complex task. Future developments should focus on advancing multi-material 3D printing techniques that enable the simultaneous printing of multiple materials with different properties. This would facilitate the direct printing of fully integrated battery cells, eliminating the need for additional assembly steps. We

have summarized the state of the art in Sections 2–4. Overall, technological advancements in 3D printing processes, printable materials, post-processing techniques, and integration methods are essential to overcome the drawbacks associated with battery manufacturing using 3D printing. Ongoing research and development efforts should be focused on addressing these challenges to unlock the full potential of 3D printing in the battery industry.

In summary, 3D printing technologies have emerged as a game-changing approach to enhance devices in the EES sector, enabling the fabrication of wearables, miniaturized micro-robots, medical devices, and micro-electronic storage devices with intricate designs. Moreover, the use of ceramics and composite materials in 3D printing has revolutionized the manufacturing process, offering unprecedented complexity and simplification. As this technology continues to advance, the possibilities of creating new materials, achieving ultrafine spatial resolution, data prediction, and stimuli-responsive 3D printed materials are becoming more feasible. Consequently, 3D printing is poised to become one of the most promising manufacturing methods for the next generation of EES systems.

Acknowledgements

The authors appreciate the funding from NSF Graduate Research Fellowships Program (GRFP # 1000343766), Qatar National Research Fund (Grant # NPRP14S-0317-210064), the NSF Faculty Early Career Development Program (CAREER) award (# 2145895), ACS PRF (award #62371-ND10), Arizona Biomedical Research Center (award # RFGA2022-010-07), and BSF (award #2020102).

Conflict of Interest

The authors declare no conflict of interest.

Keywords

3D printing, batteries, electrodes, hierarchies, multimaterials, solid electrolytes

Received: March 31, 2023
Revised: July 8, 2023
Published online: July 27, 2023

[1] K. H. Choi, D. B. Ahn, S. Y. Lee, *ACS Energy Lett.* **2018**, *3*, 220.
[2] Z. Lyu, G. J. H. Lim, J. J. Koh, Y. Li, Y. Ma, J. Ding, J. Wang, Z. Hu, J. Wang, W. Chen, Y. Chen, *Joule* **2021**, *5*, 89.
[3] M. P. Browne, E. Redondo, M. Pumera, *Chem. Rev.* **2020**, *120*, 2783.
[4] Y. Zhu, J. Qin, G. Shi, C. Sun, M. Ingram, S. Qian, J. Lu, S. Zhang, Y. L. Zhong, *Carbon Energy* **2022**, *4*, 1242.
[5] M. Idrees, S. Batool, M. A. U. Din, M. S. Javed, S. Ahmed, Z. Chen, *Nano Energy* **2023**, *109*, 108247.
[6] P. Chang, H. Mei, S. Zhou, K. G. Dassios, L. Cheng, *J. Mater. Chem. A* **2019**, *7*, 4230.
[7] J. C. Ruiz-Morales, A. Tarancó, J. Canales-Vá zquez, J. Mé ndez-Ramos, L. Herná ndez-Afonso, P. Acosta-Mora, J. R. Marí Rueda, R. Ferná ndez-Gonzá lez, *Energy Environ. Sci.* **2017**, *10*, 846.
[8] T. Chu, S. Park, K. Fu, K. Correspondence, *Carbon Energy* **2021**, *3*, 424.
[9] M. Pei, H. Shi, F. Yao, S. Liang, Z. Xu, X. Pei, S. Wang, Y. Hu, *J. Mater. Chem. A* **2021**, *9*, 25237.
[10] Y. Pang, Y. Cao, Y. Chu, M. Liu, K. Snyder, D. MacKenzie, C. Cao, *Adv. Funct. Mater.* **2020**, *30*, 1906244.
[11] V. Egorov, U. Gulzar, Y. Zhang, S. Breen, C. O'Dwyer, *Adv. Mater.* **2020**, *32*, 2000556.
[12] M. Zhang, H. Mei, P. Chang, L. Cheng, *J. Mater. Chem. A* **2020**, *8*, 10670.
[13] Y. Han, Y. You, C. Hou, Y. Xiong, Y. Lin, Q. Xue, G. Kaur, B. D. Gates, Z. Chen, W. Zhang, Z. Yang, *Nanotechnology* **2019**, *31*, 012001.
[14] S. J. Dillon, K. Sun, *Curr. Opin. Solid State Mater. Sci.* **2012**, *16*, 153.
[15] P. Zheng, J. Sun, H. Liu, R. Wang, C. Liu, Y. Zhao, J. Li, Y. Zheng, X. Rui, *Batteries Supercaps* **2023**, *6*, 202200481.
[16] Y. Zhu, J. Qin, G. Shi, C. Sun, M. Ingram, S. Qian, J. Lu, S. Zhang, Y. Lin Zhong, *Carbon Energy* **2022**, *4*, 1242.
[17] X. Gao, M. Zheng, X. Yang, R. Sun, J. Zhang, X. Sun, *Mater. Today* **2022**, *59*, 161.
[18] Y. Lu, C. Z. Zhao, H. Yuan, J. K. Hu, J. Q. Huang, Q. Zhang, *Matter* **2022**, *5*, 876.
[19] K. Fu, Y. Yao, J. Dai, L. Hu, *Adv. Mater.* **2017**, *29*, 1603486.
[20] X. Tian, B. Xu, *Small Methods* **2021**, *5*, 2100877.
[21] T. Zhang, F. Ran, *Adv. Funct. Mater.* **2021**, *31*, 2010041.
[22] X. Li, H. Jiang, Y. Liu, X. Guo, G. He, Z. Chu, G. Yu, M. Science, E. Program, *EcoMat* **2022**, *4*, e12162.
[23] X. Tian, J. Jin, S. Yuan, C. K. Chua, S. B. Tor, K. Zhou, *Adv. Energy Mater.* **2017**, *7*, 1700127.
[24] O. C. Esan, X. Shi, Z. Pan, X. Huo, L. An, T. S. Zhao, *Adv. Energy Mater.* **2020**, *10*, 2000758.
[25] S. Abada, G. Marlair, A. Lecocq, M. Petit, V. Sauvant-Moynot, F. Huet, *J. Power Sources* **2016**, *306*, 178.
[26] H. Lu, J. Wang, J. Yang, J. Zou, Q.-K. Wang, J.-N. Shen, Y.-J. He, Z.-F. Ma, *Chin. Phys. B* **2020**, *29*, 068201.
[27] Z. Wang, H. Jiang, Y. Zhang, Y. An, C. Wei, L. Tan, S. Xiong, Y. Qian, J. Feng, *Adv. Funct. Mater.* **2023**, *33*, 2210184.
[28] J. T. Frith, M. J. Lacey, U. Ulissi, *Nat. Commun.* **2023**, *14*, 420.
[29] S. Zhou, I. Usman, Y. Wang, A. Pan, *Energy Storage Mater.* **2021**, *38*, 141.
[30] C. M. Costa, R. Gonçalves, S. Lanceros-Méndez, *Energy Storage Mater.* **2020**, *28*, 216.
[31] C. Y. Lee, A. C. Taylor, A. Nattestad, S. Beirne, G. G. Wallace, *Joule* **2019**, *3*, 1835.
[32] J. C. Ruiz-Morales, A. Tarancón, J. Canales-Vázquez, J. Méndez-Ramos, L. Hernández-Afonso, P. Acosta-Mora, J. R. Marín Rueda, R. Fernández-González, *Energy Environ. Sci.* **2017**, *10*, 846.
[33] J. Huang, Q. Qin, J. Wang, *Processes* **2020**, *8*, 1138.
[34] S. Zakeri, M. Vippola, E. Levänen, *Addit. Manuf.* **2020**, *35*, 101177.
[35] L. J. Hornbeck, in *LEOS Summer Topical Meeting*, IEEE, Piscataway, NJ **1996**, pp. 7–8.
[36] X. Peng, X. Kuang, D. J. Roach, Y. Wang, C. M. Hamel, C. Lu, H. J. Qi, *Addit. Manuf.* **2021**, *40*, 101911.
[37] H. X. Nguyen, H. Suen, B. Poudel, P. Kwon, H. Chung, *CIRP Ann.* **2020**, *69*, 177.
[38] R. Chaudhary, P. Fabbri, E. Leoni, F. Mazzanti, R. Akbari, C. Antonini, *Prog. Addit. Manuf.* **2022**, *8*, 331.
[39] Y. Zhang, L. Wu, M. Zou, L. Zhang, Y. Song, *Adv. Mater.* **2022**, *34*, 2107249.
[40] J. R. Tumbleston, D. Shirvanyants, N. Ermoshkin, R. Janusziewicz, A. R. Johnson, D. Kelly, K. Chen, R. Pinschmidt, J. P. Rolland, A. Ermoshkin, E. T. Samulski, J. M. DeSimone, *Science* **2015**, *347*, 1349.
[41] B. Huang, Y. Zhou, L. Wei, R. Hu, X. Zhang, P. Coates, F. Sefat, W. Zhang, C. Lu, *Ind. Eng. Chem. Res.* **2022**, *61*, 13052.
[42] T. R. Yeazel-Klein, A. G. Davis, M. L. Becker, *Adv. Mater. Technol.* **2023**, *8*, 2201904.

[43] G. Lipkowitz, T. Samuelsen, K. Hsiao, B. Lee, M. T. Dulay, I. Coates, H. Lin, W. Pan, G. Toth, L. Tate, E. S. G. Shaqfeh, J. M. DeSimone, *Sci. Adv.* **2022**, *8*, 3917.
[44] B. J. Lee, K. Hsiao, G. Lipkowitz, T. Samuelsen, L. Tate, J. M. DeSimone, *Addit. Manuf.* **2022**, *55*, 102800.
[45] Z. Huang, G. Shao, L. Li, *Prog. Mater. Sci.* **2023**, *131*, 101020.
[46] B. E. Kelly, I. Bhattacharya, H. Heidari, M. Shusteff, C. M. Spadaccini, H. K. Taylor, *Science* **2019**, *363*, 1075.
[47] Q. Geng, D. Wang, P. Chen, S. C. Chen, *Nat. Commun.* **2019**, *10*, 2179.
[48] J. W. Choi, H. C. Kim, R. Wicker, *J. Mater. Process. Technol.* **2011**, *211*, 318.
[49] J. T. Toombs, M. Luitz, C. C. Cook, S. Jenne, C. C. Li, B. E. Rapp, F. Kotz-Helmer, H. K. Taylor, *Science* **2022**, *376*, 308.
[50] B. M. Schmitt, C. F. Zirbes, C. Bonin, D. Lohmann, D. C. Lencina, A. da Costa Sabino Netto, *Mater. Res.* **2018**, *20*, 883.
[51] M. Ratiu, M. A. Prichici, D. M. Anton, D. C. Negrau, *IOP Conf. Ser. Mater. Sci. Eng.* **2021**, *1169*, 012008.
[52] W. Xu, S. Jambhulkar, Y. Zhu, D. Ravichandran, M. Kakarla, B. Vernon, D. G. Lott, J. L. Cornella, O. Shefi, G. Miquelard-Garnier, Y. Yang, K. Song, *Composites, Part B* **2021**, *223*, 109102.
[53] M. A. S. R. Saadi, A. Maguire, N. T. Pottackal, M. S. H. Thakur, M. M. Ikram, A. J. Hart, P. M. Ajayan, M. M. Rahman, *Adv. Mater.* **2022**, *34*, 2108855.
[54] S. Tagliaferri, A. Panagiotopoulos, C. Mattevi, *Mater. Adv.* **2021**, *2*, 540.
[55] L. del-Mazo-Barbara, M. P. Ginebra, *J. Eur. Ceram. Soc.* **2021**, *41*, 18.
[56] A. Mazzoli, *Med. Biol. Eng. Comput.* **2013**, *51*, 245.
[57] C. Yan, Y. Shi, L. Hao, *Int. Polym. Process.* **2011**, *26*, 416.
[58] D. Drummer, S. Greiner, M. Zhao, K. Wudy, *Addit. Manuf.* **2019**, *27*, 379.
[59] D. Drummer, D. Rietzel, F. Kühnlein, *Phys. Procedia* **2010**, *5*, 533.
[60] N. K. Roy, D. Behera, O. G. Dibua, C. S. Foong, M. A. Cullinan, *Microsyst. Nanoeng.* **2019**, *5*, 64.
[61] J. P. Kruth, P. Mercelis, J. van Vaerenbergh, L. Froyen, M. Rombouts, *Rapid Prototyping J.* **2005**, *11*, 26.
[62] B. Nagarajan, Z. Hu, X. Song, W. Zhai, J. Wei, *Engineering* **2019**, *5*, 702.
[63] G. Z. Cheng, R. S. J. Estepar, E. Folch, J. Onieva, S. Gangadharan, A. Majid, *Chest* **2016**, *149*, 1136.
[64] H. N. Chia, B. M. Wu, *J. Biol. Eng.* **2015**, *9*, 4.
[65] J. Wang, Y. Liu, Z. Fan, W. Wang, B. Wang, Z. Guo, *Adv. Compos. Hybrid Mater.* **2019**, *2*, 1.
[66] I. Gibson, D. Rosen, B. Stucker, M. Khorasani, in *Additive Manufacturing Technologies* (Eds: I. Gibson, D. Rosen, B. Strucker, M. Khorasani), Springer, Cham, Switerzerland **2021**, pp. 237–252.
[67] P. Shakor, S. H. Chu, A. Puzatova, E. Dini, *Prog. Addit. Manuf.* **2022**, *7*, 643.
[68] M. Ziaee, N. B. Crane, *Addit. Manuf.* **2019**, *28*, 781.
[69] V. Popov, A. Fleisher, G. Muller-Kamskii, A. Shishkin, A. Katz-Demyanetz, N. Travitzky, S. Goel, *Sci. Rep.* **2021**, *11*, 2438.
[70] H. Sun, J. Zhu, D. Baumann, L. Peng, Y. Xu, I. Shakir, Y. Huang, X. Duan, *Nat. Rev. Mater.* **2018**, *4*, 45.
[71] C. Liu, Y. Qiu, Y. Liu, K. Xu, N. Zhao, C. Lao, J. Shen, Z. Chen, *J. Adv. Ceram.* **2022**, *11*, 295.
[72] E. Cohen, S. Menkin, M. Lifshits, Y. Kamir, A. Gladkich, G. Kosa, D. Golodnitsky, *Electrochim. Acta* **2018**, *265*, 690.
[73] G. Qi, H. Yao, Y. Zeng, J. Chen, *J. Alloys Compd.* **2023**, *935*, 167941.
[74] H. Ning, J. H. Pikul, R. Zhang, X. Li, S. Xu, J. Wang, J. A. Rogers, W. P. King, P. V. Braun, *Proc. Natl. Acad. Sci. USA* **2015**, *112*, 6573.
[75] B. Wu, B. Guo, Y. Chen, Y. Mu, H. Qu, M. Lin, J. Bai, T. Zhao, L. Zeng, *Energy Storage Mater.* **2023**, *54*, 75.
[76] H. Ragones, S. Menkin, Y. Kamir, A. Gladkikh, T. Mukra, G. Kosa, D. Golodnitsky, *Sustainable Energy Fuels* **2018**, *2*, 1542.
[77] C. Reyes, R. Somogyi, S. Niu, M. A. Cruz, F. Yang, M. J. Catenacci, C. P. Rhodes, B. J. Wiley, *ACS Appl. Energy Mater.* **2018**, *1*, 5268.
[78] A. Maurel, M. Courty, B. Fleutot, H. Tortajada, K. Prashantha, M. Armand, S. Grugeon, S. Panier, L. Dupont, *Chem. Mater.* **2018**, *30*, 7484.
[79] C. W. Foster, G. Q. Zou, Y. Jiang, M. P. Down, C. M. Liauw, A. Garcia-Miranda Ferrari, X. Ji, G. C. Smith, P. J. Kelly, C. E. Banks, *Batteries Supercaps* **2019**, *2*, 448.
[80] C. W. Foster, M. P. Down, Y. Zhang, X. Ji, S. J. Rowley-Neale, G. C. Smith, P. J. Kelly, C. E. Banks, *Sci. Rep.* **2017**, *7*, 42233.
[81] K. Fu, Y. Wang, C. Yan, Y. Yao, Y. Chen, J. Dai, S. Lacey, Y. Wang, J. Wan, T. Li, Z. Wang, Y. Xu, L. Hu, *Adv. Mater.* **2016**, *28*, 2587.
[82] C. Sun, S. Liu, X. Shi, C. Lai, J. Liang, Y. Chen, *Chem. Eng. J.* **2020**, *381*, 122641.
[83] T.-S. Wei, B. Yeop Ahn, J. Grotto, J. A. Lewis, *Adv. Mater.* **2018**, *30*, 1703027.
[84] C. Liu, F. Xu, Y. Liu, J. Ma, P. Liu, D. Wang, C. Lao, Z. Chen, *Electrochim. Acta* **2019**, *314*, 81.
[85] W. He, C. Chen, J. Jiang, Z. Chen, H. Liao, H. Dou, X. Zhang, *Batteries Supercaps* **2022**, *5*, 202100258.
[86] J. Sha, Y. Li, R. Villegas Salvatierra, T. Wang, P. Dong, Y. Ji, S. K. Lee, C. Zhang, J. Zhang, R. H. Smith, P. M. Ajayan, J. Lou, N. Zhao, J. M. Tour, *ACS Nano* **2017**, *11*, 6860.
[87] Y. T. Chen, F. Y. Hung, T. S. Lui, J. Z. Hong, *Mater. Trans.* **2017**, *58*, 525.
[88] S. Guo, J. Li, L. Zhang, Y. Li, *Mater. Lett.* **2023**, *330*, 133300.
[89] S. Lawes, Q. Sun, A. Lushington, B. Xiao, Y. Liu, X. Sun, *Nano Energy* **2017**, *36*, 313.
[90] A. Kushwaha, M. K. Jangid, B. B. Bhatt, A. Mukhopadhyay, D. Gupta, *ACS Appl. Energy Mater.* **2021**, *4*, 7911.
[91] T. Chen, Y. Wang, Y. Yang, F. Huang, M. Zhu, B. T. W. Ang, J. M. Xue, *Adv. Funct. Mater.* **2021**, *31*, 2101607.
[92] A. Azhari, E. Marzbanrad, D. Yilman, E. Toyserkani, M. A. Pope, *Carbon* **2017**, *119*, 257.
[93] J. Sha, R. V. Salvatierra, P. Dong, Y. Li, S. K. Lee, T. Wang, C. Zhang, J. Zhang, Y. Ji, P. M. Ajayan, J. Lou, N. Zhao, J. M. Tour, *ACS Appl. Mater. Interfaces* **2017**, *9*, 7376.
[94] A. Maurel, S. Grugeon, B. Fleutot, M. Courty, K. Prashantha, H. Tortajada, M. Armand, S. Panier, L. Dupont, *Sci. Rep.* **2019**, *9*, 18031.
[95] X. Gao, X. Yang, S. Wang, Q. Sun, C. Zhao, X. Li, J. Liang, M. Zheng, Y. Zhao, J. Wang, M. Li, R. Li, T. K. Sham, X. Sun, *J. Mater. Chem. A* **2019**, *8*, 278.
[96] P. Bao, Y. Lu, P. Tao, B. Liu, J. Li, X. Cui, *Ionics* **2021**, *27*, 2857.
[97] J. Hu, Y. Jiang, S. Cui, Y. Duan, T. Liu, H. Guo, L. Lin, Y. Lin, J. Zheng, K. Amine, F. Pan, *Adv. Energy Mater.* **2016**, *6*, 1600856.
[98] K. A. Acord, A. D. Dupuy, U. Scipioni Bertoli, B. Zheng, W. C. West, Q. N. Chen, A. A. Shapiro, J. M. Schoenung, *J. Mater. Process. Technol.* **2021**, *288*, 116827.
[99] Z. Shu, E. Beckert, R. Eberhardt, A. Tünnermann, *J. Mater. Chem. C* **2017**, *5*, 11590.
[100] Y. Gu, A. Wu, H. Sohn, C. Nicoletti, Z. Iqbal, J. F. Federici, *J. Manuf. Process.* **2015**, *20*, 198.
[101] F. Xu, T. Wang, W. Li, Z. Jiang, *Chem. Phys. Lett.* **2003**, *375*, 247.
[102] R. Rodriguez, L. J. Deiner, B. H. Tsao, J. P. Fellner, *ACS Appl. Energy Mater.* **2021**, *4*, 9507.
[103] L. J. Deiner, T. Jenkins, A. Powell, T. Howell, M. Rottmayer, *Adv. Eng. Mater.* **2019**, *21*, 1801281.
[104] C. Ke Sun, T.-S. Wei, B. Yeop Ahn, J. Yoon Seo, S. J. Dillon, J. A. Lewis, *Adv. Mater.* **2013**, *25*, 4539.
[105] S. Zekoll, C. Marriner-Edwards, A. K. O. Hekselman, J. Kasemchainan, C. Kuss, D. E. J. Armstrong, D. Cai, R. J. Wallace, F. H. Richter, J. H. J. Thijssen, P. G. Bruce, *Energy Environ. Sci.* **2018**, *11*, 185.

[106] D. W. McOwen, S. Xu, Y. Gong, Y. Wen, G. L. Godbey, J. E. Gritton, T. R. Hamann, J. Dai, G. T. Hitz, L. Hu, E. D. Wachsman, *Adv. Mater.* **2018**, *30*, 1707132.
[107] Q. Chen, R. Xu, Z. He, K. Zhao, L. Pan, *J. Electrochem. Soc.* **2017**, *164*, A1852.
[108] Y. He, S. Chen, L. Nie, Z. Sun, X. Wu, W. Liu, *Nano Lett.* **2020**, *20*, 7136.
[109] K. Lee, Y. Shang, V. A. Bobrin, R. Kuchel, D. Kundu, N. Corrigan, C. Boyer, *Adv. Mater.* **2022**, *34*, 2204816.
[110] D. Melodia, A. Bhadra, K. Lee, R. Kuchel, D. Kundu, N. Corrigan, C. Boyer, *Small* **2023**, *12*, 2206639.
[111] A. Maurel, M. Armand, S. Grugeon, B. Fleutot, C. Davoisne, H. Tortajada, M. Courty, S. Panier, L. Dupont, *J. Electrochem. Soc.* **2020**, *167*, 070536.
[112] A. Vinegrad, H. Ragones, N. Jayakody, G. Ardel, M. Goor, Y. Kamir, M. M. Dorfman, A. Gladkikh, L. Burstein, Y. Horowitz, S. Greenbaum, D. Golodnitsky, *J. Electrochem. Soc.* **2021**, *168*, 110549.
[113] H. Rupp, R. Bhandary, A. Kulkarni, W. Binder, *Adv. Mater. Technol.* **2022**, *7*, 2200088.
[114] J. Bae, S. Oh, B. Lee, C. H. Lee, J. Chung, J. Kim, S. Jo, S. Seo, J. Lim, S. Chung, *Energy Storage Mater.* **2023**, *57*, 277.
[115] P. E. Delannoy, B. Riou, B. Lestriez, D. Guyomard, T. Brousse, J. L. Bideau, *J. Power Sources* **2015**, *274*, 1085.
[116] Y. Gambe, H. Kobayashi, K. Iwase, S. Stauss, I. Honma, *Dalton Trans.* **2021**, *50*, 16504.
[117] A. J. Blake, R. R. Kohlmeyer, J. O. Hardin, E. A. Carmona, B. Maruyama, J. D. Berrigan, H. Huang, M. F. Durstock, *Adv. Energy Mater.* **2017**, *7*, 1602920.
[118] M. Cheng, Y. Jiang, W. Yao, Y. Yuan, R. Deivanayagam, T. Foroozan, Z. Huang, B. Song, R. Rojaee, T. Shokuhfar, Y. Pan, J. Lu, R. Shahbazian-Yassar, *Adv. Mater.* **2018**, *30*, 1800615.
[119] Z. Katcharava, A. Marinow, R. Bhandary, W. H. Binder, *Nanomaterials* **2022**, *12*, 1859.
[120] H. Ragones, A. Vinegrad, G. Ardel, M. Goor, Y. Kamir, M. M. Dorfman, A. Gladkikh, D. Golodnitsky, *J. Electrochem. Soc.* **2020**, *167*, 070503.
[121] L. J. Deiner, T. Jenkins, T. Howell, M. Rottmayer, *Adv. Eng. Mater.* **2019**, *21*, 1900952.
[122] R. Wei, S. Chen, T. Gao, W. Liu, *Nano Sel.* **2021**, *2*, 2256.
[123] H. Rupp, R. Bhandary, A. Kulkarni, W. Binder, *Adv. Mater. Technol.* **2022**, *7*, 2200088.
[124] P. E. Delannoy, B. Riou, B. Lestriez, D. Guyomard, T. Brousse, J. L. Bideau, *J. Power Sources* **2015**, *274*, 1085.
[125] Z. Fang, J. Wang, H. Wu, Q. Li, S. Fan, J. Wang, *J. Power Sources* **2020**, *454*, 227932.
[126] W. Xu, S. Jambhulkar, Y. Zhu, D. Ravichandran, M. Kakarla, B. Vernon, D. G. Lott, J. L. Cornella, O. Shefi, G. Miquelard-Garnier, Y. Yang, K. Song, *Composites, Part B* **2021**, *223*, 109102.
[127] J. Li, Q. Jiang, N. Yuan, J. Tang, *Materials* **2018**, *11*, 2280.
[128] T. Liu, R. Yan, H. Huang, L. Pan, X. Cao, A. deMello, M. Niederberger, *Adv. Funct. Mater.* **2020**, *30*, 2004410.
[129] Y. Yang, S. Jeong, L. Hu, H. Wu, S. W. Lee, Y. Cui, *Proc. Natl. Acad. Sci. USA* **2011**, *108*, 13013.
[130] F. S. Gittleson, D. Hwang, W. H. Ryu, S. M. Hashmi, J. Hwang, T. Goh, A. D. Taylor, *ACS Nano* **2015**, *9*, 10005.
[131] S. Oukassi, L. Baggetto, C. Dubarry, L. le Van-Jodin, S. Poncet, R. Salot, *ACS Appl. Mater. Interfaces* **2019**, *11*, 683.
[132] S. Jambhulkar, D. Ravichandran, B. Sundaravadivelan, K. Song, I. A. Fulton, *J. Mater. Chem. C* **2023**, *11*, 4333.
[133] J.-W. Choi, Y. Hwang, H. Yim, in *Fabrication of transparent all-solid-state thin film lithium ion battery*, **2022**.
[134] H. Lee, H. Yim, K. B. Kim, J. W. Choi, *J. Nanosci. Nanotechnol.* **2015**, *15*, 8627.
[135] X. Zhang, T. Liu, S. Zhang, X. Huang, B. Xu, Y. Lin, B. Xu, L. Li, C. W. Nan, Y. Shen, *J. Am. Chem. Soc.* **2017**, *139*, 13779.
[136] Y. J. Shen, M. J. Reddy, P. P. Chu, *Solid State Ionics* **2004**, *175*, 747.
[137] T. Zheng, Z. Jia, N. Lin, T. Langer, S. Lux, I. Lund, A. C. Gentschev, J. Qiao, G. Liu, *Polymers* **2017**, *9*, 657.
[138] L. Ma, D. Lu, P. Yang, X. Xi, R. Liu, D. Wu, *Electrochim. Acta* **2019**, *319*, 201.
[139] J. Wan, J. Xie, X. Kong, Z. Liu, K. Liu, F. Shi, A. Pei, H. Chen, W. Chen, J. Chen, X. Zhang, L. Zong, J. Wang, L. Q. Chen, J. Qin, Y. Cui, *Nat. Nanotechnol.* **2019**, *14*, 705.
[140] Z. Ren, Y. Liu, K. Sun, X. Zhou, N. Zhang, *Electrochim. Acta* **2009**, *54*, 1888.
[141] B. Sun, J. Mindemark, K. Edström, D. Brandell, *Solid State Ionics* **2014**, *262*, 738.
[142] J. Wu, K. Jiang, G. Li, Z. Zhao, Q. Li, F. Geng, *Adv. Funct. Mater.* **2019**, *29*, 1901576.
[143] L. Shen, Q. Dong, G. Zhu, Z. Dai, Y. Zhang, W. Wang, X. Dong, *Adv. Mater. Interfaces* **2018**, *5*, 1800362.
[144] T. Liu, M. Zhang, Y. L. Wang, Q. Y. Wang, C. Lv, K. X. Liu, S. Suresh, Y. H. Yin, Y. Y. Hu, Y. S. Li, X. Bin Liu, S. W. Zhong, B. Y. Xia, Z. P. Wu, *Adv. Energy Mater.* **2018**, *8*, 1802349.
[145] K. Zhu, Y. Luo, F. Zhao, J. Hou, X. Wang, H. Ma, H. Wu, Y. Zhang, K. Jiang, S. Fan, J. Wang, K. Liu, *ACS Sustainable Chem. Eng.* **2018**, *6*, 3426.
[146] S. Jambhulkar, W. Xu, R. Franklin, D. Ravichandran, Y. Zhu, K. Song, *J. Mater. Chem. C* **2020**, *8*, 9495.
[147] T. Jiang, F. Bu, X. Feng, I. Shakir, G. Hao, Y. Xu, *ACS Nano* **2017**, *11*, 5140.
[148] R. Mo, D. Rooney, K. Sun, H. Y. Yang, *Nat. Commun.* **2017**, *8*, 13949.
[149] W. Xi, Y. Zhang, J. Zhang, R. Wang, Y. Gong, B. He, H. Wang, J. Jin, *J. Mater. Chem. C* **2023**, *11*, 2414.
[150] K. Zhu, H. Zhang, K. Ye, W. Zhao, J. Yan, K. Cheng, G. Wang, B. Yang, D. Cao, *ChemElectroChem* **2017**, *4*, 3018.
[151] X. Zheng, H. Lee, T. H. Weisgraber, M. Shusteff, J. DeOtte, E. B. Duoss, J. D. Kuntz, M. M. Biener, Q. Ge, J. A. Jackson, S. O. Kucheyev, N. X. Fang, C. M. Spadaccini, *Science* **2014**, *344*, 1373.
[152] R. Kumar, S. K. Sarangi, in *Int. Conf. on Advances in Materials Processing & Manufacturing Applications*, Springer Science and Business Media, Deutschland GmbH, Frankfurt, Germany **2021**, pp. 531–538.
[153] W. Wu, P. Geng, G. Li, D. Zhao, H. Zhang, J. Zhao, *Materials* **2015**, *8*, 5834.
[154] J. A. Lewis, *Adv. Funct. Mater.* **2006**, *16*, 2193.
[155] G. M. Gratson, F. García-Santamaría, V. Lousse, M. Xu, S. Fan, J. A. Lewis, P. v. Braun, *Adv. Mater.* **2006**, *18*, 461.
[156] C. M. S. Vicente, M. Sardinha, L. Reis, A. Ribeiro, M. Leite, *Prog. Addit. Manuf.* **2023**, *8*, 1.
[157] A. Sharif, N. Farid, P. McGlynn, M. Wang, R. K. Vijayaraghavan, A. Jilani, G. Leen, P. J. McNally, G. M. O'Connor, *J. Phys. D: Appl. Phys.* **2023**, *56*, 075102.
[158] B. Gao, H. Zhao, L. Peng, Z. Sun, *Micromachines* **2022**, *14*, 57.
[159] P. Goldberg-Oppenheimer, D. Eder, U. Steiner, *Adv. Funct. Mater.* **2011**, *21*, 1895.
[160] I. Liashenko, J. Rosell-Llompart, A. Cabot, *Nat. Commun.* **2020**, *11*, 753.
[161] A. Maurel, A. C. Martinez, S. Grugeon, S. Panier, L. Dupont, P. Cortes, C. G. Sherrard, I. Small, S. T. Sreenivasan, E. MacDonald, *IEEE Access* **2021**, *9*, 140654.
[162] J. U. Park, M. Hardy, S. J. Kang, K. Barton, K. Adair, D. K. Mukhopadhyay, C. Y. Lee, M. S. Strano, A. G. Alleyne, J. G. Georgiadis, P. M. Ferreira, J. A. Rogers, *Nat. Mater.* **2007**, *6*, 782.
[163] S. Zekoll, C. Marriner-Edwards, A. K. O. Hekselman, J. Kasemchainan, C. Kuss, D. E. J. Armstrong, D. Cai, R. J. Wallace, F. H. Richter, J. H. J. Thijssen, P. G. Bruce, *Energy Environ. Sci.* **2018**, *11*, 185.

[164] K. Sachsenheimer, C. Richter, D. Helmer, F. Kotz, B. E. Rapp, *Micromachines* **2019**, *10*, 588.
[165] A. Yadav, B. De, S. K. Singh, P. Sinha, K. K. Kar, *ACS Appl. Mater. Interfaces* **2019**, *11*, 7974.
[166] L. Zeng, H. Xi, X. Liu, C. Zhang, *Nanomaterials* **2021**, *11*, 3454.
[167] D. Ji, H. Zheng, H. Zhang, W. Liu, J. Ding, *Chem. Eng. J.* **2022**, *433*, 133815.
[168] M. Rafiee, F. Granier, D. Therriault, *Adv. Mater. Technol.* **2021**, *6*, 2100356.
[169] D. Ravichandran, W. Xu, M. Kakarla, S. Jambhulkar, Y. Zhu, K. Song, *Addit. Manuf.* **2021**, *47*, 102322.
[170] M. A. Skylar-Scott, J. Mueller, C. W. Visser, J. A. Lewis, *Nature* **2019**, *575*, 330.
[171] A. Maurel, *Thermoplastic Composite Filaments Formulation and 3D-Printing of a Lithium-Ion Battery via Fused Deposition Modeling*, Université de Picardie Jules Verne, Amiens, France **2020**.
[172] V. L. Deringer, *J. Phys.: Condens. Matter.* **2020**, *2*, 041003.
[173] H. Ko, Y. Lu, Z. Yang, N. Y. Ndiaye, P. Witherell, *J. Manuf. Syst.* **2023**, *67*, 213.
[174] M. Mani, B. Lane, A. Donmez, S. Feng, S. Moylan, R. Fesperman, *NIST Interagency/Internal Report (NISTIR), National Institute of Standards and Technology*, Gaithersburg, MD, https://doi.org/10.6028/NIST.IR.8036 (accessed: March 2015).
[175] T. G. Spears, S. A. Gold, *Integr. Mater. Manuf. Innovation* **2016**, *5*, 16.
[176] B. Lane, H. Yeung, *J. Res. Natl. Inst. Stand. Technol.* **2021**, *125*, 125027.
[177] E. Brinksmeier, S. Reese, A. Klink, L. Langenhorst, T. Lübben, M. Meinke, D. Meyer, O. Riemer, J. Sölter, *Nanomanuf. Metrol.* **2018**, *1*, 193.
[178] V. Sandfort, K. Yan, P. J. Pickhardt, R. M. Summers, *Nature* **2019**, *9*, 16884.
[179] A. Sancarlos, M. Cameron, A. Abel, E. Cueto, J. L. Duval, F. Chinesta, *Arch. Comput. Methods Eng.* **2021**, *28*, 979.
[180] Z. Wei, Q. He, Y. Zhao, *J. Power Sources* **2022**, *549*, 232125.
[181] A. Adadi, M. Berrada, *IEEE Access* **2018**, *6*, 52138.
[182] H. Ko, P. Witherell, Y. Lu, S. Kim, D. W. Rosen, *Addit. Manuf.* **2021**, *37*, 101620.
[183] P. Xu, D. H. S. Tan, B. Jiao, H. Gao, X. Yu, Z. Chen, *Adv. Funct. Mater.* **2023**, *33*, 2213168.
[184] K. K. Jena, A. Alfantazi, A. T. Mayyas, *EnergyFuels* **2021**, *35*, 18257.
[185] Y. Huang, Z. Qin, C. Shan, Y. Xie, X. Meng, D. Qian, G. He, D. Mao, L. Wan, *J. Energy Chem.* **2023**, *80*, 492.
[186] H. Wang, S. Burke, R. Yuan, J. F. Whitacre, *J. Energy Storage* **2023**, *60*, 106616.
[187] G. Ji, J. Wang, Z. Liang, K. Jia, J. Ma, Z. Zhuang, G. Zhou, H. M. Cheng, *Nature* **2023**, *14*, 584.
[188] Y. Yang, X. Meng, H. Cao, X. Lin, C. Liu, Y. Sun, Y. Zhang, Z. Sun, *Green Chem.* **2018**, *20*, 3121.
[189] J. Zhang, J. Hu, Y. Liu, Q. Jing, C. Yang, Y. Chen, C. Wang, *ACS Sustainable Chem. Eng.* **2019**, *7*, 5626.
[190] L. X. Yuan, Z. H. Wang, W. X. Zhang, X. L. Hu, J. T. Chen, Y. H. Huang, J. B. Goodenough, *Energy Environ. Sci.* **2011**, *4*, 269.
[191] W. Lv, X. Zheng, L. Li, H. Cao, Y. Zhang, R. Chen, H. Ou, F. Kang, Z. Sun, *Front. Chem. Sci. Eng.* **2021**, *15*, 1243.
[192] Y. Li, W. Lv, H. Huang, W. Yan, X. Li, P. Ning, H. Cao, Z. Sun, *Green Chem.* **2021**, *23*, 6139.
[193] Z. Lianqi, G. Jian, Z. Enlou, CN105742743A, **2016**.
[194] S. Natarajan, K. Subramanyan, R. B. Dhanalakshmi, A. M. Stephan, V. Aravindan, *Batteries Supercaps* **2020**, *3*, 581.
[195] F. Larouche, F. Tedjar, K. Amouzegar, G. Houlachi, P. Bouchard, G. P. Demopoulos, K. Zaghib, *Materials* **2020**, *13*, 801.
[196] J. Dunn, A. Kendall, M. Slattery, *Resour., Conserv. Recycl.* **2022**, *185*, 106488.
[197] M. Chen, X. Ma, B. Chen, R. Arsenault, P. Karlson, N. Simon, Y. Wang, *Joule* **2019**, *3*, 2622.
[198] S. Vangala, B. Casagranda, *Clim. Energy* **2023**, *39*, 19.
[199] L. Albertsen, J. L. Richter, P. Peck, C. Dalhammar, A. Plepys, *Resour., Conserv. Recycl.* **2021**, *172*, 105658.
[200] N. O. Bonsu, *J. Cleaner Prod.* **2020**, *256*, 120659.
[201] W. A. Shaikh, M. A. Kalwar, M. A. Khan, A. Nawaz Wassan, M. Hussain Wadho, M. Faisal Shahzad, *Jordan J. Mech. Ind. Eng.* **2023**, *17*, 19956665.
[202] Y. Deng, Y. Mu, X. Wang, S. Jin, K. He, H. Jia, S. Li, J. Zhang, *Energy Rep.* **2023**, *9*, 337.
[203] V. M. Leal, J. S. Ribeiro, E. L. D. Coelho, M. B. J. G. Freitas, *J. Energy Chem.* **2023**, *79*, 118.
[204] V. E. O. Santos, V. G. Celante, M. F. F. Lelis, M. B. J. G. Freitas, *J. Power Sources* **2012**, *218*, 435.
[205] S. yin Tan, D. J. Payne, J. P. Hallett, G. H. Kelsall, *Curr. Opin. Electrochem.* **2019**, *16*, 83.
[206] X. Yu, W. Li, V. Gupta, H. Gao, D. Tran, S. Sarwar, Z. Chen, *Global Challenges* **2022**, *6*, 2200099.
[207] C. M. Costa, J. C. Barbosa, R. Gonçalves, H. Castro, F. J. D. Campo, S. Lanceros-Méndez, *Energy Storage Mater.* **2021**, *37*, 433.
[208] L. Lander, T. Cleaver, M. A. Rajaeifar, V. Nguyen-Tien, R. J. R. Elliott, O. Heidrich, E. Kendrick, J. S. Edge, G. Offer, *iScience* **2021**, *24*, 102787.
[209] F. Momeni, J. Ni, *Engineering* **2020**, *6*, 1035.
[210] D. Ravichandran, M. Kakarla, W. Xu, S. Jambhulkar, Y. Zhu, M. Bawareth, N. Fonseca, D. Patil, K. Song, *Composites, Part B* **2022**, *247*, 110352.
[211] D. Ravichandran, R. J. Ahmed, R. Banerjee, M. Ilami, H. Marvi, G. Miquelard-Garnier, Y. Golan, K. Song, *J. Mater. Chem. C* **2022**, *10*, 13762.
[212] H. Wei, Q. Zhang, Y. Yao, L. Liu, Y. Liu, J. Leng, *ACS Appl. Mater. Interfaces* **2017**, *9*, 876.
[213] J. C. Breger, C. Yoon, R. Xiao, H. R. Kwag, M. O. Wang, J. P. Fisher, T. D. Nguyen, D. H. Gracias, *ACS Appl. Mater. Interfaces* **2015**, *7*, 3398.
[214] L. K. Rivera-Tarazona, T. Shukla, K. Abhay Singh, A. K. Gaharwar, Z. T. Campbell, T. H. Ware, *Adv. Funct. Mater.* **2022**, *32*, 2106843.
[215] C. Cui, L. An, Z. Zhang, M. Ji, K. Chen, Y. Yang, Q. Su, F. Wang, Y. Cheng, Y. Zhang, *Adv. Funct. Mater.* **2022**, *32*, 2203720.
[216] Y. Wang, C. Chen, H. Xie, T. Gao, Y. Yao, G. Pastel, X. Han, Y. Li, J. Zhao, K. Fu, L. Hu, *Adv. Funct. Mater.* **2017**, *27*, 1703140.
[217] S. Weng, X. Kuang, Q. Zhang, C. M. Hamel, D. J. Roach, N. Hu, H. Jerry Qi, *ACS Appl. Mater. Interfaces* **2021**, *13*, 12797.
[218] P. Rewatkar, P. K. Enaganti, M. Rishi, S. Mukhopadhyay, S. Goel, *Int. J. Hydrogen Energy* **2021**, *46*, 35408.
[219] H. He, L. Zeng, D. Luo, J. He, X. Li, Z. Guo, C. Zhang, *Adv. Mater.* **2023**, *35*, 2211498.
[220] L. Zeng, H. He, H. Chen, D. Luo, J. He, C. Zhang, *Adv. Energy Mater.* **2022**, *12*, 2103708.
[221] K. Sirengo, A. Babu, B. Brennan, S. C. Pillai, *J. Energy Chem.* **2023**, *81*, 321.
[222] W. Wang, C. Li, S. Liu, J. Zhang, D. Zhang, J. Du, Q. Zhang, Y. Yao, W. Wang, C. Li, S. Liu, Y. Yao, J. Zhang, D. Zhang, J. Du, Q. Zhang, *Adv. Energy Mater.* **2023**, *13*, 2300250.
[223] Y. Ren, F. Meng, S. Zhang, B. Ping, H. Li, B. Yin, T. Ma, *Carbon Energy* **2022**, *4*, 446.
[224] M. Zhang, L. Pan, Z. Jin, X. Wang, H. Mei, L. Cheng, L. Zhang, *Adv. Energy Mater.* **2023**, *13*, 2204058.
[225] H. Lu, J. Hu, Y. Zhang, K. Zhang, X. Yan, H. Li, J. Li, Y. Li, J. Zhao, B. Xu, *Adv. Mater.* **2023**, *35*, 2209886.
[226] G. Zhang, X. Zhang, H. Liu, J. Li, Y. Chen, H. Duan, *Adv. Energy Mater.* **2021**, *11*, 2003927.
[227] M. Zhang, T. Hu, X. Wang, P. Chang, Z. Jin, L. Pan, H. Mei, L. Cheng, L. Zhang, *J. Mater. Chem. A* **2022**, *10*, 7195.

[228] X. Gao, K. Liu, C. Su, W. Zhang, Y. Dai, I. P. Parkin, C. J. Carmalt, G. He, *SmartMat* **2023**, *3*, e1197.
[229] G. Zhang, X. Zhang, H. Liu, J. Li, Y. Chen, H. Duan, *Adv. Energy Mater.* **2021**, *11*, 2003927.
[230] J. Ma, S. Zheng, L. Chi, Y. Liu, Y. Zhang, K. Wang, Z.-S. Wu, J. Ma, S. Zheng, L. Chi, Y. Liu, Y. Zhang, Z.-S. Wu, K. Wang, *Adv. Mater.* **2022**, *34*, 2205569.
[231] Z. Li, Y. Gao, H. Huang, W. Wang, J. Zhang, Q. Yu, *Composites, Part B* **2023**, *258*, 110712.
[232] J. Zheng, C. Hu, L. Nie, H. Chen, S. Zang, M. Ma, Q. Lai, *Adv. Mater. Technol.* **2023**, *8*, 2201591.
[233] M. Shi, T. Li, H. Shang, D. Zhang, H. Qi, T. Huang, Z. Xie, J. Qi, F. Wei, Q. Meng, B. Xiao, Q. Yin, Y. Li, D. Zhao, X. Xue, Y. Sui, *J. Energy Storage* **2023**, *68*, 107765.
[234] Z. Li, J. Häcker, M. Fichtner, Z. Zhao-Karger, *Adv. Energy Mater.* **2023**, *13*, 2300682.
[235] Z. Huang, X. Du, M. Ma, S. Wang, Y. Xie, Y. Meng, W. You, L. Xiong, *ChemSusChem* **2023**, *16*, 202202358.
[236] V. Verma, S. Kumar, W. Manalastas, R. Satish, M. Srinivasan, *Adv. Sustainable Syst.* **2019**, *3*, 1800111.
[237] X. Wang, R. Xiao, H. Li, L. Chen, *J. Materiomics* **2017**, *3*, 178.
[238] M. Attarian Shandiz, R. Gauvin, *Comput. Mater. Sci.* **2016**, *117*, 270.
[239] R. A. Eremin, P. N. Zolotarev, O. Y. Ivanshina, I. A. Bobrikov, *J. Phys. Chem. C* **2017**, *121*, 28293.
[240] O. Allam, B. W. Cho, K. C. Kim, S. S. Jang, *RSC Adv.* **2018**, *8*, 39414.
[241] R. Jalem, K. Kanamori, I. Takeuchi, M. Nakayama, H. Yamasaki, T. Saito, *Sci. Rep.* **2018**, *8*, 5845.
[242] B. Liu, J. Yang, H. Yang, C. Ye, Y. Mao, J. Wang, S. Shi, J. Yang, W. Zhang, *J. Mater. Chem. A* **2019**, *7*, 19961.
[243] M. Dixit, N. Muralidharan, A. Bisht, C. J. Jafta, C. T. Nelson, R. Amin, R. Essehli, M. Balasubramanian, I. Belharouak, *ACS Energy Lett.* **2023**, *5*, 2356.
[244] R. Car, *Quant. Struct.-Act. Relat.* **2002**, *21*, 97.
[245] T. Hansson, C. Oostenbrink, W. F. Van Gunsteren, *Curr. Opin. Struct. Biol.* **2002**, *12*, 190.
[246] T. P. Fries, T. Belytschko, *Int. J. Numer. Methods Eng.* **2010**, *84*, 253.
[247] J. T. Katsikadelis, M. S. Nerantzaki, *Eng. Anal. Boundary Elem.* **1999**, *23*, 365.
[248] B. Regassa Hunde, A. Debebe Woldeyohannes, *Results Eng.* **2022**, *14*, 100478.
[249] K. J. Prabuchandran, S. Penubothula, C. Kamanchi, S. Bhatnagar, *Appl. Intell.* **2021**, *51*, 1565.
[250] S. Lang, T. Reggelin, J. Schmidt, M. Müller, A. Nahhas, *Expert Syst. Appl.* **2021**, *172*, 114666.
[251] J. M. Tarascon, *Nat. Mater.* **2022**, *21*, 979.
[252] M. Zheng, H. Salim, T. Liu, R. A. Stewart, J. Lu, S. Zhang, *Energy Environ. Sci.* **2021**, *14*, 5801.
[253] S. Haghi, M. F. V. Hidalgo, M. F. Niri, R. Daub, J. Marco, *Batteries Supercaps* **2023**, *6*, 202300046.
[254] A. Pregowska, M. Osial, W. Urbańska, *Recycling* **2022**, *7*, 81.

Nathan Fonseca, currently a Ph.D. student at Arizona State University (ASU), is under the guidance of Prof. Kenan Song. He completed his B.S. in engineering with a specialization in mechanical engineering systems at ASU in 2018. Nathan's research encompasses several areas, including additive manufacturing for improved performance in energy storage devices, sensing, textiles, and co-design/manufacturing strategies. Presently, his primary focus lies in developing a novel approach to 3D printing interdigitated batteries using co-axial printing. This technique aims to enhance the ionic kinetic energy within energy storage devices by enabling the deposition of the battery in a single process.

Kenan Song is currently holding an associate professor position at the University of Georgia (UGA) and is affiliated with Arizona State University. Dr. Song's research interest includes the processing-structure-property relationships, especially advanced manufacturing, characterization, simulation, and application of polymer-based nanoparticle-filled composites for energy, sustainability, health, and smart systems. Kenan Song has been the recipient of the NSF CAREER Award (2022), ACS PMSE Young Investigator Award (2022), SAMPE North America Young Professionals Emerging Leadership Award (YPELA) (2022), and DHS New Investigator Award (NIA).